Coherent excitation of ultracold atoms between ground and Rydberg states

ABEL, RICHARD,PHILIP

Coherent excitation of ultracold atoms between ground and Rydberg states

Richard P. Abel

A thesis submitted in partial fulfilment
of the requirements for the degree of
Doctor of Philosophy

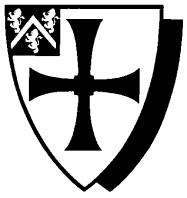

Department of Physics
University of Durham

1st August, 2011

Coherent excitation of ultracold atoms between ground and Rydberg states

Richard P. Abel

Abstract

This thesis describes the development of an experiment to study coherent population transfer between ground states, and between ground and Rydberg states, in ultracold atoms.

In order to study coherent transfer between hyperfine ground states a pair of phase stable Raman beams is required. Both beams are derived from a single master laser before being spatially separated into individual components using a novel Faraday filtering technique. The frequency dependent Faraday effect in an isotopically pure thermal vapour is exploited to rotate the plane of polarisation of each Raman component such that they may be separated using a polarising beam splitter. The Raman beams are applied to a sample of ultracold atoms and evidence of coherent population transfer is observed.

Rydberg states offer an ideal tool for electrometry; the electric field induced Rydberg energy level shift scales with the seventh power of the principle quantum number. Electromagnetically induced transparency (EIT) is used to map Rydberg energy level shifts onto a ground state transition. EIT in a thermal vapour cell also provides a novel method of stabilising the Rydberg coupling laser. The Rydberg energy level shift is highly sensitive to the electric field produced by adsorbates bonded to a nearby dielectric surface. These effects are found to be time dependent and can be eliminated if the electric field is applied transiently. The measured electric field is compared to that calculated by numerical solution of Laplace's equation; the bulk dielectric is found to have a strong effect on the local electric field experienced by the atoms.

The exaggerated properties of Rydberg states make these systems ideal for quantum information processing and precision electrometry.

Contents

List of Figures

List of Tables

Declaration

I confirm that no part of the material offered has previously been submitted by myself for a degree in this or any other University. Where material has been generated through joint work, the work of others has been indicated.

Richard P. Abel
Durham, 1st August, 2011

Acknowledgements

The completion of this thesis has been made possible only through the help and guidance I have received from many people during my time in Durham. Most importantly thanks must go to my supervisor, Charles Adams, for giving me the opportunity to continue studying in Durham and his great scientific insight without which this work would have been impossible. During this project I have worked with two excellent post-docs from whom I have learnt so much; thanks must go to Ashok Mohapatra for introducing me to experimental atomic physics and Ulrich Krohn for his never ending patience. I am also very grateful to Ifan Hughes for his help on the Faraday filter project and meticulous proof reading; Matt Jones for useful discussions and career advice; and Simon Gardiner for his advice and proof reading some of this thesis.

The friendly atmosphere of the atomic physics group in Durham has made it an enjoyable place to work. This thesis would not have been possible without the help and friendship I have received over the past three and a half years from too many people to mention them all. In particular thanks must go to Christopher Carr for his help in the lab and Graham Lochead for his knowledge of electronics and proof reading. Special mention must go to my long term office mates James Millen and Jon Pritchard for their much appreciated banter and friendship. Finally, I would like to thank all my friends and family for their support over the many years I have been a student; special thanks go to my little brother for his great friendship and lastly to my parents for their love and encouragement without which I would not have achieved what I have.

Dedicated to Mum and Dad,
for all their love and support.

Chapter 1

Introduction

Coherent excitation

The study of coherent excitation covers a broad range of topics in atomic physics. Fundamental to the study of coherent excitation is the requirement of a coherent source of electro-magnetic radiation; the invention of the laser [1] triggered an era of intense investigation into the interaction of coherent light with atoms.

When coherent light interacts with a simple two-level atom [2] the wavefunction is found to oscillate coherently between the ground and excited states in a process known as Rabi oscillation. The inversion of the atom's state may be monitored by measuring their fluorescence varying between maxima and minima as a function of the incident light pulse duration [3]; the frequency of this oscillation is known as the Rabi frequency. The pulse required to transfer the atom from the ground to excited state is defined as a '$\pi-$pulse'. The light pulse may be characterised by an 'area' found from the time-integrated electric field envelope function; one may therefore refer to a $\pi-$pulse having an area equal to π.

This simple case can be extended to a variety of systems with multi-level atoms and different combinations of coherent light fields. If the two-level atom, with a resonant probe beam, is strongly coupled to a third level the medium may be rendered transparent to the probe. This process, known as electromagentically induced transparency (EIT) [4, 5], appears in a variety of

forms and was first observed experimentally by Harris *et al.* [6]. Although as a result of EIT the medium becomes transparent on resonance, the transmitted beam will experience strong nonlinear and dispersive effects. EIT can be understood by considering the dressed state picture which combines the bare atomic states with the eigenstates of the light field [7]. In this picture the dressed states are spaced equally about the zero field resonance and decay to the same continuum. When the probe is tuned to resonance the contribution from the coupling to each dressed state will cancel out due to a Fano-like interference [8] of the decay channels, hence the probe will not be absorbed by the medium. EIT has subsequently found many applications, in particular the dispersive properties of an EIT resonance leads to a large reduction of the group velocity of light within the medium, creating so called slow light [9].

Other coherent phenomena that arise in a system of three atomic levels interacting with two light fields include coherent population trapping (CPT) [10]. If one considers a Λ scheme with two ground states coherently coupled to a shared excited state, with the two photon Raman resonance condition fulfilled, the excited state will become decoupled or dark. As there is no absorption route from the dark state, population will become trapped in that state. The creation of the dark state can be made dependent on the velocity of the atom so that zero velocity atoms experience no absorption. This technique, known as velocity selective coherent population trapping (VSPT), can be employed in laser cooling experiments to reach temperatures below the single photon recoil limit [11]. Similarly, the creation of a dark state can be exploited to transfer population between states efficiently. The technique of stimulated Raman adiabatic passage (STIRAP) [12] allows transfer via an excited state without actually populating that state, thus eliminating spontaneous decay.

Rydberg physics

Highly excited Rydberg states [13, 14] have been the subject of much recent interest; the extreme properties of Rydberg atoms has led to their study and application in a wide range of fields. Firstly, Rydberg atoms have been

proposed as a tool with which to carry out quantum information processing (QIP) [15] because of their strong yet controllable interactions [16, 17]. As well as individual atom quantum gates Rydberg atoms have also been studied with regard to many-particle entanglement [18–21]. Similarly, proposals have been made regarding: many-body quantum simulations [22]; single-atom and single-photon sources [23]; and non-local gates with microwave resonators [24, 25].

The study of many-body Rydberg effects began with experiments carried out in atomic beams [26, 27]. Developments in laser cooling and trapping techniques [28] has allowed the study of cold, dense samples of atoms. Using such methods the suppression of Rydberg excitation [29–31] and collective effects [32, 33] have been observed. Recent experiments that utilise the dipole blockade between individual trapped atoms [34, 35] have achieved remarkable results; a quantum C-NOT gate has been demonstrated [36] along with the controlled entanglement of atoms [37]. Additionally, the nature of the interaction of light with Rydberg atoms leads to interesting quantum mechanical and non-linear optical effects such as superrandiance [38], co-operative atom light interactions [39], four wave mixing [40] and the giant Kerr effect [41].

Rydberg physics has grown into an expansive field; there is much ongoing study into long range Rydberg molecules [42, 43], anti-matter Rydberg atoms [44], magnetic trapping of Rydberg atoms [45], interacting cold two-electron atom Rydberg gasses [46] and ultracold neutral plasmas [47].

1.1 Thesis layout

This thesis presents the work carried out to build an experimental apparatus with which to study coherent excitation between ground states and excitation from those ground states to Ryderg states. As the experiments are to be carried with ultracold atoms a laser cooling and trapping setup must be established. With a flexible ultracold atom apparatus developed one may then carry out a variety of experiments. The thesis is structured as follows:

- Chapter 2 gives an introduction to the properties of Rydberg atoms and their application in relation to quantum information processing.

The long term goals and proposals that motivate the work presented within this thesis are then discussed.

- Chapter 3 gives details of the experimental apparatus used throughout the reminder of the thesis. The design features motivated by the quantum information processing and electrometry proposals in Chapter 2 are introduced. Details are then presented of the magneto-optic and dipole trap setup and their characterisation.

- Chapter 4 covers coherent excitation between ground states. A novel method of producing phase stable Raman beams from a single master laser is presented. Work towards Raman transfer between ground states is then detailed and the results discussed.

- Chapter 5 presents details of a novel laser stabilising scheme required to achieve coherent two-photon excitation to Rydberg states. A technique for locking a Rydberg coupling laser to an EIT signal in thermal vapour cell is presented. The performance of the laser system is then evaluated using various methods.

- Chapter 6 covers the work carried out on spectroscopy of the Rydberg state using EIT in ultracold atoms. Using the EIT spectra a method of carrying out electrometry near a dielectric surface is presented. The results of the electrometry are given and compared with a theoretical calculation of the expected electric field in close proximity to a dielectric.

- Chapter 7 summarises the important results and draws conclusions from the work carried out.

1.2 Publications arising from this work

- R. P. Abel, A. K. Mohapatra, M. G. Bason, J. D. Pritchard, K. J. Weatherill, U. Raitzsch and C. S. Adams, *Laser frequency stabilization to excited state transitions using electromagnetically induced transparency in a cascade system*, Appl. Phys. Lett. **94**, 071107 (2009).

- R. P. Abel, U. Krohn, P. Siddons, I. G. Hughes and C. S. Adams, *Faraday dichroic beam splitter for Raman light using an isotopically pure alkali-metal-vapor cell*, Opt. Lett. **34**, 30713073 (2009).

- R. P. Abel, C. Carr, U. Krohn and C. S. Adams, *Electrometry near a dielectric surface using Rydberg electromagnetically induced transparency*, Phys. Rev. A **84**, 023408 (2011).

Related publications

- K. J. Weatherill, J. D. Pritchard, R. P. Abel, M. G. Bason, A. K. Mohapatra, C. S. Adams, *Electromagnetically induced transparency of an interacting cold Rydberg ensemble*, J. Phys. B **41**, 201002 (2008).

Chapter 2

Rydberg atoms: Properties and applications

This chapter begins by discussing some of the fundamental properties of Rydberg atoms and the nature of their exaggerated properties. The two most important applications of Rydberg atoms, namely quantum information processing and precision measurement, are discussed in further detail in Sec. 2.1.2 and Sec. 6.2. Following this the long term goals that motivate the work presented in this thesis are given. The work on ground state excitation is motivated by a proposed mesoscopic quantum Rydberg gate [20] and details of how this can be extended to include single site addressibility are given. Finally, the prospect of utilising ultracold Rydberg atoms as an electric field sensor using electromagnetically induced transparency is discussed.

2.1 Rydberg atoms

2.1.1 Properties

Rydberg atoms are atoms in states of high principal quantum number, n. The first realisation of Rydberg atoms came with Balmer's 1885 formula describing the wavelengths of the visible series of atomic hydrogen:

$$\lambda = \frac{bn^2}{n^2 - 4}, \tag{2.1}$$

where $b = 3.6456 \times 10^{-7}$ m. This describes the now familiar Balmer series of transitions from $n = 2$ to highly excited states. By 1890 Rydberg had begun to study the spectral lines of alkali metal atoms [13] and consequently discovered a more generalised version of Balmer's formula [14]:

$$\pm\,\nu = \frac{R_y}{(m-\delta_s)^2} - \frac{R_y}{(n-\delta_p)^2}, \tag{2.2}$$

where the series of p states is given by the minus sign and constant m; the s states are correspondingly given by the plus sign and constant n. The δ terms are known as the quantum defects and R_y is the Rydberg constant. The result of a high principle quantum number is made apparent by the Bohr model of the atom. By the quantisation of angular momentum Bohr was able to propose a formula for the radius and binding energy of an electron orbit:

$$r = \frac{n^2\hbar^2}{Ze^2mk}, \tag{2.3}$$

$$W = \frac{-k^2Z^2e^4m}{2n^2\hbar^2}. \tag{2.4}$$

Here $k = 1/4\pi\epsilon_0$, e is the charge of the electron, m is the mass and Z the charge of the positive nucleus. It is clear from these expressions that for high values of n the electron will be in a very large, weakly bound orbital. Rydberg atoms therefore have extreme properties when compared to ground state atoms and thus are of great interest in numerous fields of research.

The key properties of Rydberg atoms are presented in Table 2.1 along with the corresponding scaling with n. It is clear that for high values of n these properties will depart dramatically from the case of ground state atoms. The applications most relevant for the work in this thesis are quantum information processing (QIP) and precision electrometry; both will be reviewed in the following sections.

2.1.2 Rydberg atoms in QIP

The unique properties of Rydberg atoms make them excellent candidates for various quantum information processing (QIP) applications. There has

Property	n scaling
Binding energy	n^{-2}
Orbital radius	n^2
Geometric cross section	n^4
Polarisability	n^7
Radiative lifetime	n^3
Dipole moment	n^2

Table 2.1: Rydberg atom property dependance on principal quantum number, n. Reproduced from Ref. [14].

been much recent interest in QIP with Rydberg atoms and progress over the last decade is reviewed in depth by Saffman *et al.* [48]. Rydberg atoms are suitable candidates for the realisation of qubits because of their long lifetime and strong interactions. These interactions have the distinct advantage of being state dependent; a weak interaction between ground state atoms may be conveniently switched to a strong interaction by excitation to a Rydberg state. The interactions of neutral atoms, Rydberg atoms and ions are summarised in Fig. 2.1 as a function of particle separation, R. For ground state atoms, at close range, $1/R^6$ dependent Van der Waals interactions dominate. At long range the magnetic dipole-dipole interactions that scale as $1/R^3$ are dominant. Conversely, the close range interaction between Rydberg atoms is resonant dipole-dipole in character, with a $1/R^3$ scaling, and dominated by Van der Waals at long range with a $1/R^6$ dependance. At a distance of the order of ten μm[1] the difference in interaction strength between ground and Rydberg state atoms can be as large as 10^{12} [48]. This behaviour is contrary to that of a trapped ion; the Coulomb interaction between ions, although much stronger, exists at all times with no possibility for switching.

The strong interaction between Rydberg atoms gives them interesting collective behaviour; perhaps most important here is the concept of the dipole blockade. An atom excited to a Rydberg state will have a strong influence

[1]The interaction strength and distance at which the change in character from dipole-dipole interaction to Van der Waals occurs is dependent on the Rydberg state. This estimate is for the $n = 100s$ state. See Ref. [48] for details.

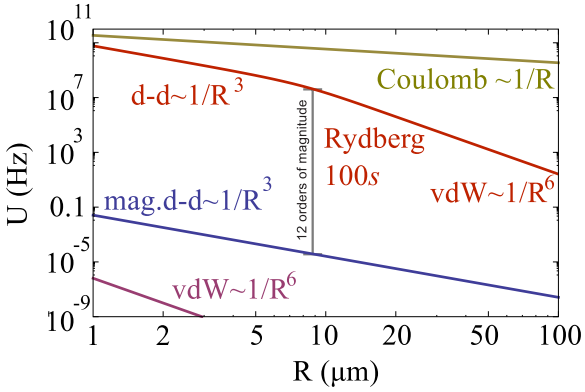

Figure 2.1: Interaction strength as a function of particle separation for Rb ground state atoms, Rb atoms excited to the 100s Rydberg state and ions. Figure reproduced from Ref. [48].

over its neighbouring atoms and will significantly shift the energy of their Rydberg states. If this effect is large enough the Rydberg state may be shifted out of resonance with the excitation laser. This then causes a suppression in the number of atoms that can be excited to Rydberg states; the sample is said to be blockaded. As the energy shift depends on the separation between the atoms a radius where only one Rydberg excitation is possible may be defined and is known as the 'blockade radius'.

The possibility of exploiting the interactions between Rydberg atoms to create neutral atom quantum gates was introduced by Jaksch *et al.* [16] and subsequently extended to ensembles of atoms by Lukin *et al.* [17]. Extensive work towards the implementation of a quantum gate using individually trapped atoms has been carried out [35, 49, 50] culminating in the realisation of a controlled-NOT quantum gate [36]. Similar work has demonstrated entanglement of individual atoms using Rydberg blockade [34, 37].

The C-NOT operation that may be achieved using the dipole blockade is summarised in Fig. 2.2. The control and target atoms are held in a pair of micro-dipole traps [51] with trap centres a few μm apart. The sequence of seven π-pulses acts to swap the amplitude of the target atom states dependent on the state of the control atom. If the control atom is initially in state $|1\rangle$ it will be unaffected by Rydberg excitation pulses 1 and 7. The sequence of pulses on the target atom, 2 to 6, will then swap the amplitudes of $|0\rangle$ and

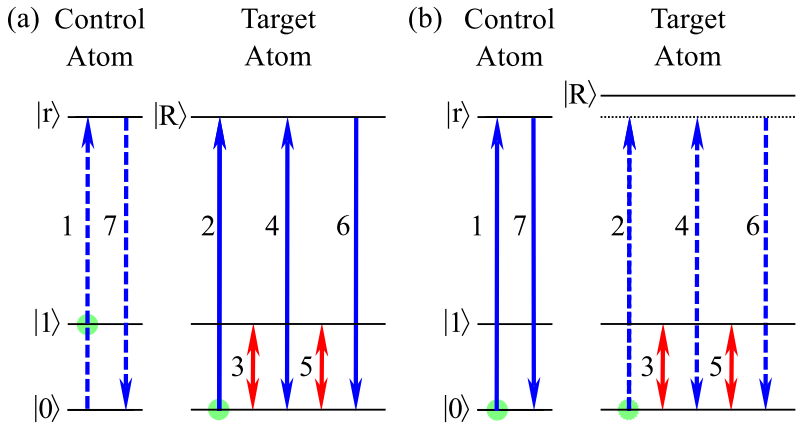

Figure 2.2: Pulse sequence required to achieve the C-NOT operation. In (a) the control atom begins in state $|0\rangle$ and the pulse sequence produces an amplitude swap between the target states $|0\rangle$ and $|1\rangle$. In (b) the dipole blockade acts to shift the energy of the target atom Rydberg state and the swap between ground states is blocked. Figure reproduced from Ref. [36].

$|1\rangle$. If the control atom is initially in state $|0\rangle$ pulse 1 will be on-resonance and excite the atom into the Rydberg state. The effect of the dipole blockade then results in pulses 2, 4 and 6 being off-resonance and have no affect. Pulses 3 and 5 then combine to produce a 2π pulse and the amplitude of $|0\rangle$ and $|1\rangle$ will not be swapped.

Along with the success of quantum information using individual atoms there has been much interest in the implementation of Rydberg atom ensembles for QIP [17]. One such proposal, that of Müller *et al.* [20], suggests a method of producing a mesoscopic gate based on electromagnetically induced transparency. In this scheme a swap between states $|0\rangle$ and $|1\rangle$ in N ensemble atoms is performed conditionally on the state of a single control atom. The scheme is summarised in Fig. 2.3. A single control atom is prepared in states $|0\rangle$ or $|1\rangle$; if $|1\rangle$ is a Rydberg state the atom will interact strongly with the nearby ensemble atoms. This interaction will shift the energy of the Rydberg states of the ensemble atoms resulting in the coupling laser becoming off-resonant [part (a) in Fig. 2.3]. Population can then be swapped between states $|A\rangle$ and $|B\rangle$ using an off-resonant Raman transfer. If the energy levels of the ensemble atoms are not shifted [part (b) in Fig. 2.3] a two-photon EIT type resonance occurs and the transfer from $|A\rangle$ and $|B\rangle$ will be blocked.

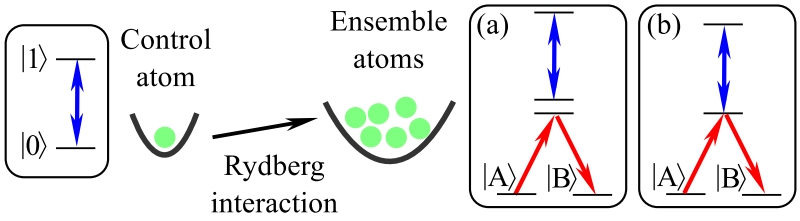

Figure 2.3: Proposed scheme for the mesoscopic Rydberg gate. The ensemble atoms are swapped between states $|A\rangle$ and $|B\rangle$ depending on the state of the control atom. Figure adapted from Ref. [20].

Muller *et al.* report that with an appropriate choice of parameters the transfer from $|A\rangle$ to $|B\rangle$ may be blocked with a fidelity of more than 99%. The realisation of this scheme is discussed in further detail in Chapter 4.

2.1.3 Rydberg atoms in electrometry

Rydberg atoms have found many useful applications in the field of precision electrometry. In the presence of an electric field the Rydberg energy level will be Stark shifted by an amount proportional to the polarisability of the relevant Rydberg state. From the Rydberg atom property scaling in Table 2.1 it is clear that with a high value of n the polarisability can be made extremely large. The Rydberg energy shift can therefore be large even if the local electric field is small, thus providing a good system for *in situ* precision electrometry.

The possibility of exploiting Rydberg energy level shifts was initially raised with regard to performing precision measurements of fundamental physical constants. In such experiments the absence or precise control of external fields can be of paramount importance. Spectroscopy of Rydberg states at $n \sim 500$ has been carried out in an atomic beam of Barium [52]. Using this method the background electric field could be minimised to a level of 45 μV/cm or less. Similarly, Stark effects in a beam of potassium atoms have be measured to minimise stray electric fields to less than 50 μV/cm [53]. Additionally, stray fields have been measured at a level of 100 μV/cm by monitoring SF_6^- formation at the onset of field ionisation of high n state argon Rydberg atoms [54].

More recently, spatially resolved electrometry has been demonstrated using a Bose-Einstein condensate (BEC) [55, 56] that is magnetically trapped. Using this approach, spatially resolved measurements of electric fields have been made [57, 58]. These results are of particular interest because they are highly sensitive to the presence of adsorbates on nearby conducting and dielectric surfaces. Using the Rydberg atom approach measurements sensitive to inhomogeneous electric fields have been performed with an accuracy of 20 $\mu V/\mathrm{cm}$ [59]. Furthermore, the effects of electric fields on Rydberg atoms in thermal vapours have been studied [60, 61]. Surface effects have also been investigated using ultracold Rydberg atom electrometry including: stray 'patch' fields at conducting surfaces [62, 63]; Rydberg energy level shifts in the vicinity of an atom chip [64]; and the effect of nearby ions on Rydberg states [65].

2.2 This thesis

The work presented in this thesis is motivated by the aforementioned fields of QIP and precision electrometry. As the title suggests this work is concerned with two related topics: coherent ground state excitation in relation to QIP; and excitation to Rydberg states to perform electrometry. The following sections discuss the long term objectives that motivate the work presented later.

2.2.1 QIP: Coherent ground state excitation

A fundamental step towards creating the mesoscopic Rydberg gate of Müller *et al.* [20] is the coherent transfer of ensemble atoms between two qubit states. This may be achieved using a coherent two-photon Raman transfer which has been already successfully employed to create ion quantum gates [66] and Rydberg quantum gates [36]. An alternative is to use stimulated Raman adiabatic passage (STIRAP) [12] to achieve qubit rotations [67]. As a step towards a mesoscopic Rydberg gate one may envisage the scheme described in Fig. 2.4. In (a) Raman transfer is driven between states $|0\rangle$ and $|1\rangle$ by Raman beams λ_{R}. A measurement of the population of atoms in state $|0\rangle$ as a function of time will produced the Rabi oscillations shown in the inset. The

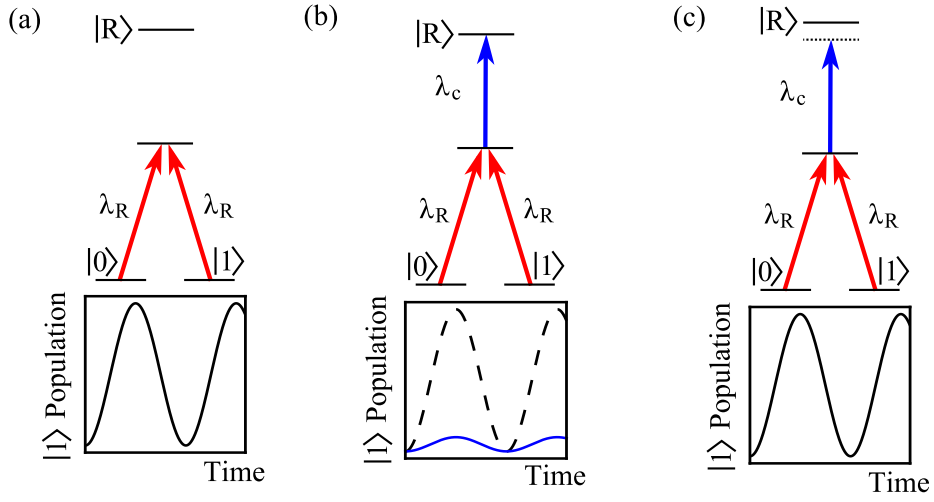

Figure 2.4: Qubit rotation controlled by Rydberg energy level shifts. In (a) Raman transfer occurs between states $|0\rangle$ and $|1\rangle$ allowing Rabi oscillations to be measured. In (b) the application of the Rydberg coupling blocks the Raman transfer. In (c) the Rydberg state is shifted using an electric field and the Rabi oscillations are once again observed.

coupling to a Rydberg state by λ_c would then act to suppress the Raman transfer as shown in part (b). Measurement of the $|0\rangle$ population would hence show a suppression of the Rabi oscillations. Finally in (c) an electric field is applied to shift the Rydberg state and thus lift the two-photon EIT resonance. In this way the electric field acts in a similar manner as the dipole blockade mechanism to unblock the Raman transfer. With a sufficiently large field the Rabi oscillations between $|0\rangle$ and $|1\rangle$ should then be recovered. This scheme therefore allows the control of qubit rotations using Rydberg energy level shifts.

As well as the controlled qubit rotation scheme taking place in a single ensemble of trapped atoms it may be possible to adapt the scheme into an array of qubits. Specifically, the scheme in Fig. 2.4 may be extended by trapping atoms in an optical lattice [68]. In previous work single lattice sites have been manipulated using optical tweezers [69] and resolved using high numerical aperture optics [70]. Atoms could be loaded into a 1-D optical lattice as shown in Fig. 2.5. The application of a steeply varying electric field, indicated by the black line, will produce a spatially varying Stark shift across the lattice sites. The Rydberg energy levels will consequently be shifted a

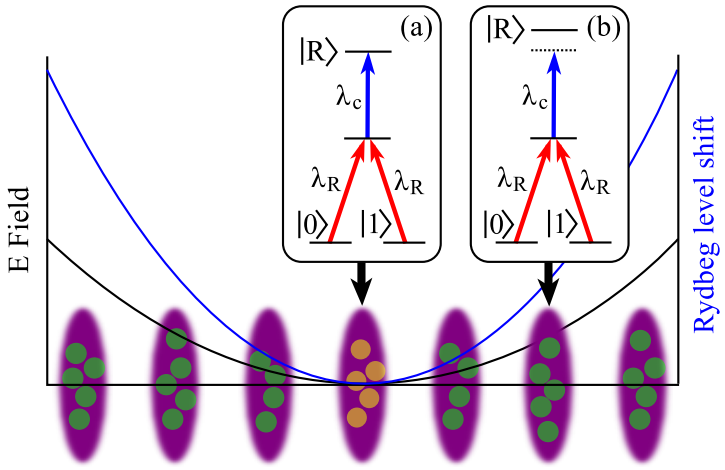

Figure 2.5: Single site addressibility scheme. At the central lattice site the electric field is zero so that the Rydberg coupling is on resonance in (a). Raman transfer will be blocked between states $|0\rangle$ and $|1\rangle$. At other lattice sites the situation in (b) will occur; the Rydberg coupling will be off-resonance and the Raman transfer will take place.

differing amount depending on the position of the atoms within the lattice, shown by the blue line. At a central lattice site the electric field and Rydberg energy shift will be zero; at this site the Rydberg coupling laser will be on-resonance and Raman transfer blocked [inset (a) in Fig. 2.5]. At other lattice sites the Rydberg energy shift will result in the coupling laser being off-resonance; in this case the Raman transfer will not be blocked. With the large polarisability of the Rydberg state the level shift between neighbouring lattice sites can be large for only a moderate electric field gradient. Therefore, using this scheme only a single lattice site will be addressed so long as the linewidth of the coupling laser is less the the Rydberg level shift between neighbouring lattice sites. The lattice sites addressed can be selected by the application of an additional offset electric field to shift the zero field point to align with any point in the lattice.

In order that the single site addressibility scheme in Fig. 2.5 is possible the Rydberg level shift between adjacent lattice sites must be sufficiently large that that the Rydberg coupling laser is on resonance at only a single site. This can be achieved using an appropriate choice of electric field gradient and Rydberg state. The practicality of producing the necessary parameters is discussed below.

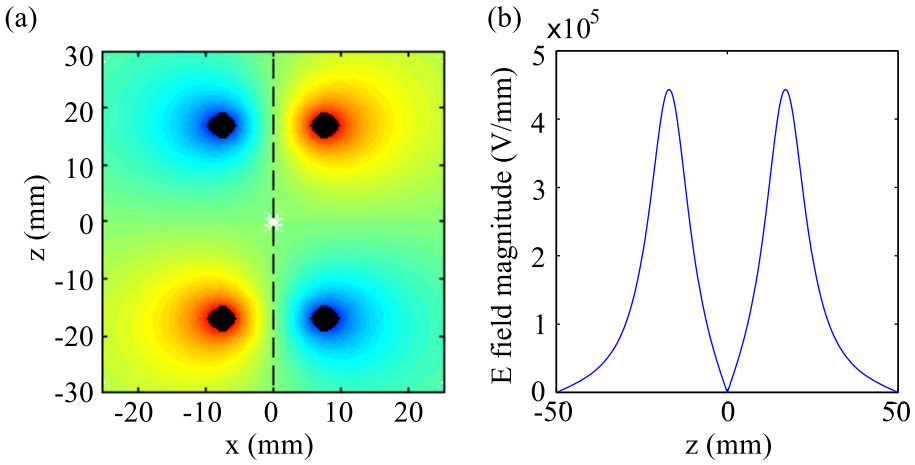

Figure 2.6: (a) Quadrapole potential produced by applying ±4 kV to the four electrodes (filled black circles). (b) Shows a slice through the electric field along the vertical dashed line.

To create an electric field gradient within the experimental volume an array of four electrodes may be used. The electric field can be calculated by numerically solving Laplace's equation, as described in Appendix A, for a given potential applied to the electrodes. The potential produced by applying ±4 kV to the electrodes is shown in Fig. 2.6 (a) along with the resulting electric field along the dashed line shown in (b). In this way a varying electric field can be applied across an optical lattice with a point of zero field at the centre. The energy shift, ΔV, in units of $\hbar$, produced by the field can be found by:

$$\Delta V = -\frac{1}{2}\alpha\mathcal{E}^2, \tag{2.5}$$

where α is the polarisability and $\mathcal{E}$ the electric field. The polarisability of the 42S Rydberg state is taken from Ref. [71] as $\alpha_{42S} = 2 \times 8.06$ MHz/(V/cm)^2. From this the polarisability of other Rydberg states is estimated using the scaling $\alpha \sim n^7$. The energy shift for the 70S Rydberg state as a function of position from the centre of the lattice is calculated and presented in Fig. 2.7. Lattice sites separated by 600 nm are shown along the x-axis by filled black circles. This shows that the shift in the energy of the 70S state between the central lattice site and its next nearest neighbour is approximately 1.8 MHz. For comparison, the separation between the 70S and 69S Rydberg states is

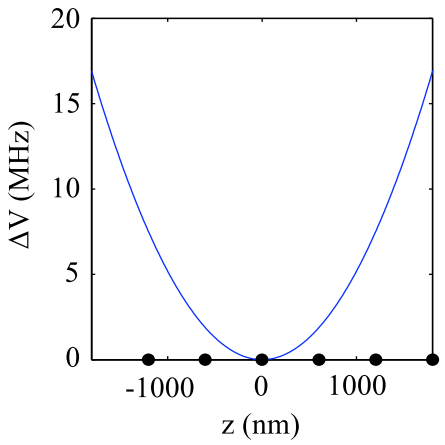

Figure 2.7: Rydberg energy shift of the 70S Rydberg state as a function of position from the centre of the lattice. Lattice sites with a separation of 600 nm are shown as black circles along the x-axis.

approximately 20 GHz. For the Rydberg laser to address only the site at the lattice centre, where the field is zero, the line width must be equal to or less than this energy shift. A laser linewidth of the order of 1 MHz is readily achievable using the methods discussed in Chaper 5.

2.2.2 Electrometry: Coherent Rydberg excitation

The secondary objective of the work presented in this thesis is to exploit the large polarisability of Rydberg atoms to perform sensitive electrometry. In order to successfully carry out the controlled qubit rotation and optical lattice experiments of the previous section a precise knowledge and control of the electric field applied to the location of the atoms is required. As discussed in Sec. 6.2 the Rydberg energy level shift provides a system with which to carry out electrometry.

To demonstrate a method of carrying out electrometry a spectroscopic technique is required to measure the Rydberg energy level shift caused by an electric field. The EIT mechanism required to block Raman transfer in the QIP schemes discussed in the previous section also provides a method with which to carry out spectroscopy of the Rydberg state. Extensive related work has been previously carried out in Durham on Rydberg EIT in thermal

vapour cells [41, 60, 61, 72, 73] and in ultracold atoms [39, 74]. Spectroscopy of the Rydberg state carried out in this way provides a non-destructive probe [74] of the Rydberg level shift in contrast to the more typical destructive ionisation techniques. As the relation between Rydberg energy level shifts and the electric field is well known, as shown by Eq. (2.5), the electric field can therefore be calibrated from the independently determined polarisability and the measured Rydberg energy level shift.

2.3 Summary and conclusion

This chapter began by introducing the key properties of Rydberg atoms and how these may produce interesting exaggerated affects. Of particular importance to the work in this thesis is the scaling of the polarisability with the seventh power of the principal quantum number. This gives Rydberg atoms extreme sensitivity to electric fields that can be exploited in a variety of experiments. Following this, in Secs. 2.1.2 and 6.2, the application of Rydberg atoms in the fields of quantum information processing and electrometry are discussed in detail. Several recent achievements and proposals in these fields are given. In the final sections the proposals that motivate the work presented in this thesis are presented. Ground state excitation is considered as the first step towards a mesoscopic quantum Rydberg gate and the feasibility of extending this to a single site addressibility experiment is considered. Lastly, a method of performing electrometry by employing electromagnetically induced transparency to perform spectroscopy on Rydberg energy level shifts is presented.

Chapter 3

Experimental setup and procedures

This chapter covers the design and setup of the experimental apparatus required for the work presented throughout this thesis. The chapter is split into three parts: firstly the design of the vacuum chamber and optics setup is given; secondly the setup of the magneto-optic trap (MOT) is discussed; and finally the dipole trap setup is presented.

In section 3.1 the design of the vacuum chamber is discussed and its key features introduced. In the following section the laser system used to generate light at all the required frequencies is discussed and the optical setup detailed. In section 3.3 the setup of the MOT is discussed along with its optimisation and characterisation. A detailed study of the MOT loading rate, image analysis, MOT temperature, probe absorption and magnetic field calibration is presented in this section. The final part of this chapter, section 3.5.3, covers the setup of the optical dipole trap. Firstly, the experimental setup and timing sequence required to load atoms into the trap is given. The chapter is then completed with the characterisation of the dipole trap; the image processing is discussed along with a measurement of the lifetime of atoms in the trap.

3.1 Vacuum chamber design and setup

In order to carry out experiments with ultracold atoms the sample of atoms must be isolated from their thermal surroundings. To achieve this the experiment must be carried out under ultra-high vacuum (UHV), with pressures typically below 10^{-10} Torr, maintained within a vacuum chamber. The vacuum system must have several key features, paramount of which are optical access and a source of atoms which are to be cooled. Additional features will be tailored towards the particular experiment that is to be carried out. The design for the vacuum system used for the work presented throughout this thesis is shown in Fig. 3.1. A supply of Rb atoms is provided by two dispensers[1] that produce a background gas of Rubidium from which the magneto-optic trap (MOT) can be loaded. Rubidium is released from the dispensers by applying an electrical current, for which the connection is made using a vacuum feed-through, labelled ⓖ in Fig. 3.1. The high vacuum is maintained by an ion pump, labelled ⓐ and a getter pump, ⓑ.

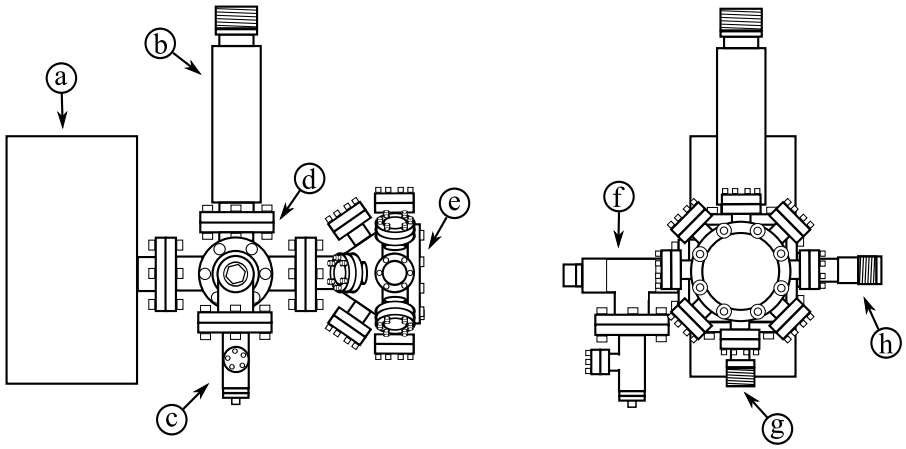

Figure 3.1: Schematic design of the vacuum system. The vacuum is maintained in the chamber using the ion pump ⓐ and getter pump ⓑ. The system is sealed using two all metal valves ⓒ and ⓕ. The Rb dispensers are connected using an electrical feed-through ⓖ and the connection to the electrodes is made using a high voltage feed-through ⓗ. Finally, the chamber for the experiment itself is labelled ⓔ. The aforementioned components are connected by a six-way cross section, labelled ⓓ.

[1] Alvatec 5 mg Rb dispersers

The most crucial design considerations must be made for the science chamber where the experiment itself will take place. The vacuum chamber is designed around the requirement to have high optical access for both laser beams and imaging. In an optical lattice experiment the capability to carry out high resolution imaging of a low number of photons is needed to detect lattice sites containing a small number of atoms. To achieve high numerical aperture imaging without using optics within the vacuum chamber a large front window is required which must be as close as possible to the position of the MOT. To achieve this a homebuilt viewport design [75] is used along with a compact chamber. All other viewports are kept small in size[2] so that their centre can be positioned close to the front viewport. To allow flexible optical access for MOT, Raman, probe, pump and optical lattice beams 12 of such viewports are included as shown in Fig. 3.1.

To create a vacuum in the chamber the system is attached to a turbo pump with a rotary backing pump via the all metal valve. Before assembly all components and tools were carefully cleaned using a detergent (Decon or Neutracon 90) and solvent (acetone and methanol) in an ultra sonic bath. While still attached to the pumps the chamber was baked to a temperature of approximately 150 °C to drive out adsorbed gases from the surface of the metal. The Rb dispensers were activated by applying a current of 6 A to heat away the indium and argon seal, after which pure Rb metal is released upon continued heating. Once a final pressure of approximately 2×10^{-10} Torr was achieved, the system was removed from the turbo pump and the valves closed. After this the vacuum is maintained by the ion and getter pumps only.

3.2 Laser systems and optics setup

Laser light that is resonant with a variety of transitions in ^{87}Rb, as shown in Fig. 3.2, is required for the experiment presented in this thesis. The light that is required can be split into four functions: (a) MOT cooling and repump light at 780 nm; (b) far off-resonant 852 nm light for dipole trapping;

[2] CF16

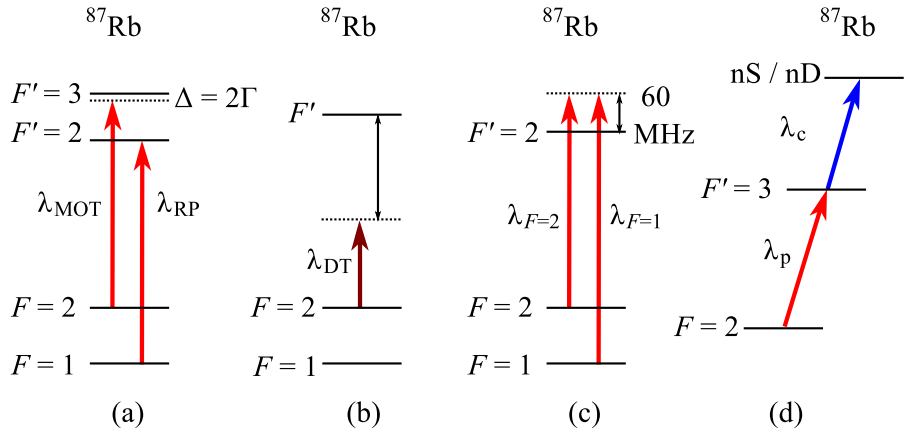

Figure 3.2: Laser frequencies required for the experiment. (a) MOT cooling and repump light for ^{87}Rb; (b) 852 nm light for the far off-resonance dipole trap. (c) Raman beams and (d) two-photon Rydberg excitation scheme.

(c) Raman beams 60 MHz detuned; and (d) two-photon Rydberg excitation consisting of a 780 nm probe and 480 nm coupling beam.

The MOT cooling light is 12 MHz red detuned from the 5s $^2S_{1/2}$ ($F = 2$) $\rightarrow$ 5p $^2P_{3/2}$ ($F' = 3$) transition and the repump resonant with the 5s $^2S_{1/2}$ ($F = 1$) $\rightarrow$ 5p $^2P_{3/2}$ (F'=2) transition in ^{87}Rb. These transitions at 780 nm can obtained from a single commercial diode laser[3] using an electro-optic modulator (EOM) as discussed in Chapter 4. The Raman beams may both be derived from the MOT cooling and repump beams with the aid of acousto-optic modulators (AOMs); by this means they are phase stable because they are stabilised to a single master laser. For the dipole trap a commercial 852 nm diode laser with a tapered amplifier[4] is used to give far-detuned light with a high power. Finally, the Rydberg excitation scheme requires a 780 nm probe beam, derived from the same source as the MOT cooling light, and a 480 nm coupling beam provided by a commercial frequency doubled laser system[5].

The laser system is summarised schematically in Fig. 3.3 giving details of the lasers and AOMs used for the experiment. The optics setup is designed around the need to create phase locked Raman beams produced from a single

[3]Toptica DL PRO
[4]Toptica TA 100
[5]Toptica TA SHG 100

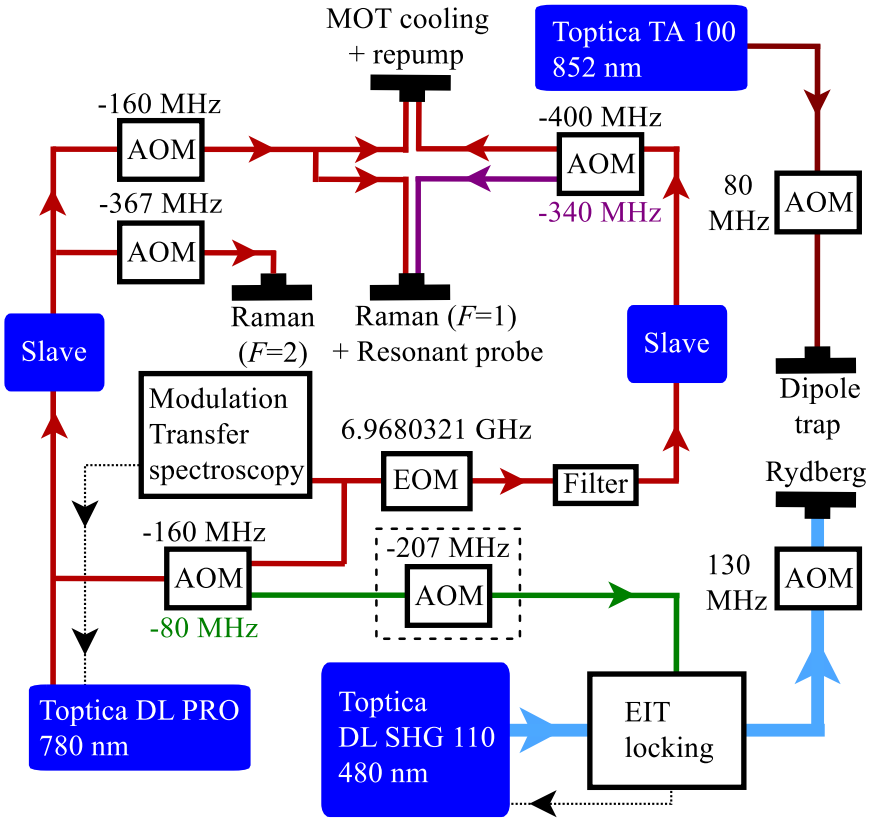

Figure 3.3: Schematic setup of the lasers and AOMs. The AOM enclosed by a dotted line is required only to lock the 480 nm Rydberg laser relative to the Raman beams instead of to the resonant probe beam.

master laser at 780 nm stabilised using modulation transfer spectroscopy. The master laser is set above resonance by locking with light double passed through an 80 MHz AOM. The master laser is locked to the ^{87}Rb cooling transition; further frequencies, those resonant with $F = 1 \rightarrow F'$ transitions, are generated from the sideband of an electro-optic modulator (EOM) set to the ground sate hyperfine splitting. Following the EOM the light is spatially split into its carrier and sideband components, using the technique detailed in Chapter 4. The sidebands produced by the EOM are only 2% of the carrier so in order to provide more laser power for the experiment both components are injected into slave lasers. Following this a variety of AOMs, detailed in Fig. 3.3, are used to produce light frequencies for cooling, repump, probe and Raman beams. All light is then coupled into polarisation maintaining fibres and sent to the vacuum system side of the experiment. In this way the laser

system remains separate from the vacuum chamber on an enclosed part of the optical bench minimising stray light and improving laser stability.

The Rydberg coupling laser provides an output of around 200 mW at 479 nm-486 nm. This laser is stabilised using cascade EIT in a vapour cell as described in Chapter 5. All of the coupling light available is propagated through the reference vapour cell maximising the power available for stabilisation. The cell has Brewster cut windows to optimise the amount of light transmitted. After this the Rydberg coupling light is single passed through an AOM and coupled into a polarisation maintaining fibre. In order that the light is on resonance with the required transition, after it is shifted by the AOM, the probe light used for stabilisation must be carefully selected. The Doppler mismatch between the 780 nm and 480 nm beams means that the probe detuning created by the AOM must be scaled by the ratio λ_c/λ_p to find the detuning of the coupling beam [61]. Consequently, within the vapour cell a probe detuned by 80 MHz produces a Rydberg coupling beam detuned by 130 MHz. The Rydberg coupling beam can then be brought onto resonance with the 5p $^2P_{3/2}$ ($F' = 3$) $\rightarrow$ nd ^2D or ns ^2S transitions using a 130 MHz AOM as shown in Fig 3.3. For experiments using the Raman beams the Rydberg coupling laser must be resonant with $5p^2P_{3/2}$ ($F' = 2$) + 60 MHz $\rightarrow$ nd ^2D or ns ^2S transitions. The probe beam used for stabilisation in the reference vapour cell must therefore be different to the probe beam used for EIT in an ultracold ensemble; this beam is created with an additional AOM, as shown in Fig. 3.3 surrounded by the dashed line.

The final part of the laser system is the dipole trapping light at 852 nm and a maximum power 750 mW. No stabilisation is required for this laser because it is far detuned from the Rb D_1 and D_2 lines. The 852 nm light is therefore simply single passed through an AOM, to provide a means of controlling the power, then coupled into a polarisation maintaining optical fibre. After this approximately 350 mW is available at the vacuum chamber for the dipole trap. After the fibre the power was found to vary by 1% which was found to produce a stable dipole trap without the need for power stabilisation.

For reference the optical setup used throughout this work is shown in detail in Appendix B. The application of this system to create a MOT and dipole trap is covered in the following sections.

3.3 Magneto-optic trap

The techniques of laser cooling are the corner stone of many modern atomic physics experiments and consequently led to the award of the 1997 Nobel Prize to Chu, Cohen-Tannoudji and Phillips [76–78]. The topic of laser cooling is covered in a variety of sources, Ref. [79] for example, so will be covered briefly here. The central idea of cooling atoms using laser light is that of the radiation pressure force. The force acting on an atom is the product of the photon momentum and the rate at which the photons are absorbed. The scattering rate of photons from a two level atom is given by [79]:

$$\Gamma_{\mathrm{s}} = \frac{\Gamma}{2} \frac{\Omega^2/2}{\Delta^2 + \Omega^2/2 + \Gamma^2/4}, \tag{3.1}$$

where Γ is the natural decay rate, Ω is the Rabi frequency and Δ is the detuning from resonance. The Rabi frequency can be related to the saturation intensity by $I/I_{\mathrm{SAT}} = 2\Omega^2/\Gamma^2$.

For every absorbed photon the atom receives a momentum kick in the direction of the photon's motion; momentum kicks from spontaneously emitted photons will be in random directions so will cancel to zero. This force can be used to slow atoms by employing counter-propagating beams. In this case the forces acting on the atoms will only balance if the they are at rest; at other velocities the Doppler shift will result an a force imbalance that will slow the atoms. The light is red-detuned from resonance; an atom moving in a direction opposite to the beam propagation will experience a Doppler shift that will bring the light closer to resonance. An increase in the rate of absorption will then produce a force that will slow the atom. For an atom moving in the same direction as the light propagation the converse will occur; the Doppler effect will shift the light further from resonance and the force will be reduced. The imbalance in the force can be written as [79]:

$$F_{\mathrm{molasses}} = -\alpha v, \tag{3.2}$$

with:

$$\alpha = 4\hbar k^2 \frac{I}{I_{\mathrm{SAT}}} \frac{-2\delta/\Gamma}{[1+(2\delta/\Gamma)^2]^2}. \tag{3.3}$$

This is a frictional force similar to that experienced by particles in a viscous fluid. Cooling atoms in this way was therefore referred to as an 'optical molasses' when it was first implemented experimentally [80].

The optical molasses technique can be extended by including a magnetic field gradient to create a magneto-optic trap (MOT) [81], the setup of which is shown in Fig. 3.4. A pair of anti-Helmhotz coils produces a field gradient across the beam overlap region. Away from the trap centre the magnetic field produces a spatially varying Zeeman shift of the magnetic sub-levels as shown in Fig. 3.4 (b). For an atom in the region where $z > 0$ the $m_F = -1$ state is shifted closer to resonance (the MOT beams are red-detuned); for absorption to take place on this transition the beam must circularly polarised to drive σ^- transitions. Absorption from this beam will give a scattering force that pushes the atom in a direction towards the centre of the trap. Where $z > 0$ the Zeeman shift and selection rules will favour absorption from the beam driving σ^+ transitions, again pushing the atoms towards the centre of the trap.

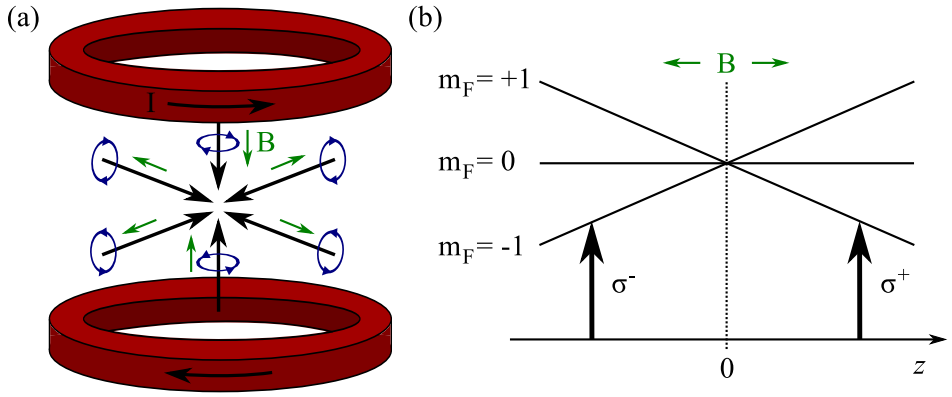

Figure 3.4: MOT operating principles. (a) Setup of orthogonal circularly polarised beams with anti-Helmholtz coils to generate the magnetic field gradient. (b) Magnetic field produces a spatially varying Zeeman shift. For $z > 0$ σ^+ transitions are closer to resonance; for $z < 0$ the σ^- transitions are shifted closer to resonance.

The coefficient of dependence of the Zeeman shift upon position may be written as [79]:

$$\beta = \frac{g\mu_{\mathrm{B}}}{\hbar}\frac{dB}{dz}, \tag{3.4}$$

where $g = g_{F'}m_{F'} - g_F m_F$, and dB/dz is the magnetic field gradient in the z direction. The force acting on the atoms is then:

$$F_{\mathrm{MOT}} = -\alpha v - \frac{\alpha\beta}{k}z, \tag{3.5}$$

where α is given by Eq. (3.3). The imbalance in the force produced by the Zeeman effect has therefore produced a restoring force with spring constant $\alpha\beta/k$. This will act to push the atoms cooled by the optical molasses effect towards the centre of the trap. This combination of cooling and trapping makes the MOT very efficient at loading atoms from a background vapour and is widely used in many experiments.

With the vacuum chamber and laser systems discussed in the previous sections in place it is possible to create a MOT. As the cooling transition in Rb is not closed the MOT cooling beams are combined with the repump generated as described in the previous section. Atoms are initially loaded into the MOT from a background vapour of Rb before being further cooled in a molasses as described later in Sec. 3.4.4. The MOT is set up in a standard six retroflected beam configuration popular in many atomic physics experiments. With this setup becoming increasingly common only the details specific to the work in this thesis are presented.

3.3.1 MOT beams

As mentioned previously the cooling and repump light required for the MOT is delivered to the chamber via optical fibres. A fibre splitter is used to create three MOT beams from a single input fiber and was found to be more effective over the use of separate fibres. Although a three fibre setup has the advantage of allowing the laser power in each beam to be adjusted independently it was found to be unstable. Over time the efficiency of the input coupling of light to each fibre changed by varying amounts giving a

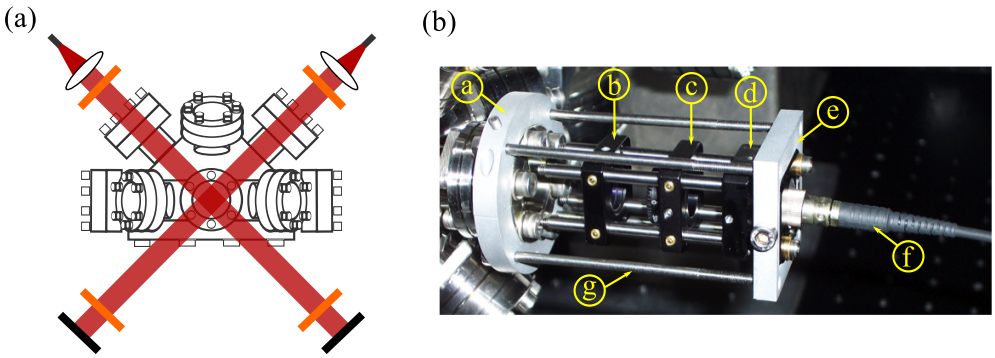

Figure 3.5: MOT optics setup. (a) The chamber shown from above along with four of the MOT beams. The final pair of beams are in a direction out of the page. Part (b) shows the custom built fiber dock and cage mount for the MOT optics. The labels are explained within the text.

drift in the power balance of the beams. This drift in power balance could be overcome by using a single fibre split into three output fibres[6]. Although the ratio of power in the three output beams was not perfectly balanced (of the total input power the three output powers were found to be 29%, 36% and 35%) and could not be adjusted, it was found to remain constant over long periods of time. Although the fibre splitter was not polarisation maintaining this was found to have little impact on the performance of the MOT. Overall, this setup produced a more stable MOT with good reproducibility compared to a MOT setup with three fibres.

Once at the chamber the MOT beams were arranged as shown in Fig. 3.5 (a). The diagram shows a view from above the vacuum chamber indicating the position of two pairs of horizontal retro-reflected beams. The third pair is in the vertical direction; out of the page in the diagram. The fibres are mounted in custom built docks attached directly to the viewports as shown in Fig. 3.5 (b). The cage assembly is clamped to the viewports by the retaining ring labelled ⓐ. To this retaining ring a rigid cage of metal rods, held by a plate labelled ⓔ, is attached to give a stable support structure for the optics. In order that the direction of the beams may be adjusted a second, smaller, cage is included. This is attached to plate ⓔ via a kinematic mirror mount so that the beam direction is manipulated by the adjustment screws. The

[6] Schäfter and Kirchhoff, FBS-780-4-33/33/33-APC-100-300

small cage and fiber, labelled ⓕ, are both mounted to the front plate of the kinematic mirror mount. This assembly then allows the required half inch diameter optics, an $f = 40$ mm lens and $\lambda/4$ waveplate, to be mounted to the small inner cage using commercial mounts. The beam is thus collimated to a radius of approximately 3 mm and the necessary circular polarisation obtained. The fibres are mounted by this rather complex method to provide high stability without the need for large support structures. This keeps the overall setup small and compact, hence maintaining good access for further components.

3.3.2 Magnetic field

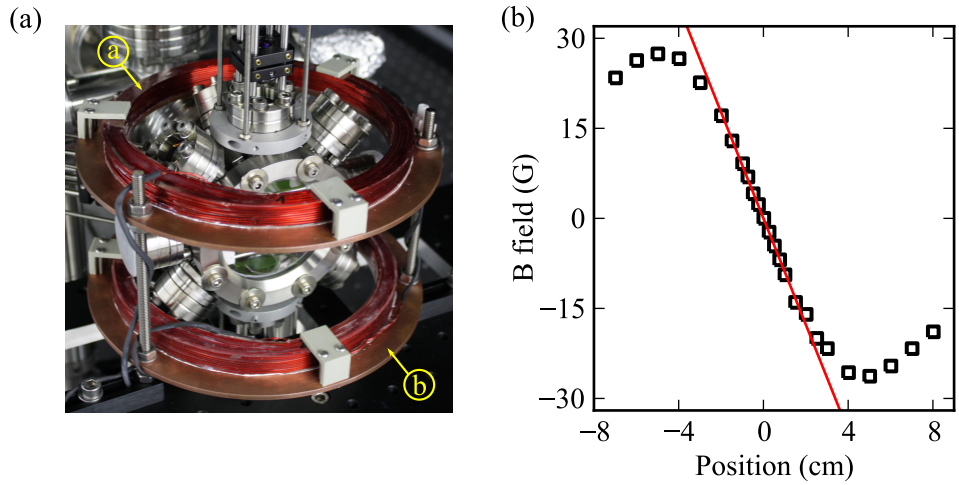

Figure 3.6: MOT coils setup. (a) The coils are labelled ⓐ and their copper heatsinks ⓑ. (b) Shows the magnetic field produced by the coils; the gradient of the central linear region is found to be 8.8 G/cm.

In order to create a MOT a magnetic field gradient across the beam overlap region is also required. This is produced by a pair of circular coils arranged in an anti-Helmholtz configuration. The position of the coils relative to the vacuum chamber is shown in the photograph of Fig. 3.6 (a). The coils themselves are labelled ⓐ and their copper heatsinks ⓑ. Each of the coils consists of 110 turns of insulated copper wire 1 mm in diameter held in place with epoxy adhesive. The magnetic field generated by these coils as a function of the position along an axis through their centre is shown in Fig.

3.6 (b). These data are measured using a Hall probe whilst 4 A of current is passing through the coils. The central portion of the data is clearly linear and is fitted accordingly giving a field gradient of 8.8 G/cm. At this current the coils reached a steady state temperature of approximately 80°C so water cooling was not required.

3.3.3 Imaging optics

Diagnostics are carried out on the MOT by imaging with a CCD camera. In order to have near single photon sensitivity for optical lattice experiments with small lattice site populations an EMCCD[7] camera was chosen. This provides low noise and includes electron multiplication (EM) gain for use with low light applications as is the case when imaging an optical lattice. The CCD is an array of 1004 × 1002 pixels each $(8\ \mu\text{m})^2$ in size. Light is collected and focused onto the CCD by the imaging optics shown in Fig. 3.7 (a). The principle design consideration here is the need to position the lens as close to the sample of ultracold atoms as possible. Hence, a 50 mm diameter $f = 40$ mm aspheric lens, labelled ⓐ in Fig. 3.7 (a), was used and fixed in a custom mount, labelled ⓑ. This lens is subsequently attached to a lens tube mounted onto a translation stage, labelled ⓒ and ⓘ respectively. Light collected from the MOT is hence collimated and must be focused onto the CCD; this is achieved using an $f = 100$ mm singlet lens, labelled ⓔ, attached to an adjustable mount, ⓕ and a second lens tube, ⓖ. This second lens tube is then attached to the camera housing using a third lens tube ⓗ. In order to correctly focus the image the two lens housings must be moved independently of each other; a sliding cover, labelled ⓓ, provides a join between the two lens mounts to eliminate stray light but still allows both lenses to move independently.

With the aspheric lens positioned so close to the front viewport of the vacuum chamber the retro-reflected MOT beams are clipped by the edge of the lens. To circumvent this problem the lens shape was cut, as shown in Fig. 3.7 (b), so that the MOT beams could pass unhindered. The lens mount was also cutaway so that more space was allowed for the beams. The specific

[7] Andor iXon 885 EMCCD

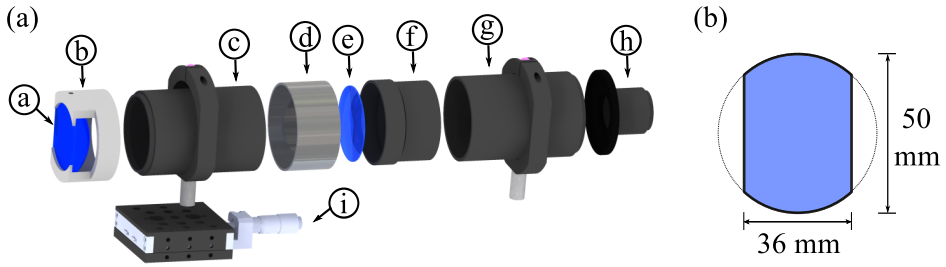

Figure 3.7: Imaging optics setup. (a) Pair of lenses mounted in a sequence of lens tubes collimate light from the MOT and focus it onto the CCD chip, all labels are described in the text. (b) dimensions of the collimating lens showing the modification in its shape made so that the MOT beams may pass without being blocked when the lens is close to the position of the MOT.

dimensions of the lens are given in Fig. 3.7 (b) and with this modified shape light is collected over a solid angle of $\Omega = 0.071$ at a working distance of 34 mm.

The resolution of the system was measured by imaging a 1951 USAF resolution test chart giving a resolution of 15.63 μm. The image size was calibrated by again recording an image of the resolution test chart. A single pixel was found to correspond to a distance of 3.13 μm; with an actual pixel size of 8 μm this gives a magnification of $M = 2.56$. The optics system can be modified by replacing the $f = 100$ mm lens to achieve a greater magnification if required.

3.3.4 MOT experimental sequence

With the MOT successfully achieved in a continuously loading steady state mode it is then possible to employ a controlled timing sequence implemented using LabVIEW. With this control in place the atoms can be loaded into the MOT over a defined period of time then a molasses phase applied to cool them further. Diagnostics are then carried out by imaging the cloud of atoms. The LabVIEW routine controlling this sequence is shown schematically in Fig. 3.8.

Atoms are trapped during the MOT loading phase, labelled ⓐ in Fig. 3.8. The MOT is loaded for around 3–15 s with the MOT cooling beams tuned to

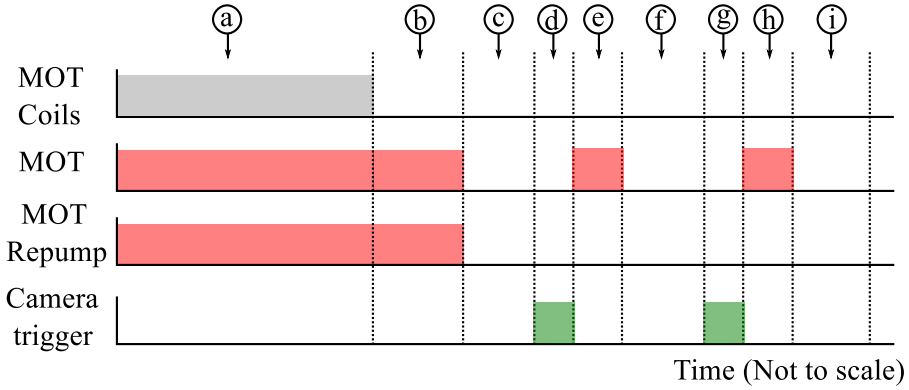

Figure 3.8: MOT loading sequence. Labels are explained in the text. Atoms are loaded into the MOT and then further cooled during a molasses phase. After this the atoms are imaged by illuminating the sample using the MOT cooling light now set to resonance and collection fluorescence light at the camera. Finally a second image is taken without the atoms to act as a measure of the background light level not attributed to the fluorescence of the atoms.

12 MHz below resonance and the repump on resonance; approximately 6 mW of cooling light is available in each beam along with a repump power of a 150 μW. During this time the MOT coils producing the magnetic field are on. Once atoms are loaded into the MOT a molasses phase, ⓑ, lasting 7 ms follows. The sub-Doppler cooling achieved by the molasses is explained later in Sec. 3.4.4. The magnetic gradient is switched off and the cooling beam detuning ramped linearly from resonance to 40 MHz red-detuned. At this stage the atoms are released from the trap and allowed to expand freely; the sample can then be prepared further in a manner specific to the experiment being carried out as detailed in later chapters.

For diagnostic purposes the atoms are allowed to freely expand, in period ⓒ in Fig. 3.8, before they are imaged using the CCD camera. The imaging process begins with a TTL pulse, of 100 μs duration, being sent to the camera in phase ⓓ to begin collecting charge on the CCD. Following this, during ⓔ, the sample of atoms is illuminated using the MOT cooling light, now set to resonance, and the fluorescence produced is collected by the imaging optics. The exposure time is 300 μs allowing adequate fluorescence light to be collected without the sample expanding and blurring the image. After the CCD has been exposed, a 1 s read out period, labelled ⓕ, is allowed so that

the data may be transferred from the CCD chip. As some stray scattered light will be incident on the CCD the image must be calibrated by taking a second background image. After the 1 s read out period all of the atoms will have left the region of the image and so can no long contribute fluorescence light if illuminated a second time. The image process is hence repeated with a second trigger, labelled ⓖ, and exposure time, ⓗ, to record a background image. After a second read out phase, labelled ⓘ, the images are subtracted to leave only an image of the fluorescence light from the atoms.

3.4 MOT characterisation

Once the MOT is set up to the design detailed in the previous sections its behaviour must be characterised and optimised using a range of well established methods. Firstly, the rate at which atoms are loaded into the MOT is measured and the Rb dispenser current optimised. The temperature of atoms in the MOT is measured using a time of flight technique and the molasses phase optimised to give an efficient reduction in temperature. Absorption measurements are then carried out to find the atom number and calibrate the quantisation magnetic field.

3.4.1 MOT loading

The rate at which atoms are loaded into the MOT can be measured by recording fluorescence using a photodiode. Light from the MOT is focused onto a photodiode and the level of fluorescence recorded as a function of time between the magnetic coils being switched on and when the number of atoms trapped in the MOT reaches a steady state. The rate at which atoms are loaded into the MOT is heavily dependent on the number of atoms in the background vapour produced by the dispensers. The loading rate of the MOT is therefore found with various currents passing through the dispensers in order to evaluate their performance.

Typical MOT loading curves are presented in Fig. 3.9 (a) at dispenser currents varying in a range between 4.4 and 5.0 A. The rate at which the MOT loads is clearly increased when the dispenser current is increased; at a higher

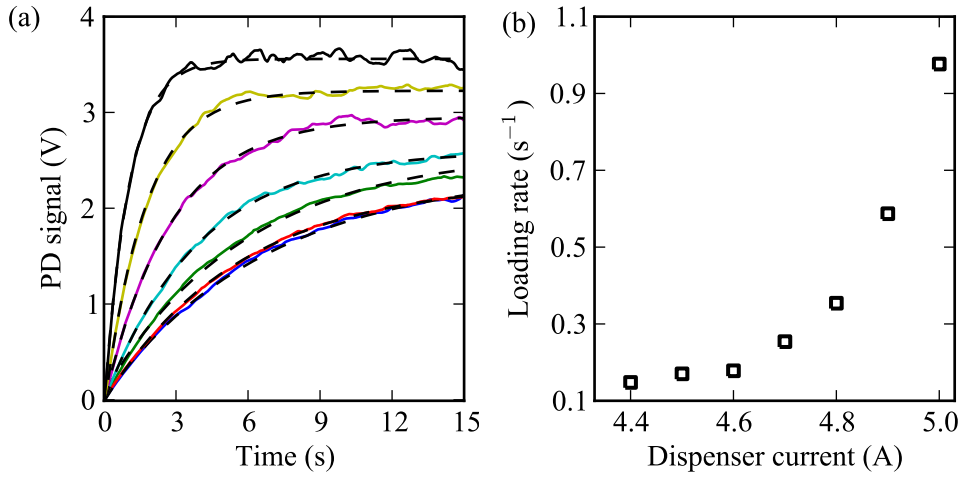

Figure 3.9: MOT loading rate optimisation. (a) MOT loading curves for various dispenser currents measured by recording fluorescence at a photodiode. The data are fit using the exponential function in Eq. (3.6). (b) Time constants of the MOT loading rate as a function of the dispenser current.

current the dispenser is heated to a higher temperature thus increasing the number of atoms emitted into the background vapour from which the MOT is loaded. The loading curves are fitted with a exponential function:

$$S(t) = R(1 - e^{-\beta_L t}), \tag{3.6}$$

where $N(t)$ is the number of atoms in the MOT, which is proportional to the fluorescence signal measured at the photodiode, and t is the time elapsed after the loading began. The loading rate associated with each curve is given by the parameter β_L. The loading rate is shown as a function of the dispenser current in Fig. 3.9 (b). The rate at which atoms are loaded into the MOT is found to rise rapidly above a dispenser current of 4.6 A. Typically the MOT was run with a dispenser current of 4.85 A; at higher currents, approaching 5 A, fluorescence of atoms in the background vapour was found in images of the MOT indicating that the background pressure of Rb was too high and will affect the dipole trap lifetime due to collisions with the background gas.

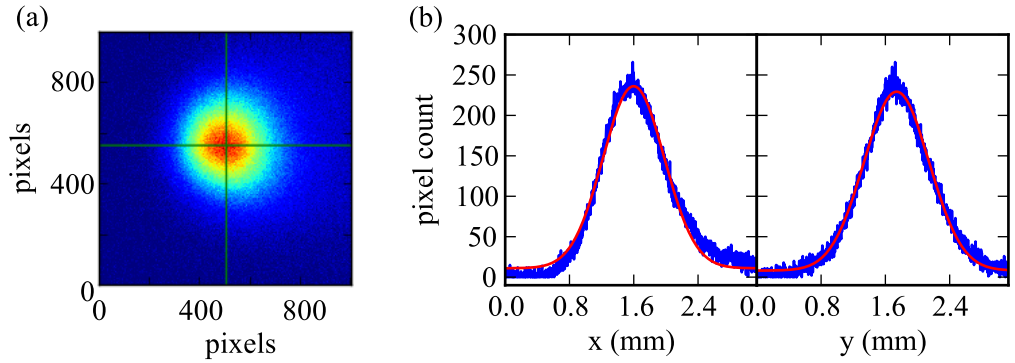

Figure 3.10: MOT fluorescence image analysis. (a) Example CCD camera image of the MOT. The data are sliced through the x and y-dimension at the point where the pixel count is greatest corresponding to the centre of the cloud. (b) Horizontal and vertical cuts through the data in (a). The pixel number is re-scaled into a position in mm and the data are fit using a Gaussian function.

3.4.2 Image analysis

An example of a fluorescence image of the MOT, taken using the imaging system described in the previous section, is shown in Fig. 3.10 (a). The centre of the MOT, the point of greatest density, is found by locating the pixel with the highest photon count. Slices of the image are then found through this point in a horizontal and vertical direction as shown by the green lines in Fig. 3.10 (a). These slices are shown in panel (b) with a Gaussian fit to the data. The distance axis is scaled using the imaging optics calibration already discussed in section 3.3.3, thus allowing the radius of the cloud to be found.

The number of atoms present in the image can be evaluated from the total level of fluorescence detected at the CCD. The number of counts detected by the CCD will be related to the rate at which photons are scattered by the atoms, which was given by:

$$\Gamma_s = \frac{\Gamma}{2} \frac{I/I_{\mathrm{SAT}}}{1 + I/I_{\mathrm{SAT}} + 4\Delta^2/\Gamma^2}, \tag{3.7}$$

as described in Sec. 3.3. In this case the light is on resonance so $\Delta = 0$. As the atoms are illuminated by the circularly polarised MOT beams various

transitions between different m_F states are possible; this can be taken into account by the use of an effective saturation intensity, $I_{\mathrm{SAT}} = 3.6$ mW/cm^2 taken from Ref. [82]. The intensity of the MOT beams is found using $I = 2P/\pi\omega_0^2$, where P is the power and ω_0 the beam waist ($P = 5.9$ mW and $\omega_0 = 4.1$ for this experiment). The number of counts produced by the CCD will depend on the optics used to focus the light and the properties of the CCD itself; if the total number of counts detected by the CCD in a time t is given by Σ then the atom number may be found using:

$$N = \frac{\Sigma c}{q\Omega T \Gamma_{\mathrm{s}} t}, \tag{3.8}$$

where q is the quantum efficiency of the CCD, c is the number of electrons produced per count, Ω is the solid angle over which photons are collected by the imaging optics, T is the transmission of the optics and Γ is the rate at which photons are scattered. For the optics and CCD used in this experiment these values are: $q = 0.45$; $c = 1.43$; $\Omega = 0.071$; $T = 1$, and $t = 3$ ms. By evaluating Eq. (3.8), approximately 5×10^5 atoms are found to be loaded into the MOT.

3.4.3 Time of flight measurement

An important property of the atoms trapped in the MOT is their temperature. This can be measured using the time of flight measurement (TOF) [83][84] technique where the cloud of atoms is allowed to expand freely and its size measured over time. Figure 3.11 shows a sequence of images of the MOT after different expansion times. The MOT clearly expands over time and is seen to fall under the influence of gravity.

Initially the cold atoms will exhibit a Gaussian position distribution,

$$P(z_i) = \frac{1}{\sqrt{2\pi}\omega_z} \exp\left(\frac{-z_i^2}{2\omega_z^2}\right), \tag{3.9}$$

where only the 1D distribution of atoms in the z-direction is considered. The velocity distribution be Maxwell-Boltzmann in form as given by:

$$f(v_z) = \left(\frac{m}{2\pi k_B T_z}\right)^{1/2} \exp\left(\frac{-mv_z^2}{2k_B T_z}\right), \tag{3.10}$$

where T_z is the temperature and m the mass of atoms in the sample. As the cloud expands over a period of time, t, the position, z_f, of an atom is given by:

$$z_f = z_i + v_z t. \tag{3.11}$$

This can be combined with Eq. (3.10) to give:

$$f(v_z) = \left(\frac{m}{2\pi k_B T_z}\right)^{1/2} \exp\left(\frac{-m(z_i - z_f)^2}{2k_B T_z t^2}\right), \tag{3.12}$$

The position distribution as a function of time is then:

$$P'(z_f, t) = \int_{-\infty}^{+\infty} P(z_i) f(v_z) dz_i, \tag{3.13}$$

$$= \int_{-\infty}^{+\infty} P(z_i) f\left(\frac{z_f - z_i}{t}\right) dz_i, \tag{3.14}$$

$$= P(z_i) \star (v_z). \tag{3.15}$$

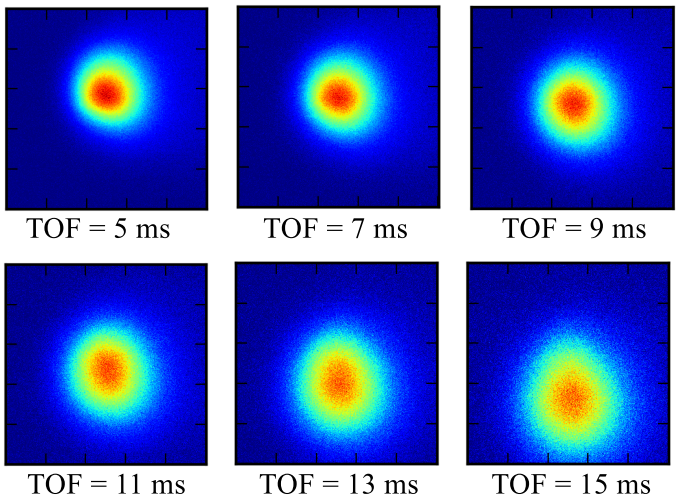

Figure 3.11: Example time of flight (TOF) sequence. The cloud of atoms released from the MOT is allowed to freely expand for a varying time before a fluorescence image is taken. The cloud is clearly seen to expand over time and fall under gravity.

The final position distribution is therefore the convolution of the initial distribution and velocity distribution. As these distributions are both Gaussian the final distribution will also be a Gaussian with a width given by the quadrature sum of their widths. From equations Eq. (3.9) and Eq. (3.12) the width of the cloud as it expands is:

$$\sigma_z(t) = \sqrt{\sigma_{z_i}^2 + \frac{k_B T_z}{m} t^2}. \tag{3.16}$$

By making a plot of the Gaussian width of the cloud for different expansion times and fitting it with Eq. (3.16) the values of the initial width of the cloud, σ_{z_i}, and the temperature can be found. The longest time the TOF measurement can be made over is limited by the time taken for the MOT to expand out of the field of view of the camera. An example of a TOF measurement is shown in Fig. 3.12.

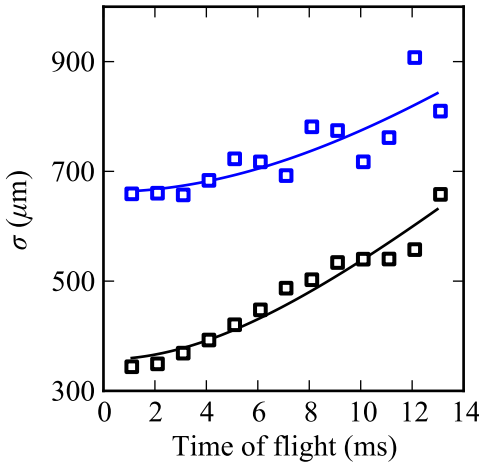

Figure 3.12: Example TOF measurement. The blue and back data show the size of the cloud, in the vertical and horizontal directions respectively, as it expands over time. The data are fit using Eq. (3.16) to extract the temperature.

3.4.4 Optical Molasses

The temperature to which atoms may be cooled using the radiation pressure force is limited by random fluctuations in the force due to spontaneous emission and the rate at which photons are absorbed. At very low temperatures the momentum kick caused by spontaneous emission leads to the atom experiencing a random walk in velocity. As the rate at which absorption occurs is random the number of photons absorbed in a fixed time will vary according to Poissonian statistics and again lead to a random walk. The equilibrium temperature occurs when this diffusive heating and cooling force balance giving the Doppler cooling limit of [79]:

$$k_{\mathrm{B}}T = \frac{\hbar\Gamma}{2}. \tag{3.17}$$

Early work on laser cooling soon discovered that temperatures significantly below this limit could be produced. This discrepancy between theoretical predictions and experimental observation was explained by new cooling mechanisms introduced by Dalibard and Cohen-Tannoudji [85] and Chu *et al.* [86]. These studies showed that sub-Doppler temperatures could be achieved using polarisation gradients created in the standing waves created by a pair of molasses beams. Two types of polarisation gradient may occur, each linked with a different cooling mechanism: for a pair of orthogonal linearly polarised beams a so called Sisyphus effect occurs because of the spatial modulation in the light shift of the Zeeman ground state sub-levels; for a pair of circularly polarised beams a motionally dependent population difference occurs.

In the case of a pair of counter-propagating linearly polarised beams the resulting polarisation of the standing wave will vary between circular and linearly polarised over a distance equal to half of one wavelength. This modulation produces an oscillating light shift of the ground state Zeeman sub-levels across the standing wave. If we consider the simple case of a two-level atom with ground state angular momentum $J = 1/2$ and excited state $J = 3/2$; the ground state will be split into two Zeeman sub-levels $g_{-1/2}$ and $g_{+1/2}$; the excited state correspondingly has four sub-levels. In a region of σ^- polarisation atoms will be optically pumped to the $g_{-1/2}$ state and in regions of σ^+ polarisation the converse is true and optical pumping occurs into the

$g_{+1/2}$ state. At a position where the light polarisation is linear both sub-levels will be equally populated. For an atom at rest, the modulation of the light shift and optical pumping result in the steady state population always residing in the lower of the Zeeman sub-levels. The key to understanding how this results in a cooling mechanism is that the optical pumping takes a finite time to occur. A moving atom will experience a series of potential maxima and minima (hills and valleys) because of the differing light shift, as shown in Fig. 3.13. If one considers an atom beginning at a valley in the potential it may move up the potential hill, losing kinetic energy as it does so, but remaining in the same Zeeman sub-level. Once it reaches the top of the potential gradient it will be pumped to the other sub-level, *i.e.* the next minimum in the potential. The time delay for the optical pumping to occur therefore results in the atom experiencing a continuous climb in potential; kinetic energy is consequently lost and the atom cooled.

In the case of a pair of counter-propagating circularly polarised beams the nature of the polarisation gradient is different. Here the polarisation is linear throughout the standing wave and rotates in orientation such that it forms a helix. Stationary atoms will have population distributed evenly over all the ground state Zeeman sub-levels. Only when an atom is in motion

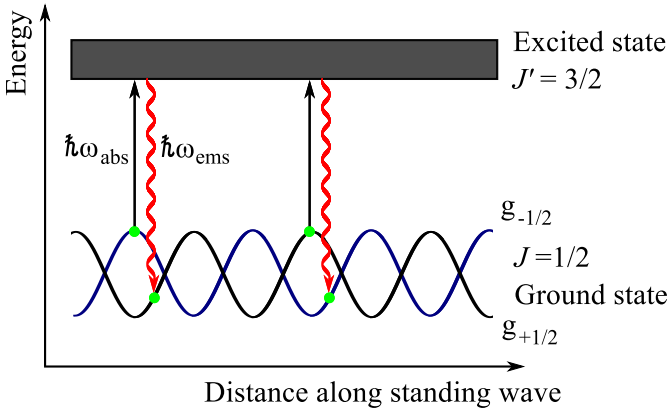

Figure 3.13: Cooling mechanism created by a periodic shift in energy of the Zeeman sub-levels. The atoms are made to travel through maxima and minima in the potential. If an atom absorbs a photon at a potential maximum it can decay back to a potential minimum by spontaneous emission. The atom therefore continuously climbs the potential gradient losing kinetic energy. Figure adapted from Ref. [79]

is this symmetry broken; moving towards the σ^+ beam brings it closer to resonance and population is optically pumped towards positive g_J states. The atoms now have a motionally distributed population which results in a greater difference between the scattering rate from each beam. Consequently, the frictional force that cools the atoms is stronger and the Doppler cooling limit may be overcome.

In reality, a combination of these processes occurs in the complex polarisation gradients produced by three orthogonal beam pairs. A molasses is typically implemented after atoms have been collected in the MOT to provide further cooling to sub-Doppler temperatures. During the molasses phase the MOT magnetic field gradient must be switched off and the Earth's magnetic field carefully cancelled using shim coils, only then can the Zeeman sub-levels be manipulated in the way required for the cooling mechanism described earlier.

In order to optimise the molasses phase of the experiment its parameters were altered and the temperature of the atom cloud measured as previously described. A critical factor in achieving a low temperature was the duration of the molasses. The change in temperature as a result of varying molasses times is shown in Fig. 3.14. The first datum has a large errorbar because at this temperature the MOT expands quickly out of the imaging region.

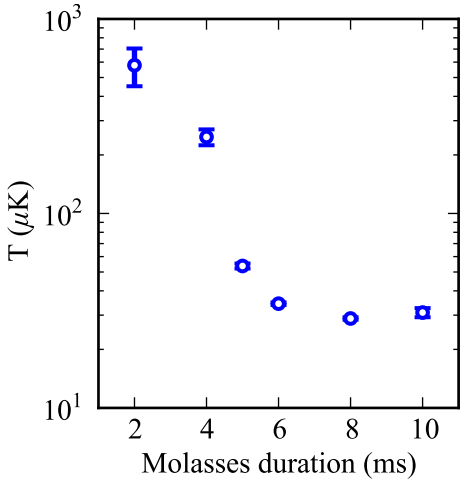

Figure 3.14: Temperature of the MOT after a varying molasses duration. The error bars show the standard deviation of a repeat of three measurements. The minimum temperature achieved is around 20 μK and the optimal molasses duration around 7 ms.

Therefore the TOF measurement can only be made for short times and consequently the fit with Eq. (3.16) is less reliable. The minimum temperature achieved is around 20 μK after a molasses duration of approximately 7 ms.

3.4.5 Absorption measurements

In order to obtain an atom number and calibration of the quantisation magnetic field an absorption measurement of atoms released from the MOT was made. A weak probe beam resonant with the 5s $^2S_{1/2}$ ($F = 2$) $\rightarrow$ 5p $^2P_{3/2}$ ($F' = 3$) transition was focused at the position of the MOT to a waist of $\omega_0 \sim$100 μm and detected using a high bandwidth photodiode. The frequency of the probe is scanned over resonance in approximately 1 ms using a voltage ramp applied to the AOM. Hence, an absorption spectrum is measured that is proportional to the number of atoms in the MOT and the magnetic field can be evaluated by observing a Zeeman shift.

An example absorption spectrum is shown in Fig. 3.15. The intensity of the probe is $I/I_{\mathrm{SAT}} = 4.78$ and the photodiode data are normalised using a background measurement to give the transmission in absolute units. The data are fit using the exponential of a Lorentzian shown by the black line.

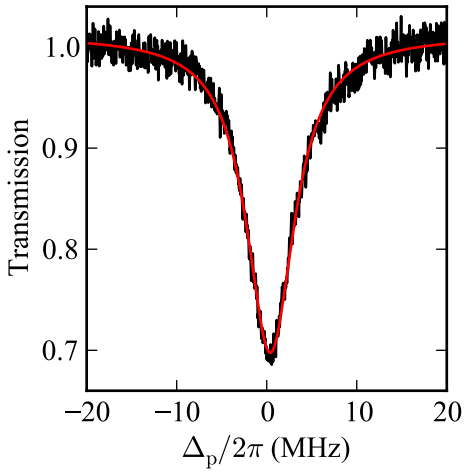

Figure 3.15: Absorption of a probe beam scanned over resonance with the ^{87}Rb cooling transition as atoms are released from the MOT. The data are normalised using a background measurement to give the transmission that is fit using a Lorentzian function (black line).

If one considers a probe beam, travelling in the y-direction, incident upon a cloud of atoms the intensity is reduced by those atoms scattering photons. For small intensities, where $\Omega \ll \Gamma$, the reduction in intensity will be given by the Beer-Lambert law:

$$I = I_0 e^{-\mathrm{OD}}, \tag{3.18}$$

where I_0 is the incident intensity, I is the intensity measured at the detector and OD is the optical depth. The optical depth is dependent on the scattering cross section, σ, and the number of atoms the light impinges on. The scattering cross section is given by the fraction of scattered power to incident intensity:

$$\sigma = \frac{P_{\mathrm{atom}}}{I} = \frac{\hbar\omega\Gamma_{\mathrm{s}}}{I} = \frac{\sigma_0}{1 + \left(\frac{2\Delta_{\mathrm{p}}}{\Gamma}\right)^2 + 2\left(\frac{\Omega}{\Gamma}\right)^2}, \tag{3.19}$$

where Γ_{s} is given by Eq. (3.1) so that σ_0 is the on-resonance cross section:

$$\sigma_0 = \frac{\hbar\omega\Gamma}{2I_{\mathrm{SAT}}}, \tag{3.20}$$

and $I/I_{\mathrm{SAT}} = 2\Omega^2/\Gamma^2$. The optical depth can now be written as:

$$\tau = \sigma \int_{-\infty}^{+\infty} n(x, y, z) dy, \tag{3.21}$$

with the spatial distribution of atoms given by $n(x, y, z)$ and the integral over the y-coordinate only because that is the direction of the beam propagation. The spatial distribution of the cloud of atoms is given by a three dimensional Gaussian function:

$$n(x, y, z) = n_0 \exp\left(-\frac{x^2}{2\sigma_x^2} - \frac{y^2}{2\sigma_y^2} - \frac{z^2}{2\sigma_z^2}\right), \tag{3.22}$$

where

$$n_0 = \frac{N_0}{(2\pi)^{3/2}\sigma_x\sigma_y\sigma_z}. \tag{3.23}$$

Here σ_x, σ_y and σ_z are the widths of the Gaussian distribution in each spatial dimension and N_0 is the total number of atoms. The optical depth on-resonance may now be written as:

$$\tau_0 = \frac{\sigma_0 N_0}{2\pi\sigma_x\sigma_y}, \tag{3.24}$$

Combining this with Eq. (3.18) gives an expression for the atom number:

$$N_0 = -2\pi\sigma_x\sigma_y\frac{\ln\left(I/I_0\right)}{\sigma_0}. \tag{3.25}$$

The value of I/I_0 is the peak transmission found from the data in Fig. 3.15 and the radii of the cloud may be obtained from the time of flight measurement. The measurement in Fig. 3.15 corresponds to an atom number of approximately 6×10^6. This atom number differs from that found from the fluorescence measurements, the discrepancy can be account for by the error on each result.

3.4.6 Magnetic field calibration

In order to obtain a well defined polarisation of beams directed at atoms released from the MOT a quantisation magnetic field must be applied. This field is small so that the magnetic sub levels remain approximately degenerate, but provides a common reference that allows the orientation of the light polarisation to be defined. The magnetic field is applied using one of the pairs of shim coils that are included in the setup to cancel the Earth's magnetic field. The field is applied only for the time when the atoms released from the MOT are to be optically pumped or interrogated by the probe. In order to calibrate the quantisation field the absorption measurement of the previous section is carried out with various magnetic fields applied and the shift in resonance extracted by fitting the data.

The Zeeman shift for various shim coil currents is presented in Fig. 3.16. The data are the result of five repeated measurements and the error bars are the standard error on the mean. The Zeeman shift is linear, as shown by the straight line fit in Fig. 3.16, with the magnetic field dependance given by:

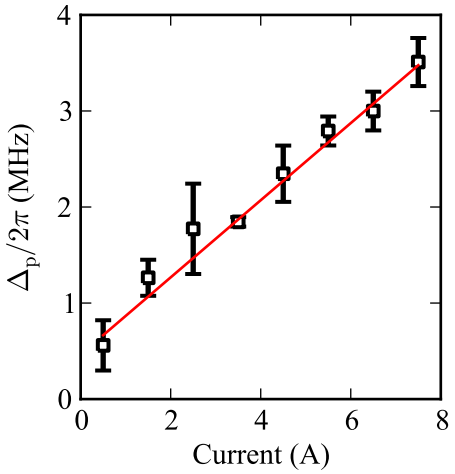

Figure 3.16: Zeeman shift as a function of shim field current. The data are the average of five repeated measurements and the error bars represent the standard error. The red line is a linear fit to the data.

$$h\Delta\nu = \mu_B(m_{F'}g_{F'} - m_F g_F)B, \tag{3.26}$$

where μ_B is the Bohr magneton and B is the applied magnetic field.

As the probe beam is scanned over resonance with the 5s $^2S_{1/2}$ ($F = 2$) $\rightarrow$ 5p $^2P_{3/2}$ ($F' = 3$) transition the relevant g-factors are: $g_{F'} = 2/3$ and $g_F = 1/2$. The probe light is σ^+ polarised so that the dominant absorption will be on the $F = 2, m_F = +2 \rightarrow F' = 3, m_F = +3$ transition. From the gradient of the linear fit in Fig. 3.16 and Eq. 3.26 the magnetic field is found to be related to the current by : B (G)$= (0.29 \pm 0.02) \times I$ (A) .

3.5 Dipole trap

Optical dipole traps confine neutral atoms using the electric dipole interaction with far-detuned light [87]. The depth of traps made in this way is comparatively low, typically no greater than 1 mK. Hence, in order for atoms to be trapped by the potential they must first be cooled by means of a MOT and molasses. The key advantage of the dipole trap is that the ground state dynamics of the atoms remain available for carrying out experiments. The use of the dipole force to demonstrate a trap for neutral atoms was first

achieved by Chu *et al.* [88]; sodium atoms cooled by an optical molasses were trapped using a strongly focused beam detuned several hundred gigahertz below resonance with the D_1 transition. After this initial breakthrough much progress has been made enabling dense, cold samples of atoms to be loaded into shallow dipole traps.

The optical dipole force is created by the dispersive interaction of the induced dipole moment and intensity gradient of the light. The dipole potential and scattering rate are given by Ref. [87] as:

$$U_{\mathrm{dip}}(r) = \frac{3\pi c^2}{2\omega_0^3}\frac{\Gamma}{\Delta}I(r), \tag{3.27}$$

$$\Gamma_{\mathrm{sc}}(r) = \frac{3\pi c^2}{2\omega_0^3}\left(\frac{\Gamma}{\Delta}\right)^2 I(r). \tag{3.28}$$

These equations describe the the two fundamental features that make dipole trapping possible. Firstly, if the light field is red-detuned, *i.e.* $\Delta < 0$, the sign of the potential is negative. This allows one to create a potential minimum, where atoms may be trapped, at the point of greatest intensity, corresponding to the focus of a Gaussian beam. Alternatively, above resonance the dipole potential is positive and atoms will be forced away from positions of high intensity. Atoms in a blue-detuned trap are therefore trapped at points of minimum light intensity.

The second feature of Eqs. (3.27) and (3.28) that must be noted is the nature of the scaling with detuning and intensity: the potential scales as I/Δ whereas the scattering rate is proportional to I/Δ^2. Therefore, at large detuning and intensity the scattering rate can be kept as low as possible for the required trap depth.

Once the atoms are cooled using the MOT and molasses techniques described in the previous sections they may be loaded into an optical dipole trap. The trapping potential is created using a far-red-detuned beam that is tightly focused at the centre of the MOT.

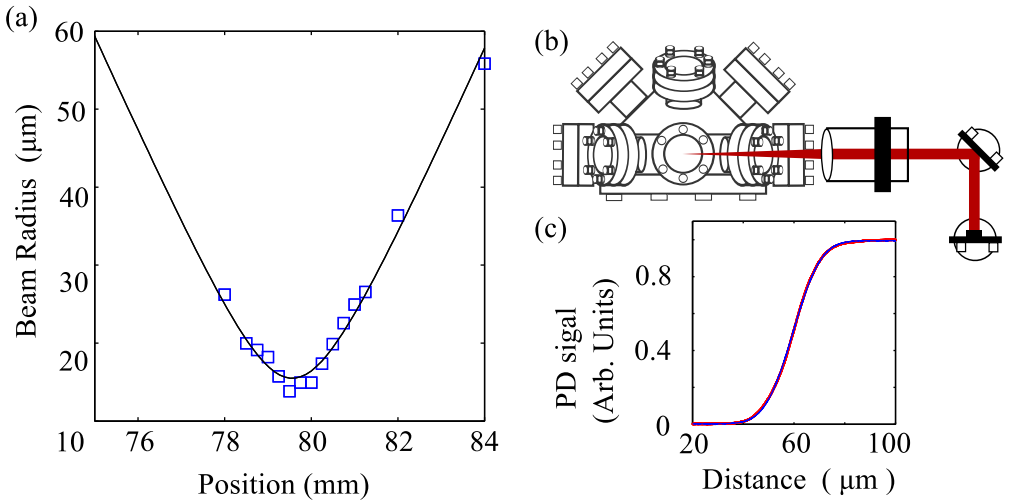

Figure 3.17: (a) Measurement of the waist of the dipole trap beam. The radius of the beam is measured at different positions from the lens and fit with a Gaussian beam profile to extract the waist. (b) Layout of the dipole trap beam optics. (c) Knife edge measurement of the beam radius.

3.5.1 Experimental setup

In order to realise the dipole trap experimentally a 350 mW beam of 852 nm light is employed. The laser is set up with an 80 MHz single pass AOM and coupled to an optical fibre as shown in Fig. 3.3. The AOM allows the amount of light reaching the chamber to be controlled and provides fast switching. Light was delivered to the chamber using the set up shown in Fig. 3.17 (b). The fibre coupler and mirror were mounted in high stability mounts[8] to improve the directional stability of the beam. The mirror is a dichroic designed to transmit the 480nm light, which is required for coupling to Rydberg states, while reflecting the 780 nm probe light and 852 nm dipole trap light. This allows all beams required for the experiment to propagate along the same axis. The dipole trap light was focused using an AR coated $f = 80$ mm plano-convex lens. The waist of the beam was found using a knife edge technique; the intensity of the beam is measured as a knife edge is translated through the beam giving the plot in Fig. 3.17 (c). This is then fitted with an error function to extract the waist of the Gaussian beam. This measurement was repeated at different distances from the lens to find

[8]Fine Adjustment Saturn series 1" mounts

its focus, as shown in Fig. 3.17 (a). At the focus the waist was measured to be 15.5 μm and the focal length 79.5 mm. The focus of the beam was initially aligned to the position of the MOT by using resonant light to deplete the MOT atom number. Whilst observing the MOT loading continuously the beam was aligned such that the maximum depletion occurred indicating that the focus of the beam was close to the centre of the cloud.

With these parameters the depth of the potential, for an alkali-metal atom such as Rb, maybe found using [89]:

$$U_0 = \frac{\hbar \Gamma I}{24 I_{\mathrm{SAT}}} \left(\frac{1}{\delta_{1/2}} + \frac{2}{\delta_{3/2}} \right), \tag{3.29}$$

where Γ is the natural decay rate, I is the laser intensity given by $I = 2P/\pi\omega_0^2$ and I_{SAT} is the saturation intensity found using $I_{\mathrm{SAT}} = 2\pi^2\hbar c\Gamma/(3\lambda^3)$. The values of $\delta_{1/2}$ and $\delta_{3/2}$ are the difference between the laser frequency and the frequency of the D_1 and D_2 transition frequencies (in units of Γ). With the dipole trap parameters above the well depth is $U_0/k_{\mathrm{B}} = -4$ mK.

The experimental sequence required to load atoms into the dipole trap is shown in Fig. 3.18. The dipole trap beam is on during the MOT loading and molasses phases, labelled ⓐ and ⓑ, to trap atoms in the optical potential.

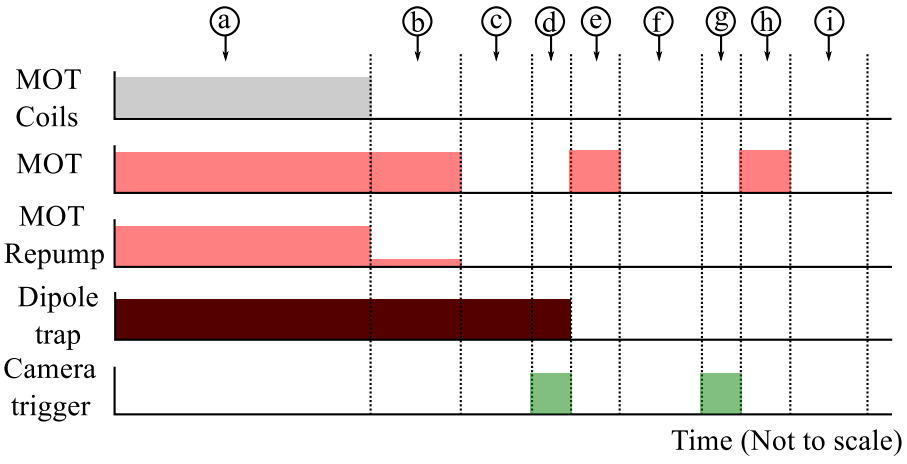

Figure 3.18: Experimental sequence implemented to load atoms into the dipole trap. The MOT loading sequence is the same as discussed previously except that the repump light intensity is reduced during the molasses. The labels are identified in the text.

The power of the repump light is reduced during the molasses phase in order to increase the dipole trap loading rate [89]. After the molasses any atoms remaining in the MOT that are not trapped by the optical potential are allowed to fall away during a 35 ms period where only the dipole trap light is on, labelled ⓒ in Fig. 3.18. The imaging then proceeds as discussed in section 3.3.4 with a trigger, ⓓ, followed by an exposure time where both MOT and repump beams are on, ⓔ. The repump must be on when the cloud is imaged to ensure atoms in both the $|F = 1\rangle$ and $|F = 2\rangle$ are detected. The imaging routine is then completed with: a readout delay, ⓕ; second trigger, ⓖ; background exposure, ⓗ; and a final readout period, ⓘ.

3.5.2 Dipole trap characterisation

After atoms are loaded into the dipole trap they are imaged in a similar way to atoms in the MOT as described in section 3.4.2. An exposure is taken over 3 ms where the trapped atoms are illuminated with the MOT and repump beams and fluorescence detected at the CCD camera. An example image of the dipole trap is shown in Fig. 3.19 (a); the data have been smoothed by applying a five point moving average and the point of greatest density is

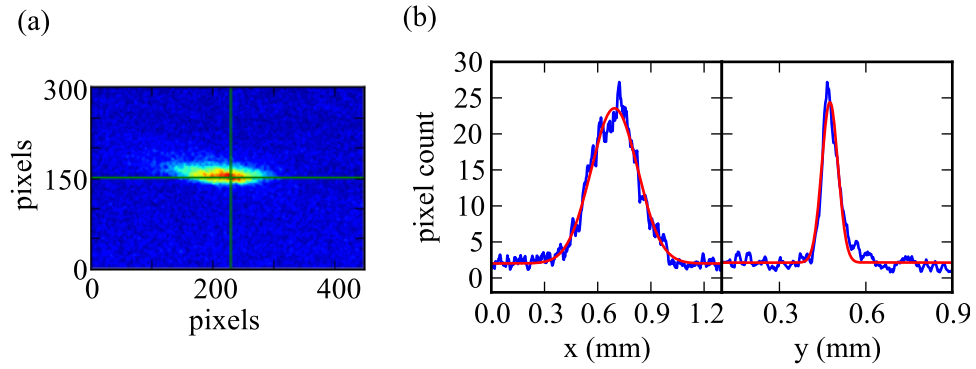

Figure 3.19: Dipole trap fluorescence image analysis. (a) Example image of atoms loaded into the dipole trap. The data have been smoothed using a five point moving average and the green lines indicate the point of greatest density. Slices through the data along the green lines are shown fit with Gaussian functions in panel (b).

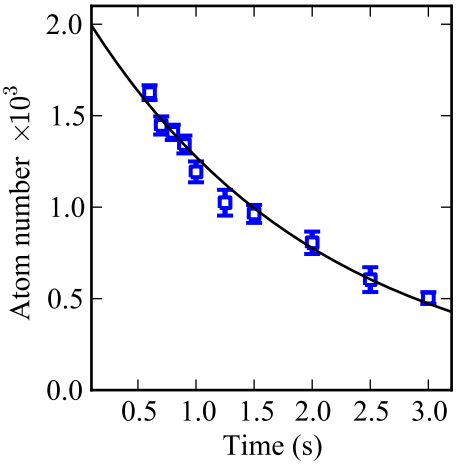

Figure 3.20: Atom number in the dipole trap as a function of the hold time. The atom number is found by collecting fluorescence produced when the atoms are illuminated using the MOT beams set to resonance. The $1/e$ lifetime is 2.0 ± 0.1 s.

indicated by the intercept of the green lines. The data are sliced along the green lines and fit with Gaussian functions as shown in Fig. 3.19 (b).

3.5.3 Dipole trap lifetime

The dipole trap is characterised by performing a lifetime measurement; the number of atoms remaining in the trap after various trapping periods is recorded. The hold time period labelled ⓒ in Fig. 3.18 is varied before recording a fluorescence image of the trap. The number of atoms in the trap is found using Eq. (3.8) and the results are shown plotted as a function of hold time in Fig. 3.20. In order to find the lifetime of atoms in the dipole trap the data are fit with an exponential function giving a $1/e$ lifetime of 2.0 ± 0.1 s. The lifetime of the trap is likely to be limited by collisions with background gasses; Ref. [87] indicates that for a $1/e$ lifetime of the order of a second the pressure in the experimental apparatus would have to be approximately $2{\times}10^{-9}$ Torr, which would appear to agree with the lifetime measured here.

3.6 Summary and conclusion

This chapter covers the details of the experimental apparatus and methods that build the foundation of the work presented in the remainder of this thesis. Firstly, the design of the vacuum chamber is presented and its key featured discussed. In section 3.3 the setup of the MOT is presented along with its characterisation and optimisation. The time of flight measurement indicates that after a molasses of 7 ms a temperature of 20 μK is reached. Absorptions measurements were also made in order to determine the atom number and calibrate the quantisation magnetic field. These measurements indicate an approximate atom number of 6 million and the magnetic field is related to the shim coil current by : B (G)$= (0.29 \pm 0.02) \times I$ (A) .

In the final section, 3.5, the setup of the dipole trap is detailed. Once cooled by the MOT and molasses atoms are loaded into the dipole trap. The trap is produced using 852 nm light with a power of 350 mW focused to a beam waist of 15 μm. Approximately 2×10^3 atoms were found to be loaded into the dipole trap; although this is a small fraction of the 6×10^6 atoms available in the MOT, it is to be expected using loading technique used. With a dipole trap beam waist of $\sim$ 15 μm and a MOT cloud radius of $\sim$ 250 μm, the overlap region is small and by simply taking a ratio of these volumes one would expect a dipole trap atom number in the order of 10^3. Images of the dipole trap are presented along with a lifetime measurement indicating that the atoms have a $1/e$ lifetime of 2.0 ± 0.1 s, which is likely limited by collisions with background gasses. Although the dipole trap presented here has modest atom number and lifetime, these are not critical requirements of the experiments detailed later in this thesis. The atom number is adequate to provide sufficient signal to noise when taking fluorescence measurements and atoms are not required to be held in the trap for time periods of more than a few tens of microseconds. The use of higher trapping light intensity and larger beams sizes, along with more elaborate loading techniques, allows larger atom numbers and lifetimes to be achieved. Ref. [87] indicates that lifetimes of dipole traps, when loaded from a MOT generated from a background vapour, are limited to around one second. If longer trap lifetimes are required, loading under improved vacuum conditions is required and can be achieved using

techniques such as a double MOT setup [90]. Using such a setup a lifetime of ~ 10 s can readily be achieved [75]. Where atom number is important, in order to create a large BEC for example, atom numbers of around 10^6 can be achieved [91].

Chapter 4

Ground state Raman transfer

This Chapter covers the generation of light comprising two frequency components, which differ by the ground state hyperfine splitting, and its application to drive ground state Raman transfer. Many experiments require the use of Raman light: in particular the scheme proposed by Müller et al. [20], introduced in Chapter 2, enables a C-NOT gate operation consisting of Raman transfer controlled by coupling to a Rydberg state. Attempting to realise this scheme motivates the work presented in this chapter.

In order to produce the necessary Raman beams an electro-optic modulation (EOM) technique is employed. To spatially filter the Raman beams a novel technique employing the Faraday effect in an isotopically pure thermal vapour cell [92] has been developed and is discussed in Sec. 4.1.2. The application of the Raman beams to drive ground state transfer in a sample of ultracold atoms released from the dipole trap is covered in Sec. 4.2. A detailed description of the experimental setup is given along with the parameters required to block the transfer by coupling to a Ryderg state. Finally, the results are presented accompanied by a discussion of the future direction of the experiment.

4.1 Raman light generation

4.1.1 Motivation

Many atomic physics experiments employ phase coherent laser light at frequencies separated by the ground state hyperfine splitting, examples include: stimulated Raman transitions [93]; coherent population trapping [10]; and Λ-system or $\mathcal{N}$-system electromagnetically induced transparency (EIT) [60, 72]. Alternatively, Raman light is also produced in experiments involving Raman scattering processes [94]. In many cases the two components of the Raman light are of unequal intensity and are not spatially separated.

Of particular interest here is the application of Raman light to form a mesoscopic Rydberg gate as suggested by Müller *et al.* [20] and introduced in Chapter 2. A fundamental step towards achieving this scheme experimentally is the blocking of ground state Raman transfer in an ensemble of atoms by the addition of a Rydberg state coupling. Such stimulated Raman transitions have been studied theoretically by Freegarde *et al.* [95]. This therefore motivates the production of phase stable Raman light separated by the ground state hyperfine splitting and demonstration of Raman transfer presented in this chapter.

Previously, several different techniques have been used to generate Raman light. These include: injection locking of two diode lasers using the +1 and -1 diffracted orders of light passed through a high frequency acousto-optic modulator (AOM) [96]; injection locking of two diode lasers to the sidebands produced by current modulation of the master laser [97]; or injection locking of a diode laser using the carrier and sidebands produced by an electro-optic modulator (EOM) [72]. A drawback of the EOM technique is that the different frequencies of light produced are of unequal intensities and are not spatially separated. The output beam of the EOM is dominated by the carrier frequency and does not have the necessary spectral purity required to inject a slave laser at the sideband frequency. The frequency components may be separated by various techniques [98, 99]; in the present work a Faraday filter is employed as described in the following section.

4.1.2 Faraday filtering

A narrow band atomic filter can be realised using the Faraday effect where a longitudinal magnetic field induces a circular birefringence in the medium [100]. Atomic filters exploiting birefringence were introduced by Öhman [101]. This principle was developed into the Faraday anomalous-dispersion optical filter (FADOF), which has been demonstrated in Cs [102], Rb [103–105] and Na [106]. Similarly, the induced-dichroism excited atomic line (IDEAL) filter, which operates without a magnetic field, has been demonstrated in K [107]. More recently, atomic filters have been produced using absorption in a thermal vapour cell [94] and velocity selective optical pumping in an atomic vapour [108]. Narrow band atomic filters have applications in free space laser communications [104], atmospheric measurements using LIDAR [106, 109], ocean temperature profiling using LIDAR [105] and the generation of narrow band quantum-noise-limited light [102]. In order to generate the Raman beams required for the experiment presented in this thesis a technique using an isotopically pure vapour cell is used such that the Faraday effect in ^{85}Rb is exploited to filter Raman light resonant with ^{87}Rb [92].

The Faraday effect is observed when a magnetic field is applied parallel to the direction of light propagation, for initially linearly polarised light the plane of polarisation is rotated by an angle, θ, given by:

$$\theta = \mathcal{V}BL, \tag{4.1}$$

where $\mathcal{V}$ is the Verdet constant, B the magnitude of the applied magnetic field and L the length of the medium. The Verdet constant is dependent on the properties of the medium, the wavelength of the light and the temperature. Typical commercial Faraday isolators employ a Terbium Gallium garnet crystal with a Verdet constant of 134 Rad T^{-1} m^{-1} at 632 nm [110].

The polarisation plane rotation is produced by an induced circular birefringence in the medium [111] which produces a relative phase shift, $\Delta\phi$, between circular field components given by:

$$\Delta\phi = \frac{\omega L}{c}(n^+ - n^-), \tag{4.2}$$

where n^+ and n^- are the refractive indices of the circular components driving σ^+ and σ^- transitions, respectively. The relative phase shift has a spectral dependance which can be expressed as:

$$\frac{\mathrm{d}(\Delta\phi)}{\mathrm{d}\omega} = \frac{L}{c}(n_g^+ - n_g^-), \tag{4.3}$$

where n_g^+ and n_g^- are the relative group refractive indices. The relative phase shift causes a rotation in the plane of polarisation of initially linearly polarised light by an amount $\theta = \Delta\phi/2$ (see Methods section in Ref. [111]).

By exploiting the Faraday effect in an isotopically pure Rb thermal vapour it is possible to design a system with a frequency dependent polarisation rotation. Light that is resonant with the lower ground state hyperfine to excited state transition in one isotope, but is in the absorption wings of the filter isotope, will be transmitted unchanged. On the other hand, light resonant with the upper hyperfine to excited state transition experiences a rotation in polarisation equal to $\pi/2$, and therefore can be separated using a polarising beam splitting (PBS) cube, thus realising a narrow band atomic filter for Raman light. This technique allows frequencies several GHz apart to be separated; methods that employ dichroic mirrors for example, are only effective for light separated by several nanometres.

4.1.3 Experimental Setup and Faraday filter operation

A schematic experimental setup of the Faraday filter is shown in Fig. 4.1 (a). Light from a master 780 nm diode laser is frequency stabilised to the ^{87}Rb $5S_{1/2}(F = 2) \rightarrow 5P_{3/2}(F' = 3)$ transition using modulation transfer spectroscopy [112]. Light from this laser is passed through an EOM[1] driven by a signal generator[2] modulated at $\nu_m = 6.8$ GHz [corresponding to the ground state hyperfine-splitting in ^{87}Rb as shown in Figure 4.1 (b)]. The EOM generates sidebands at $\pm\nu_m$ with an amplitude of 1%. The beam is then linearly

[1] New Focus 4851

[2] Aglient E8267D

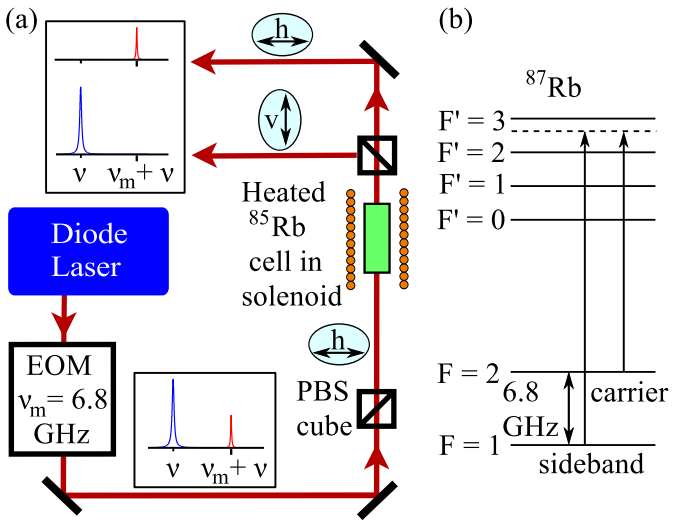

Figure 4.1: (a) Schematic experimental setup of the Faraday filter. An EOM is used to create sidebands at $\nu \pm \nu_m$ with $\nu_m = 6.8$ GHz producing light corresponding to the Raman transitions in ^{87}Rb as shown in (b). The components at ν and $\nu + \nu_m$ are separated using the Faraday effect in a heated ^{85}Rb vapour cell within a solenoid. The input light is initially horizontally polarised using a polarising beam splitting (PBS) cube. Following the solenoid the different frequency components are separated using a second PBS cube. The insets show schematics of Fabry-Pérot etalon signals.

polarised by a PBS cube and propagated through a heated isotoptically pure ^{85}Rb vapour cell[3] within a solenoid 28 cm in length with a field uniformity better than 1% over the length of cell. The Rb vapour cell contains a mixture of Rb isotopes in a ratio of ^{85}Rb : ^{87}Rb equal to 99.9 : 0.1. The current in the solenoid produces both a homogenous magnetic field along the length of the cell and Ohmic heating. Following the vapour cell the light is analysed using a second PBS cube, which generates the two output ports of the filter.

The Faraday beamsplitter output as a function of the laser frequency is shown in Fig. 4.2. The solid red vertical line indicates the position of light at the carrier frequency and the dashed red line shows the sideband frequency, $\nu + \nu_m$. Experimental data are represented by a blue line and the black line is a theoretical calculation, which is seen to be in good agreement. The calculation is based on the theoretical model presented in [113] and the polarisation

[3]Triad Technology TT-Rb85-75-V-Q

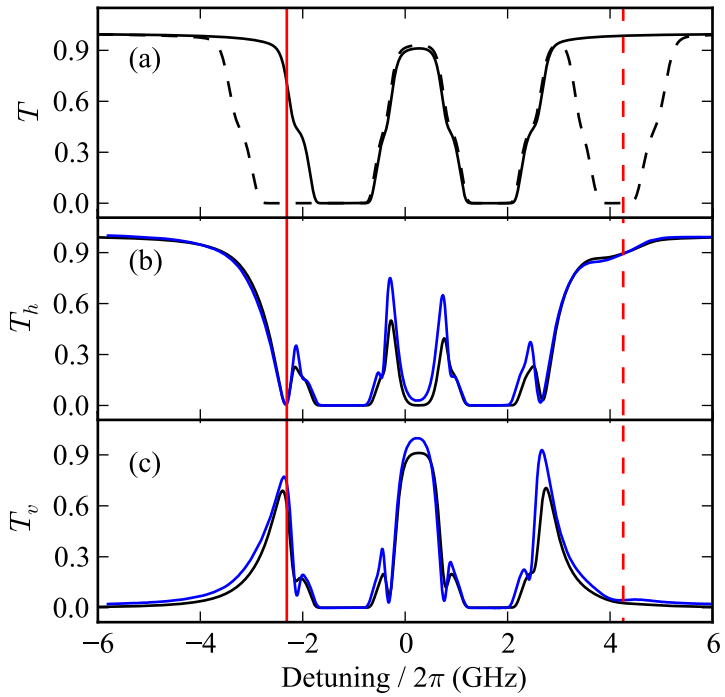

Figure 4.2: Transmission spectra at both output ports of the Faraday filter. Panel (a) shows the total transmission through the cell, $T_h + T_v$, for both pure ^{85}Rb (solid line) and Rb vapour with the natural isotope abundance (dashed line). Panel (b) corresponds to the transmitted port of the beamsplitter with panel (c) corresponding to the reflected port. The blue line represents the experimental data and the black line is the result of a theoretical calculation. The solid red vertical line shows the frequency of the carrier and the dashed red line the frequency of the sideband, $\nu + \nu_m$, generated by the EOM. Zero detuning corresponds to the weighted centre of the ^{85}Rb and ^{87}Rb D_2 lines.

rotation found using Eq. (4) from [111]. The magnetic field dependence is calculated using a full matrix diagonalisation as in [105]. Panel (a) shows the total transmission through the cell, $T_h + T_v$, for both pure ^{85}Rb (solid line) and Rb vapour with the natural isotope abundance (dashed line). It can be seen that without exploiting the detuning dependent rotation in polarisation the beamsplitter would transmit light at both the carrier ($T \sim 70\%$) and sideband frequency ($T \sim 100\%$) with no possibility of spatial separation. If the cell contained natural Rb vapour then light at the carrier frequency along with the sideband frequency would be absorbed ($T \sim 0\%$) as indicated by

the black dashed line.

Fig. 4.2 panels (b) and (c) demonstrate how by analysing the vapour cell output polarisation with the PBS cube the Raman light components can be spatially separated. Panel (b) shows the transmission of light with a horizontal polarisation, T_h, and panel (c) light with a vertical polarisation, T_v. At the carrier frequency, T_v is approximately 70% whereas T_h is close to zero. At the sideband frequency, $\nu + \nu_m$, the contrary is the case, with T_h being approximately 90% and T_v is less than 1%. This produces the desired separation of light at frequencies 6.8 GHz apart without a large portion of the light being absorbed by the vapour cell. The temperature of the splitter is approximately 70° C and the magnetic field is 80 G. The power of the beam before the splitter was approximately 25 μW with a waist of 1 mm. With these parameters the Verdet constant $\mathcal{V} = 2.6 \times 10^3$ rad T^{-1} m^{-1} at a detuning of 60 MHz.

In Fig. 4.3 the performance of the beamsplitter is demonstrated by using a Fabry-Pérot etalon with a free spectral range $\sim$ 745 MHz to analyse the light (a) with the magnetic field switched off, (b) at the transmitted port of the polariser (T_h) and (c) at the reflected port (T_v). The detuning axis is calibrated by using the known separation of the sidebands and carrier. In (a) the two components of the input beam are clearly visible with the signal dominated by the carrier. In (b) the carrier frequency is suppressed to approximately -18 dB, leaving the sideband unchanged. In (c) the sideband is suppressed to a level of -19 dB leaving only the carrier. The suppression of the carrier is limited by the extinction ratio of the polarisation optics. For the particular case where the Raman sideband is produced by an EOM the other sideband is also present. The unwanted sideband is removed by injecting a slave laser. In contrast to Ref. [72] where a double injection scheme is required to achieve a spectrally pure Raman beam, the Faraday filter enables a stable operation at the sideband frequency with a single injection stage.

The characterisation of the Faraday filter presented in Fig. 4.2 is made with a moderately low beam power of 24 μW (with a beam waist of 1 mm). For the filter to be practical it must maintain its transmission profile at the Raman beam frequencies for much higher laser powers. This then allows higher power beams to be filtered which can subsequently be used to provide light for a

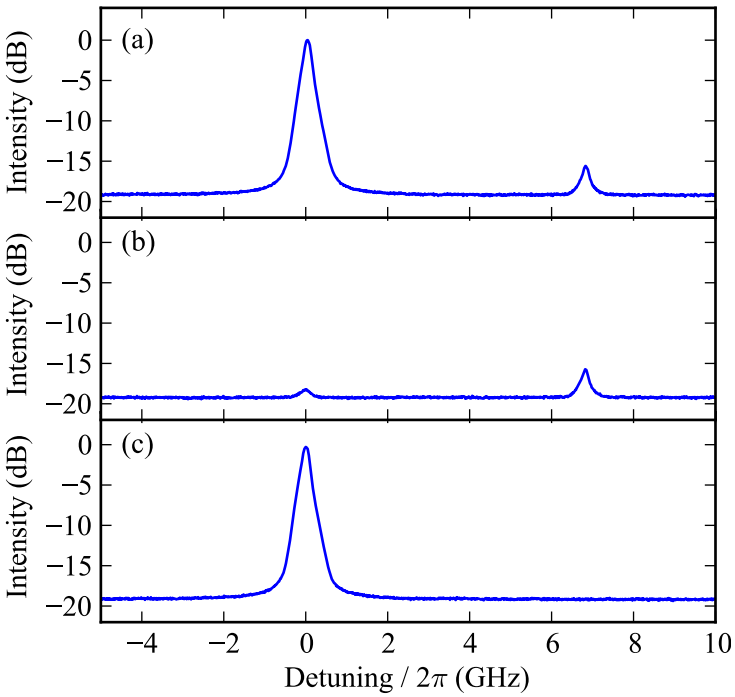

Figure 4.3: Fabry-Pérot etalon signals. In (a) the beamsplitter is turned off, (b) is at the transmitted port of the polariser (T_h) and (c) is at the reflected port (T_h). In (a) both carrier and sideband are present, in (b) the carrier is suppressed to approximately -18 dB and in (c) the sideband is suppressed to the noise level leaving only the carrier.

magneto-optic trap (MOT) and Raman beams, as in this work, or other such applications. The transmission characteristics of the filter at varying beam powers are presented in Fig. 4.4. At these intensities the beam is far above the weak probe limit and optical pumping effects will dramatically alter the transmission properties of the medium [114]. Although the transmission of the filter is affected by the beam power, the properties at the key Raman beam frequencies remain largely unchanged. In practice the Faraday filter is operated at an input beam power of ∼10 mW so that sufficient light is available to inject the slave lasers lasers providing light for the MOT, Raman and EIT probe beams.

If at high power the performance of the filter is found to be reduced the laser intensity may be decreased by increasing the beam size. The size of the beam is in principle limited by the dimensions of the Rb vapour cell

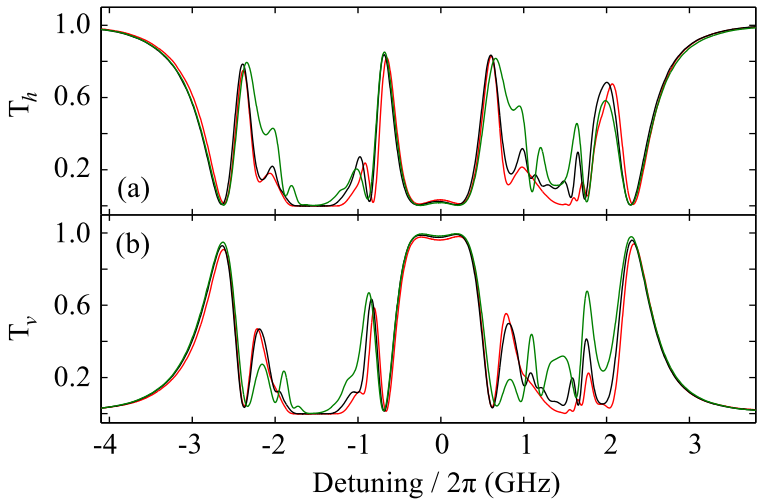

Figure 4.4: Transmission spectra at both output ports of the Faraday beamsplitter for varying beam powers. Panel (a) corresponds to the transmitted port of the beamsplitter with panel (b) corresponding to the reflected port. The beam powers are: red 2.56 mW; black 5.12 mW; green 10.2 mW.

used; in the present experiment the cell is approximately 25 mm in diameter. This highlights a distinct advantage over commercial Faraday isolators where the beam size is limited by the size of the crystal, typically only several millimetres in diameter.

4.2 Raman transfer

4.2.1 Experimental parameters

With the Raman light generated using the method described it is possible to study a system similar to that proposed by Müller *et al.* [20]. One of the fundamental elements of this scheme is the blocking of population transfer between two qubit states by coupling to a Rydberg state. This is shown diagrammatically in Fig. 4.5 (a) where Raman transfer takes place between qubit states $|1\rangle$ and $|2\rangle$ and may be blocked by a coupling of the intermediate state, $|3\rangle$, to a Rydberg state, $|\mathrm{R}\rangle$. The Raman transfer is driven by beams with on-resonance Rabi frequency Ω_p that are detuned by Δ from resonance.

The Raman transfer is blocked by an EIT-type interference process so that

the intermediate $|3\rangle$ state is eliminated. Müller *et al.* report that the Raman transfer may be blocked with a 99% fidelity when the Rabi frequencies meet the condition that $\Omega_c > 2\Omega_p$. The experimental parameters must therefore be carefully chosen such that the Rabi frequencies will meet this condition. The value of Ω_c is limited by the laser power available at the frequency required to couple to the Rydberg state. In the case of the experiment presented in this thesis Ω_c is limited to a value in the order of 10 MHz, the exact value depending on the specific Rydberg state and the beam focus size.

It is clear that meeting the condition that $\Omega_c > 2\Omega_p$ may also be achieved by reducing the value of Ω_p. This will, however, affect the time scale over which Raman transfer between states $|1\rangle$ and $|2\rangle$ occurs. The entire population will be Raman transferred by a π-pulse with a duration given by:

$$t_\pi = \frac{2\pi\Delta}{\Omega_p^2}. \tag{4.4}$$

The π-pulse time should be minimised to prevent decoherence effects reducing the fidelity of the Raman transfer. Hence, the parameters Δ and Ω_p must be chosen such that t_π is of appropriate duration but the $\Omega_c > 2\Omega_p$ condition required to block the transfer is still met.

As suggested by Müller *et al.* the hyperfine ground states and Rydberg states of ^{87}Rb offer a suitable system to demonstrate the proposed scheme. The

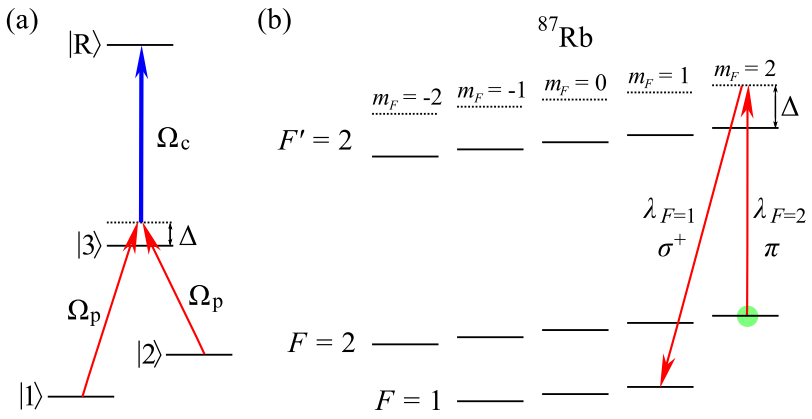

Figure 4.5: (a) Shows the Raman transfer scheme between states $|1\rangle$ and $|2\rangle$, and coupling to a Rydberg state $|R\rangle$. The specific Raman transfer energy levels for ^{87}Rb are shown in (b).

specific Raman transfer process chosen is shown by the detailed energy level diagram of Fig. 4.5 (b); population in the 5s $^2\mathrm{S}_{1/2}(F = 2)$ ground state is coherently transferred to the 5s $^2\mathrm{S}_{1/2}(F = 1)$ state via the intermediate 5p $^2\mathrm{P}_{3/2}(F' = 2)$ state. If the atoms are prepared initially in the $|F = 2, m_F = 2\rangle$ state they may be Raman transferred to the $|F = 1, m_F = 1\rangle$ state via the $|F' = 2, m_F = 2\rangle$ state using a π and σ^+ polarised pair of beams. No Raman transfer is possible via the $F' = 3$ state because there is no transition from the $F = 1$ ground state, so this level is omitted from Fig. 4.5 (b). Other Raman transfer routes are possible via the $F' = 1$ state and are discussed later in Sec. 4.2.6.

The Rabi frequency of the Raman beams is found by [95, 113]:

$$\begin{aligned}\Omega &= (-1)^{2F'+J+i+m_F}\sqrt{\frac{2I}{c\hbar\epsilon_0}}\langle J||e\mathbf{r}||J'\rangle \\ &\quad\times\sqrt{(2F'+1)(2F+1)(2J+1)} \\ &\quad\times\begin{pmatrix} F' & 1 & F \\ m_{F'} & -q & -m_F \end{pmatrix}\begin{Bmatrix} J' & J' & 1 \\ F' & F & i \end{Bmatrix}. \end{aligned} \tag{4.5}$$

Here the braces and curly braces denote the Wigner-3j and Wigner-6j symbols respectively [115]. The variable I is the laser intensity and the reduced matrix element, $\langle J||e\mathbf{r}||J'\rangle$, is found from the upper state lifetime [116] and is tabulated in Ref. [82]. If the Raman beams in Fig. 4.5 (b) are both set to a waist size of 1 mm and have powers of 20 μW ($\lambda_{F=1}$) and 30 μW ($\lambda_{F=2}$), the Rabi frequency given by Eq. (4.5) is approximately 16 MHz for both beams. This corresponds to a π-pulse duration of 9 μs found using Eq. (4.4) if the detuning of the Raman beams is set to $2\pi\times60$ MHz. This set of approximate parameters therefore meets the requirements that the π-pulse duration is reasonably short with a Rabi frequency in the regime where the transfer may be blocked with the available coupling laser Rabi frequency.

4.2.2 Raman beams with thermal atoms

Before Raman transfer is studied in a sample of ultracold atoms the detuning of the Raman beams can be confirmed using spectroscopy in a thermal vapour cell. Fig. 4.6 (a) shows the optical setup used: a probe beam is propagated

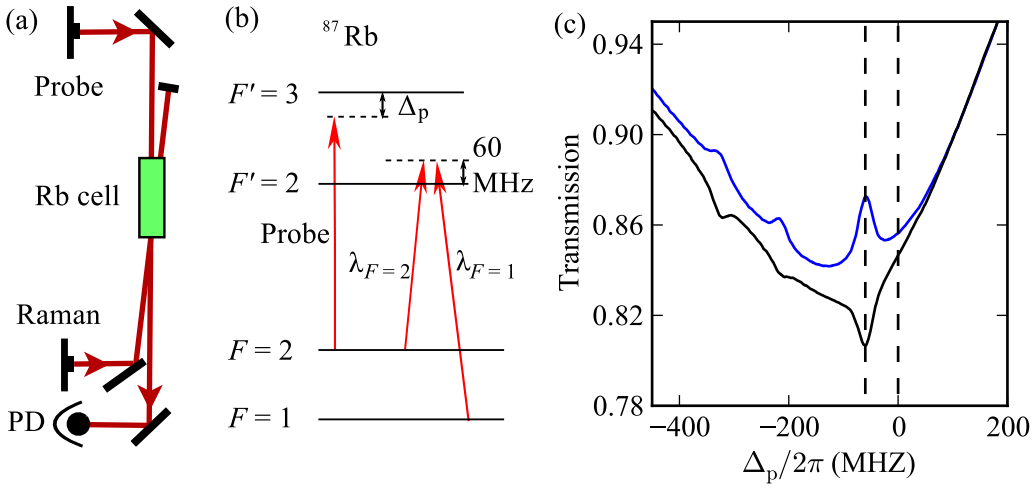

Figure 4.6: Raman beams with thermal atoms. (a) Experimental setup for spectroscopy using the Raman beams in a thermal vapour cell. A scanning probe beam is counter-propagated with either of the Raman beams and detected on a photodiode. (b) Relevant energy levels for ^{87}Rb showing the fixed Raman beams detuned from the $F' = 2$ state by 60 MHz and the scanning probe beam. (c) Transmission of the probe as a function of the detuning from the $F' = 3$ transition. The blue line corresponds to the combination of the probe and the $\lambda_{F=2}$ Raman beam; the black line is the result of the $\lambda_{F=1}$ Raman beam combined with the probe. The effect of the Raman beams is to produce a peak of increased and decreased absorption at a probe detuning of 60 MHz.

through a Rb vapour cell, with isotopes in their natural abundance, at room temperature. This beam is scanned through resonance with the 5s ^{2}S$_{1/2}(F = 2) \rightarrow$ 5p ^{2}P$_{3/2}(F')$ transitions and a spectrum recorded by detecting the probe at a photodiode. The Raman beams and probe beam are counter-propagated through the cell and the resulting spectra presented in Fig. 4.6 (c). The frequency axis is calibrated using standard saturated absorption spectroscopy [79] carried out by simply replacing the counter-propagating Raman beam with a pump beam of the same frequency as the probe. The vertical dotted lines show the position of the 5p ^{2}P$_{3/2}(F' = 3)$ absorption line at zero detuning and a frequency that is 60 MHz detuned.

The transmission of the probe is clearly modified by the presence of the Raman beams. Where the $\lambda_{F=1}$ Raman beam is combined with the probe,

shown by the black line in Fig. 4.6 (c), an enhancement in absorption is produced at the hyperfine and cross-over resonances. For the combination of probe and $\lambda_{F=2}$ Raman beam, shown by the blue line, the converse is true; a decrease in absorption is created. This occurs because the $\lambda_{F=1}$ Raman beam will pump population into the $F = 2$ state, increasing the absorption of the probe when it is on resonance. The $\lambda_{F=2}$ Raman beam will have the same effect as the pump beam in saturation absorption spectroscopy: it will pump population away from the $F = 2$ state and reduce the amount by which the probe is absorbed.

The positions of the features can be understood by considering the energy level diagram in Fig. 4.6 (b). Although the Raman beams are fixed at a detuning of 60 MHz above the 5p $^2\mathrm{P}_{3/2}(F' = 2)$ state they will be Doppler shifted into resonance by the selection of the appropriate velocity class of atoms. As the probe beam is scanning it will become resonant with different velocity classes at different frequencies. When it is detuned by 60 MHz it will select the same velocity class as the Raman beams and be on resonance with the 5s $^2\mathrm{S}_{1/2}(F = 2) \rightarrow$ 5p $^2\mathrm{P}_{3/2}(F')$ transitions giving the sub-Doppler features familiar from saturated absorption spectroscopy. The features appear at detunings 60 MHz below resonance because of the counter-propagating probe and Raman beams. As the beams will have wavevectors of opposite sign, for the Doppler shifts to be equal for the same velocity class the detuning must also be of the opposite sign.

The Rabi frequencies of the Raman beams were set to be approximately equal by adjusting the power so that the features observed in Fig. 4.6 (b) were equal in size. In this case the pumping effect of each beam is matched. Once the frequency of the Raman beams was confirmed using the spectroscopy of thermal atoms the beams could be employed to carry out Raman transfer of ultracold atoms released from the dipole trap as discussed in the next section.

4.2.3 Raman transfer in an ultracold ensemble

The experimental setup for Raman transfer in ultracold atoms released from the dipole trap is shown in Fig. 4.7. The setup and characterisation of the dipole trap is covered in detail in Chapter 3. The $\lambda_{F=1}$ Raman and optical

pumping beams are both counter-propagated along the path of the dipole trap beam. A quantisation magnetic field is created along this axis by using one pair of the shim coils, thus ensuring the beams have a circular polarisation. The optical pumping and Raman beam are combined using a 50:50 beam splitter and the polarisation set to be circular using a $\lambda/4$ waveplate.

For the $\lambda_{F=2}$ Raman beam to have the necessary linear polarisation it must propagate in a direction perpendicular to the quantisation magnetic field. The beam is in a direction pointing 45 degrees out of the plane of the page in Fig. 4.7. With this setup the beam is of linear polarisation in a plane set by the $\lambda/2$ waveplate. The beams were aligned by observing them deplete the number of atoms in the MOT whilst it was loading continuously. The waists of the $\lambda_{F=1}$ and $\lambda_{F=2}$ Raman beams are 1.1 mm and 0.8 mm respectively; the beams are not focused so that the power does not vary by large amounts over the size of the dipole trap. This ensures that all atoms experience the same Rabi frequency regardless of their position in the dipole trap and Rabi oscillations at only a single frequency are observed.

The experimental sequence for Raman transfer measurements is shown in Fig. 4.8. The loading of the MOT and dipole trap is covered in more detail

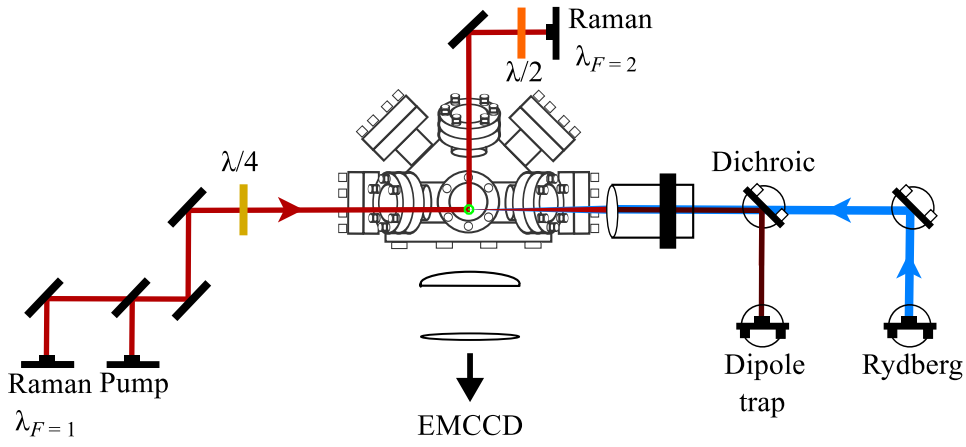

Figure 4.7: Experimental setup for ground state Raman transfer of atoms released from the dipole trap. The circularly polarised $\lambda_{F=1}$ Raman beam and optical pumping beam propagate through the position of the dipole trap. Light for the dipole trap is focused at the centre of the MOT along the same axis. The $\lambda_{F=2}$ Raman beam is in a plane perpendicular to this axis and is linearly polarised. Fluorescence imaging is carried out using an EMCCD camera and lens system.

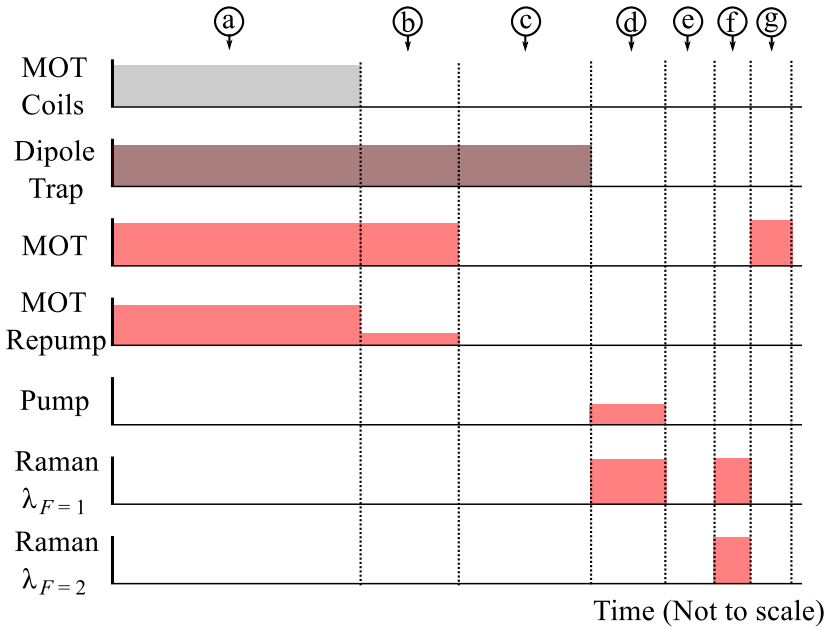

Figure 4.8: Experimental sequence for Raman transfer in cold atoms. Initially atoms are loaded into the dipole trap as described in Chapter 3. Optical pumping prepares the atoms into the $|F = 2, m_F = 2\rangle$ state. The Raman beams are then switched on to transfer atoms between ground states before the population in the $F = 2$ state is measured using fluorescence imaging.

in Chapter 3. In ⓐ the MOT is loaded for a time of 5 s after which a 5 ms molasses, ⓑ, cools the atoms further. During this time the dipole trap light is on and atoms can be loaded into the optical potential. Any atoms remaining trapped only by the MOT are allowed to fall away under gravity during a 25 ms period, labelled ⓒ, when the MOT is switched off. In order to prepare the atoms in the correct initial state a 0.1 ms period, ⓓ, of optical pumping is used followed by a period of 5 ms allowing for the mechanical shutters used to block the beams to switch, labelled ⓔ. These shutters are used in addition to the optical switching provided by the accousto-optic modulators (AOMs) to ensure no leakage light is present during the experiment. The Raman beams can now be applied to the sample in part ⓕ for various times to create Rabi oscillations between the hyperfine ground states. Finally, in ⓖ, the cloud of atoms is imaged to measure the number of atoms in the $F = 2$ state. This is done by illuminating the cloud using the MOT beams for 0.3 ms, with no repump light and the cooling light on resonance, and

detecting fluorescence using an EMCCD camera[4].

To measure the number of atoms transferred by the Raman beams the fluorescence images must be calibrated. Although this can be done in such a way as to measure the absolute number of atoms, a more useful figure of merit is the number of atoms in the $F = 2$ state as a proportion of the total number in the system. The experimental sequence in Fig. 4.8 is therefore repeated a second time but without the Raman beams being switched on. This gives a measurement of the total number of atoms available for transfer and can be compared to the result of the sequence where the Raman beams were on. The proportion of atoms transferred is therefore found by:

$$\mathscr{N} = \frac{N_{F=2}}{N_{\mathrm{TOT}}} = \frac{\mathrm{S_{Raman}} - \mathrm{S_{Bg}}}{\mathrm{S_{NoRaman}} - \mathrm{S_{Bg}}}, \tag{4.6}$$

where S_{Raman} is the pixel sum of an image taken after the sequence with the Raman beams on, S_{NoRaman} is the result of the sequence without the Raman beams and S_{Bg} is the pixel sum of a background image. The background level of light is found by repeating the sequence with the MOT coils switched off so that no atoms are loaded into the trap. This is found to be reasonably constant so is not repeated for every run of the experiment but taken from the average of 20 shots.

4.2.4 Optical pumping

For the Raman transfer process to produce Rabi oscillations at a single frequency and with good visibility the sample of atoms must be prepared in the same initial state. Atoms are therefore prepared in the $|F = 2, m_F = 2\rangle$ state using the optical pumping scheme shown in Fig. 4.9 (a). An optical pumping beam, λ_{OP}, is resonant with the 5s $^2\mathrm{S}_{1/2}(F = 2) \rightarrow$ 5p $^2\mathrm{P}_{3/2}(F' = 2)$ transition and is circularly polarised so that it drives σ^+ transitions. This will have the effect of driving population towards states with $m_F > 0$. As the $F' = 2$ state can decay to both the $F = 1$ and $F = 2$ ground states a repump beam, λ_{RP}, is also required to ensure the lower ground state is not populated. This is detuned 10 MHz from the 5s $^2\mathrm{S}_{1/2}(F = 1) \rightarrow$ 5p $^2\mathrm{P}_{3/2}(F' = 2)$

[4]Andor iXon 885 with the imaging system described in Chapter 3

transition to avoid any two-photon Raman resonances. Once population has been pumped to the $|F = 2, m_F = 2\rangle$ state it will be dark to both λ_{OP} and λ_{RP} so will remain in this state whilst the pumping light is on without any unwanted heating effects.

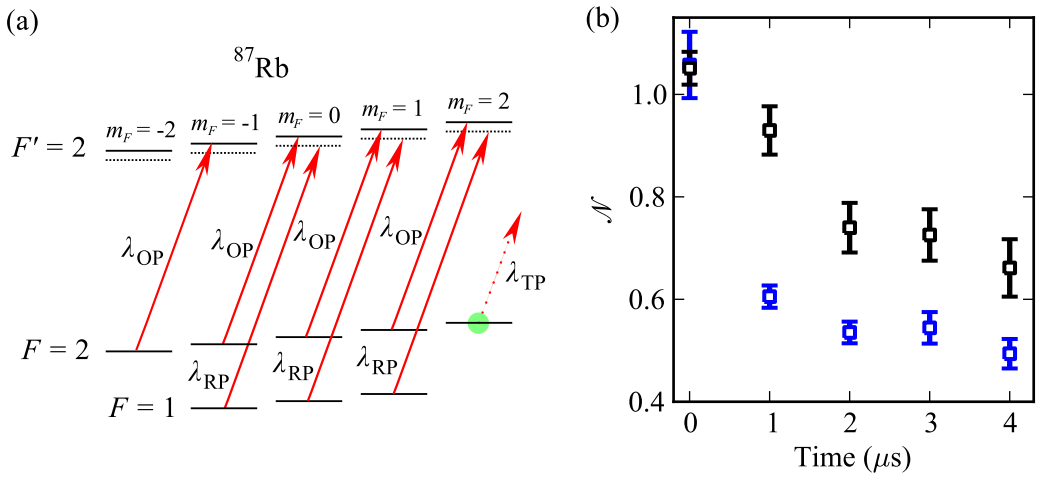

Figure 4.9: (a) Relevant energy levels in ^{87}Rb for optical pumping. The optical pumping beam, λ_{OP}, and Repump beam, λ_{RP}, are both σ^+ polarised to drive the atoms into the $|F = 2, m_F = 2\rangle$ state. This state is then dark to the optical pumping light and repump light. The effectiveness of the optical pumping is demonstrated in (b). A test pump pulse, λ_{TP}, is applied for various times to remove population from the $F = 2$ state. The blue data show the results of applying λ_{TP} without optical pumping; the black data show the result after the optical pumping has been applied.

In order to test the effectiveness of the optical pumping a system of determining how the population is distributed across the m_F states is required. Collecting fluorescence light from imaging with the MOT beams only gives information about the number of atoms in the $F = 2$ state; it is insensitive to the magnetic sub-levels unless they can be shifted in energy with a large magnetic field. An alternative method is to make use of the fact that the atoms prepared into the $|F = 2, m_F = 2\rangle$ state will not absorb the optical pumping light. If after the optical pumping phase the light is applied again to the sample, this time as a 'test pump', λ_{TP}, there should be no effect. If population is observed to be lost from the $F = 2$ state the atoms were not in a dark state and not correctly prepared into the required initial state.

The results of applying the test pump pulse to the sample for varying times is shown is Fig. 4.9 (b). The black and blue data show the proportion of atoms remaining in the $F = 2$ state with and without the preceding optical pump respectively. The data represent the average of 10 measurements and the error bars are the standard error. Where the atoms are randomly distributed throughout the m_F states, the application of λ_{TP} would cause population to be lost to the $F = 1$ state; the value of $\mathscr{N}$ would fall for longer pumping times. This is clearly seen in the blue data of Fig. 4.9 (b). However, if the sample were to contain only atoms prepared in the $|F = 2, m_F = 2\rangle$ then no pumping caused by λ_{TP} would occur; the value of $\mathscr{N}$ would remain constant.

The data in Fig. 4.9 (b) show that the optical pumping does increase the population in the $|F = 2, m_F = 2\rangle$ state, but not to a level where further pumping by λ_{TP} is eliminated. The data would suggest that around 60% of the atoms were pumped into the dark state, indicated by the limit of the exponential decrease of $\mathscr{N}$ as the test pump period is increased. The effectiveness of the optical pumping could be limited by the polarisation of the optical pumping light not being purely circular. Any light present with a different polarisation would interact with atoms in the $|F = 2, m_F = 2\rangle$ state, making it no longer a dark state. Incorrect polarisation could result from the quality of the optics used or alignment with the magnetic field quantisation axis. Although the optical pumping is not crucial for the success of the experiment, where showing that Rabi oscillations can be suppressed by coupling to a Rydberg state is the goal, problems at this stage may also appear during following Raman transfer phase. With the optical pumping not behaving as expected, the Raman transfer could suffer from the same deficiencies in the experiment.

4.2.5 Raman transfer results

Raman transfer can be carried out once the atoms are prepared into the initial $|F = 2, m_F = 2\rangle$ state, to the greatest extent achievable with the optical pumping described in the previous section. The effects of the Raman beams can be observed in two ways: one of the beams can be scanned in frequency whist the other remains fixed to detect the two-photon resonance; secondly

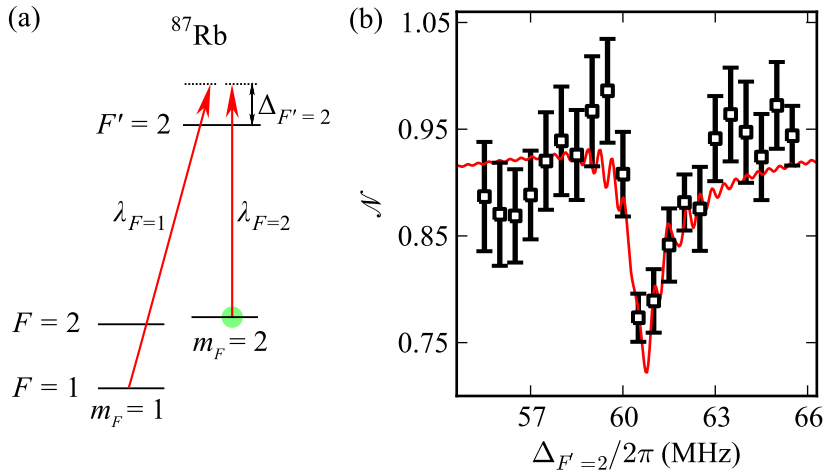

Figure 4.10: (a) Relevant energy levels for two-photon Raman resonance measurement. The Raman beams $\lambda_{F=1}$ and $\lambda_{F=2}$ are σ^+ and π polarised respectively. Atoms initialised into the $|F = 2, m_F = 2\rangle$ state will be coherently transferred to the $|F = 1, m_F = 1\rangle$ state. (b) Proportion of atoms remaining in the $F = 2$ state after Raman pulses with a duration of 1.5 μs as a function of the detuning of $\lambda_{F=2}$ from resonance.

the frequency of the beams can be fixed but the pulse length varied to produce Rabi oscillations. In both cases the length and frequency of the pulses must be controlled accurately and varied with a high resolution. The beams are pulsed on by switching the rf signal sent to the AOMs used to control their frequency. In order to achieve a short pulse time the AOM driver is switched using a TTL pulse from a function generator[5] with a bandwidth of 25 MHz. The pulse length of the Raman beams is then limited to approximately 50 ns by the rise and fall time of the AOM.

To scan the frequency of the Raman beams requires that the rf signal provided to the AOM be varied in frequency. Typically the rf signal is produced by an AOM driver controlled using LabVIEW allowing the frequency to be set with a resolution of approximately 0.25 MHz. For a two-photon Raman resonance with a width of the order of a few MHz a higher resolution frequency scan is required. This is achieved again by making use of a function generator[6] with a frequency resolution of 1 mHz to drive the AOM.

[5]Tektronix AFG 3022B
[6]Tektronix AFG 3252

The resulting measurement of a two-photon Raman resonance is shown in Fig. 4.10. The relevant energy levels are shown in part (a); one of the Raman beams ($\lambda_{F=1}$) is held at a fixed frequency whilst the other beam ($\lambda_{F=2}$) is varied. The number of atoms remaining in the $F = 2$ state is shown in Fig. 4.10 (b) as a function of the $\lambda_{F=1}$ beam frequency. The data represent the average of 10 measurements and the error bar is the standard error. The frequency axis is scaled so that zero corresponds to the beam being on resonance with the 5s $^2S_{1/2}(F = 2) \rightarrow$ 5p $^2P_{3/2}(F' = 2)$ transition. With $\lambda_{F=1}$ detuned by a fixed 60 MHz above this transition the two-photon Raman resonance is manifest as a fall in the value of $\mathscr{N}$ at a frequency of 60 MHz. The beams are set to high powers of 460 μW ($\lambda_{F=1}$) and 380 μW ($\lambda_{F=2}$) so that the Raman transfer is less sensitive to other experimental parameters. The Raman beams are pulsed on for a time of $\tau_R = 2$ μs, which in the case of the high beam powers used corresponds to many π-pulses.

The data in Fig. 4.10 (b) clearly show a two photon Raman resonance at a frequency of 60 MHz. The population in the $F = 2$ state is observed to fall by 20% when the two-photon resonance is met. The red line in Fig. 4.10 (b) is the result of a theoretical calculation of the Raman transfer [117]; the Lindblad master equation [118] is solved for the system of two Raman beams

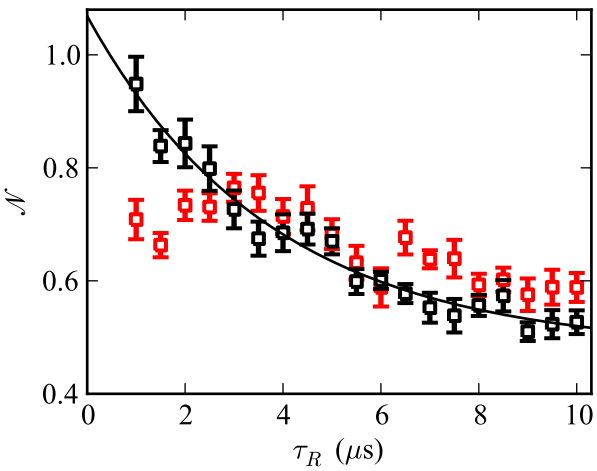

Figure 4.11: Proportion of population remaining in the $F = 2$ state after Raman pulses of duration τ_R. The black data show the case where only the $\lambda_{F=2}$ Raman beam is on; the red data show the results of both Raman beams being on simultaneously. The solid black line is an exponential fit to guide the eye.

and the energy levels shown in Fig. 4.5 (b). Where the initial population is distributed throughout the $|F = 2, m_F\rangle$ states the theoretical model gives a good qualitative description of the data.

The proportion of population remaining in the $F = 2$ state as a function of the Raman pulse duration, τ_{R}, is shown in Fig. 4.11. The data represent the average of 10 measurements and the error bar is the standard error. The black data show the change in $\mathscr{N}$ when only the $\lambda_{F=2}$ Raman beam is on and the solid black line is an exponential fit to guide the eye. In this case the $F = 2$ population is observed to fall because of incoherent pumping, which is significant even with $\lambda_{F=2}$ detuned from resonance by 60 MHz. With both Raman beams on simultaneously, the case of the red data in Fig. 4.11, the value of $\mathscr{N}$ is observed to deviate from the incoherent pumping case. This can be attributed to a two-photon Raman transfer between the two ground states. Although the Rabi oscillations have a low visibility, the value of $\mathscr{N}$ does vary above and below the coherent pumping case. The largest Raman transfer, approximately 25%, is observed for a time period of $\tau_{\mathrm{R}} = 1.5$ μs, which agrees well with the data in Fig. 4.10 (b).

4.2.6 Discussion

The results of applying the Raman beams to a sample of ultracold atoms shows some evidence of coherent transfer, indicated by the recovery of $F = 2$ population after an initial dip. This coherent transfer between the ground states was, however, only observed to have a fidelity of 20%. No clear Rabi oscillations were observed with the setup up described in this chapter. The key factors contributing to this are likely to be the small detuning of the Raman beams from resonance with the intermediate state and the poor performance of the optical pumping.

The detuning from resonance was chosen, as discussed at the beginning of this section, so that the suppression of the Raman transfer by coupling to a Rydberg state was feasible. This constraint is imposed by the laser power available at 480 nm and the lack of short focal length optics inside the vacuum chamber to focus the beam. Similar work on Raman transfer combined with Rydberg states has demonstrated high fidelity Raman oscillations: the

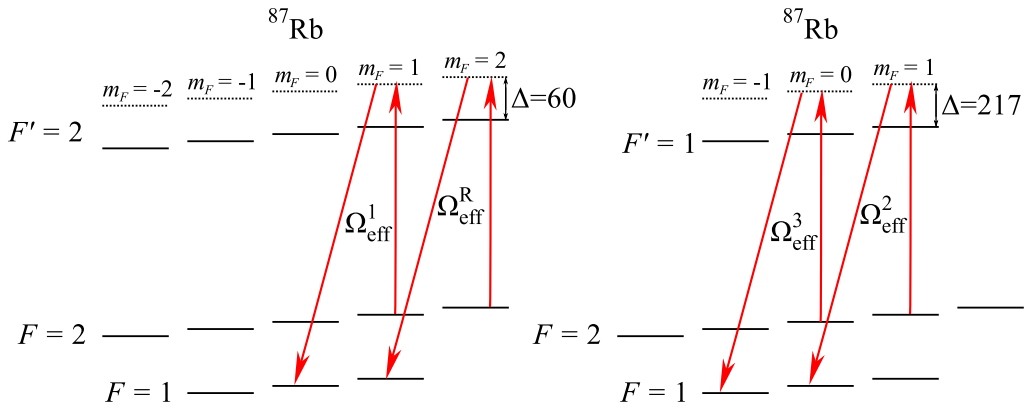

Figure 4.12: Possible Raman transfer Rabi frequencies for atoms that are not optically pumped into the $|F = 2, m_F = 2\rangle$ state.

neutral atom C-NOT gate demonstrated by the Saffman group [48] employs Raman beams that are detuned $2\pi \times 41$ GHz from resonance [49]. However, in this scheme the transfer of population between ground states is blocked by exciting the target atom to Rydberg states; if the target atom is excited to a Rydberg state Raman transfer will not occur. This Rydberg excitation is dependent on the state of a nearby control atom via the dipole blockade mechanism. In this scheme the Raman transfer is not blocked by an EIT-type process as proposed by Müller *et al.* [20], so that the condition that $\Omega_{\rm c} > 2\Omega_{\rm p}$ is not required. The large Raman beam detuning used in Ref. [49] will therefore minimise the effect of spontaneous decay from the intermediate state and maintain a high gate fidelity.

The second contribution to the absence of clear Raman transfer is the performance of the optical pumping required to prepare the atoms in a pure initial state. With the sample of atoms in a random distribution of initial m_F states many Raman transfer channels are possible, each with a different Rabi frequency. This may result in the Rabi oscillations becoming 'washed out' and difficult to observe. The possible Raman transfer routes available with a combination of σ^+ and π transitions are shown in Fig. 4.12. If all atoms are optically pumped into the $|F = 2, m_F = 2\rangle$ state Raman transfer with effective Rabi frequency $\Omega^R_{\rm eff}$ will occur and other possible routes are labelled $\Omega^m_{\rm eff}$ (where $m = 1, 2, 3$). The effective Rabi frequency is found using:

$$\Omega_{\text{eff}} = \frac{\Omega_{\text{p}}\Omega_{\text{s}}}{2\Delta}, \tag{4.7}$$

where Ω_{p} and Ω_{s} are the Rabi frequencies of the two Raman beams and are found using Eq. (4.5). The ratios of each possible Rabi frequency with that expected if the initial state were $|F = 2, m_F = 2\rangle$ are shown in the table presented in Fig. 4.13 (a). For cases 2 and 3 the Raman beams are detuned 217 MHz from the intermediate $F = 1$ state. The population of atoms in the $F = 2$ state is shown as a function of time in Fig. 4.13 (b). The blue line shows the Rabi oscillations that occur for atoms optically pumped into the $|F = 2, m_F = 2\rangle$ state with Rabi frequency Ω^R_{eff}. The dashed black lines show the other possible Rabi oscillations for the different Raman transfer routes detailed in Fig. 4.12. The red line is the average of all the available Rabi oscillations and consequently has a lower visibility.

Fig. 4.13 demonstrates that additional Raman transfer routes can affect the visibility of Rabi oscillations. Therefore to increase the fidelity of the Raman transfer it would be beneficial to improve the performance of the optical pumping to ensure the atoms are in a pure initial state.

4.2.7 Outlook and summary

In order to improve the fidelity of the Raman transfer so that Rabi oscillations can be observed the method of preparing the initial state must be improved. A possible means of improving this would be to use a magnetic trap to capture atoms from the MOT. The magnetic trap can be used to hold only atoms with a single magnetic spin state so a pure initial state can be produced. The Raman transfer could also be improved by attempting to move the beams further from resonance. This must be done within the restrictions discussed in Sec. 4.2.1 in order that the Raman transfer can be blocked by coupling to the Rydberg state. Increasing the coupling beam Rabi frequency would prove advantageous but could only be achieved with a more powerful laser system or decreasing the beam waist using short focal length lenses mounted within the vacuum chamber. Both of these options would involve significant rebuilding of the experimental apparatus presented in this thesis.

(a)

m	$\Omega^{m}_{eff}/\Omega^{R}_{eff}$
1	0.35
2	0.10
3	0.11

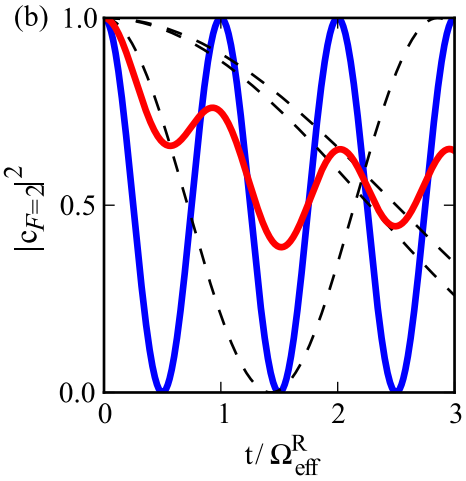

Figure 4.13: (a) Possible Raman transfer Rabi frequencies for atoms that are not optically pumped into the $|F = 2, m_F = 2\rangle$ state. (b) Shows Rabi oscillations in the population of atoms in the $F = 2$ state for the Rabi frequencies in (a). The blue line shows Rabi oscillations at Ω^{R}_{eff} for atoms optically pumped in the $|F = 2, m_F = 2\rangle$ state. The back dashed lines show Rabi oscillations for the other possible routes. The red line is an average of the possible Rabi oscillations.

To summarise, this chapter has covered the production of Raman light that employs a novel Faraday filtering technique [92] and the application of the Raman beams both in a thermal vapour cell and a sample of ultracold atoms. The desire to study Raman transfer is motivated by the C-NOT gate protocol introduced by Müller *et al.* [20]. Fundamental to this scheme is the coherent transfer of population between hyperfine ground states. The Raman beams are produced by an EOM technique requiring that the two frequency components be subsequently spatially filtered. To achieve this the Faraday effect in a vapour cell of isotopically pure ^{85}Rb is used to give a frequency dependent rotation in polarisation, allowing the Raman beams to be separated using polarisation optics. The effect of the Raman beams when applied in pump-probe spectroscopy was studied in order to confirm the correct laser frequencies are produced. The Raman beams were then used to drive Raman transfer in a sample of ultracold atoms released from the dipole trap. Finally, evidence of a 20% population transfer was observed.

Chapter 5

Laser stabilisation for Rydberg excitation

A critical element of any atomic physics experiment is the production of narrow linewidth laser light at the required frequencies. In this work not only is 780 nm light required for the magneto-optic trap; Raman beams and a two-photon Rydberg excitation are also necessary. This chapter covers the key laser stabilisation techniques used throughout this work. Although existing methods are readily available for locking to ground state transitions, coupling to Rydberg states offers a further challenge. This has led to the development of a novel laser stabilisation scheme using electromagnetically induced transparency (EIT).

In section 5.1 common laser stabilisation schemes available for ground state transitions are introduced along with their various merits and disadvantages. Section 5.2 covers modulation transfer spectroscopy [112, 119, 120], the laser stabilisation method used throughout this work, in more detail. Following this, section 5.3 introduces a scheme that allows laser stabilisation to an EIT signal [121]. The required experimental setup is given and the error signals for various experimental parameters are presented. Finally, in the last section of this chapter, the frequency stability performance of the laser system is evaluated. The linewidth of the 780 nm laser is found using a beat measurement and the performance of the 480 nm laser is evaluated by a demonstration of EIT in an ultracold ensemble.

5.1 Laser stabilisation

Many experiments require a stable frequency in the optical region of the electromagnetic spectrum [122]. Typically, an optical frequency reference is established by stabilising a laser to an optical transition. In order to stabilise the laser the spectroscopic reference signal is fed-back to the laser to counteract any drift in frequency. Typically the feedback mechanism will require the reference signal, known as the 'error' signal, to be anti-symmetric with a zero crossing centred on the atomic transition. Fundamental to laser stabilisation is therefore the means by which a suitable error signal may be generated.

Many techniques exist for producing error signals from atomic references, these include: dichroic atomic vapour laser locking (DAVLL) [123–125]; combined saturated absorption and DAVLL [126–128]; polarization spectroscopy [129]; Sagnac interferometry [130, 131]; frequency modulation (FM) spectroscopy [132, 133]; and modulation transfer spectroscopy [112, 119, 120]. These techniques each have specific advantages and disadvantages. Single beam DAVLL will produce an error signal with a broad capture range but will therefore not exhibit high frequency resolution. Sub-Doppler resolution can be achieved using pump-probe spectroscopy to produce error signals with steep gradients around the spectral feature. Of these techniques sub-Doppler DAVLL and polarisation spectroscopy may suffer from sensitivity to stray magnetic fields. For the work in this thesis the master 780 nm laser is stabilised using modulation transfer spectroscopy. This technique provides dispersive error signals, with a steep gradient, that are well centred on the spectral feature. The modulation transfer technique has advantages over FM spectroscopy: the error signal is on a zero background and has a large amplitude for closed transitions.

5.2 Modulation transfer spectroscopy

The techniques of modulation transfer spectroscopy, and the closely related frequency modulation (FM) spectroscopy, have at their foundation the modulation of the frequency of laser light. The modulation has the result of

producing sidebands on the light that are separated from the carrier by the modulation frequency. This frequency modulation can be added to conventional saturation absorption spectroscopy by directly modulating the diode drive current or passing the probe beam through an electro-optic modulator (EOM) before it reaches the vapour cell. FM spectroscopy relies on the non-linear interaction between the medium and the probe and sidebands causing them to experience different levels of absorption and dispersion. The resulting amplitude modulation can be measured as the beat note at a photodiode detecting the probe. Using rf heterodyne techniques, where the signal is mixed with a reference oscillator, the absorption and dispersion associated with the spectral feature can be determined, as demonstrated in the following section. The technique of modulation transfer differs from FM spectroscopy in that the modulation is applied to the pump beam and not the probe. If the interactions with the medium are sufficiently non-linear the modulation is transferred to the probe by a four-wave mixing process that is most efficient for closed transitions where there is no relaxation to different ground states [112]. Sidebands added to the probe will then beat with the carrier at the photodetector and absorption and dispersion signals can again be produced with a phase-sensitive demodulation technique. The four-wave mixing process that transfers the modulation will only occur where sub-Doppler resonance between the probe and pump occurs. Modulation transfer spectroscopy can therefore produce a dispersive error signal on a zero background that is required for laser stabilisation.

5.2.1 Theoretical error signal lineshapes

Light from a single frequency laser source, oscillating at ω_c, has an electric field given by $E = E_0 \sin \omega_c t$. If this beam is passed through an EOM, operating at a modulation frequency ω_m, the beam is now described by [112]:

$$E = E_0 \sin[\omega_c + M \sin \omega_m], \tag{5.1}$$

$$\begin{aligned} E &= E_0\Bigg[\sum_{n=0}^{\infty} J_n(M)\sin(\omega_\mathrm{c}+n\omega_\mathrm{m})t \\ &\quad +\sum_{n=1}^{\infty}(-1)^n J_n(M)\sin(\omega_\mathrm{c}-n\omega_\mathrm{m})t\Bigg], \end{aligned} \tag{5.2}$$

where M is the modulation index and J_n are Bessel functions with order n. The light now has a carrier component at a central frequency, ω_c, with sideband components separated by integer multiples of the modulation frequency, $\pm\, n\omega_\mathrm{m}$. The modulation index determines relative amplitude of the carrier and sidebands; for $M < 1$ the beam will be composed of a strong carrier and weak first order sidebands. The modulation transfer error signal is given, for $M \ll 1$, in Ref. [119] as:

$$\begin{aligned} S &= AJ_0J_1(\mathcal{L}_1-\mathcal{L}_{1/2}+\mathcal{L}_{1/2}-\mathcal{L}_{-1})\cos(\omega_m t+\phi) \\ &\quad +(-\mathcal{D}_1+\mathcal{D}_{1/2}+\mathcal{D}_{1/2}-\mathcal{D}_{-1})\sin(\omega_m t+\phi), \end{aligned} \tag{5.3}$$

where J_0J_1 are the Bessel functions of zeroth and first order, and A being a constant related to the properties of the medium. The phase between the modulation frequency and the signal used in the demodulation part of the detector is represented by ϕ. The terms $\mathcal{L}$ and $\mathcal{D}$ are the Lorentzian and dispersive line shapes given by:

$$\mathcal{L}_n = \frac{\Gamma^2}{\Gamma^2+(\Delta-n\omega_\mathrm{m})^2}, \tag{5.4}$$

and

$$\mathcal{D}_n = \frac{\Gamma(\Delta-n\omega_\mathrm{m})}{\Gamma^2+(\Delta-n\omega_\mathrm{m})}. \tag{5.5}$$

Here Γ is the natural linewidth of the state being probed and Δ is the detuning from the line centre of the spectral feature. By varying the phase, differing amounts of the *sine* and *cosine* terms will be detected, giving either the absorption or dispersion in the medium respectively.

Combining Eq. (5.3), Eq. (5.4) and Eq. (5.5) allows the modulation transfer signal to be plotted as a function of detuning, as shown in Fig. 5.1. The modulation frequency is set to $\omega_n/\Gamma = 1$ and panels (a) and (b) show the *cosine* and *sine* terms respectively. The signal in panel (b) has a clear dispersion like lineshape, with a zero crossing at zero detuning from the line centre, therefore it is an ideal error signal for laser stabilisation. The error signals produced by modulation transfer spectroscopy vary significantly with differing modulation frequencies, this is covered in more detail in Ref. [112].

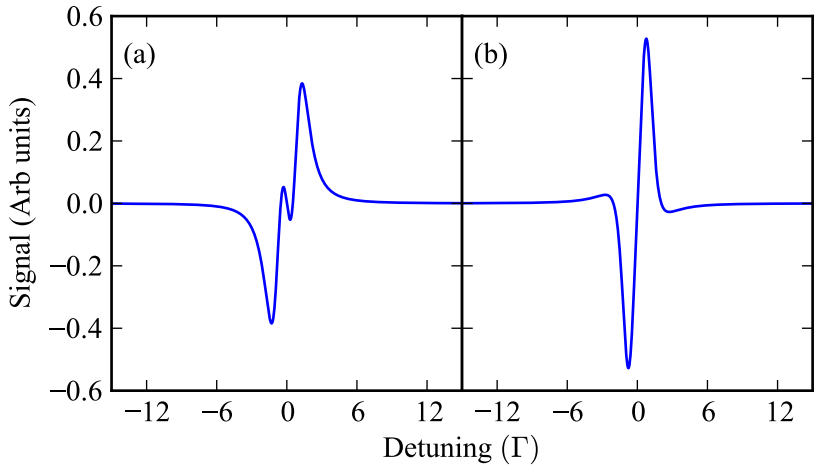

Figure 5.1: Lineshape for modulation transfer spectroscopy error signals. Panels (a) and (b) show the *cosine* and *sine* terms of Eq. (5.3) respectively. (b) has a clear dispersion-like lineshape ideal for laser stabilisation.

5.2.2 Experimental setup for modulation transfer spectroscopy

The setup of the optics and electronics required for laser stabilisation using modulation transfer spectroscopy is shown in Fig. 5.2. A probe and pump beam counter-propagate through a Rb vapour cell after which the probe is detected using a fast photodiode[1] with a bandwidth of 20 MHz. The photodiode signal is mixed[2] with the modulation signal used to drive the EOM and a phase shifter allows the dispersion lineshape to be selected as previously

[1]Hamamatsu APD C5460 20 MHz

[2]Mini-Circuits ZAD-6+

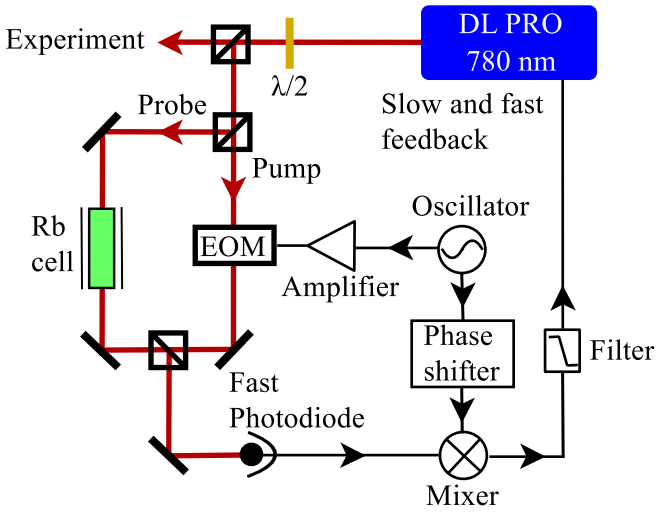

Figure 5.2: Schematic experimental setup for modulation transfer spectroscopy used for laser frequency stabilisation of the master 780 nm laser. A probe and pump beam are counter-propagated through a Rb vapour cell after which the probe beam is detected on a fast photodiode with a 20 MHz bandwidth. The pump beam is first passed through an EOM driven sinusoidally to produce sidebands. The EOM modulation signal is phase shifted and mixed with the photodiode signal. The output of the mixer is then filtered to produce an error signal that can be fed back to the laser current and piezo control to stabilise the frequency.

described. Finally the signal is filtered with a ∼20 kHz low pass filter before being fed back to the laser current and piezo controls. Commercial PID type feedback electronics with a high bandwidth[3] are used to stabilise the laser.

The probe beam is modulated using an EOM built to the design detailed in Ref. [112]. The EOM consists of a lithium tantalate crystal mounted between the plates of a capacitor in a simple LC circuit. The sidebands generated can be measured by passing the light through a scanning Fabry–Pérot etalon, an example of which is shown in Fig. 5.3 (a), where the first and second order sidebands are clearly visible. The resonance frequency of the LC circuit is found by varying the driving frequency and measuring the ratio of the sideband magnitude to the carrier. The result of this measurement is shown in Fig. 5.3 (b), where the data have been fit with a Lorentzian function. The resonance frequency is found to be 13.8 MHz.

[3]Toptica FALC module

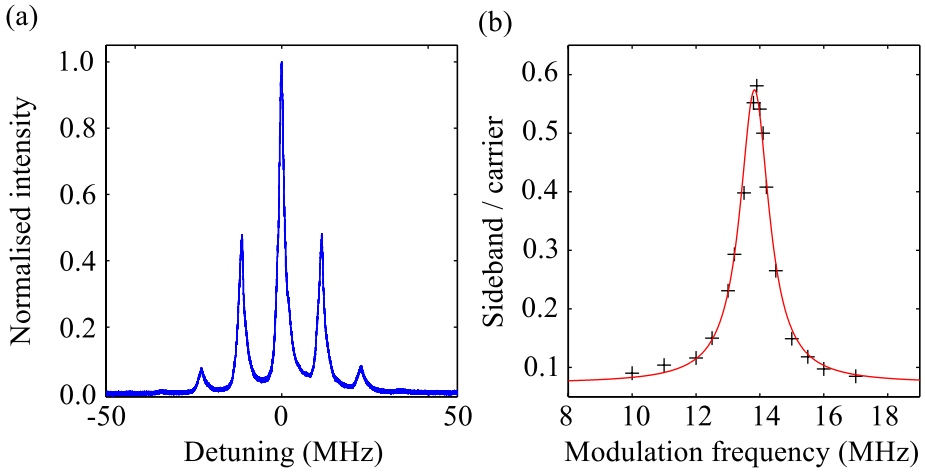

Figure 5.3: (a) Fabry-Pérot etalon signal showing the sidebands created by the EOM. For high modulation depths near resonance the first and second order sidebands are clearly visible. (b) The ratio of the first order side band amplitude to the carrier is plotted as a function of the modulation frequency. The data are then fit with a Lorentzian function to find the resonant frequency.

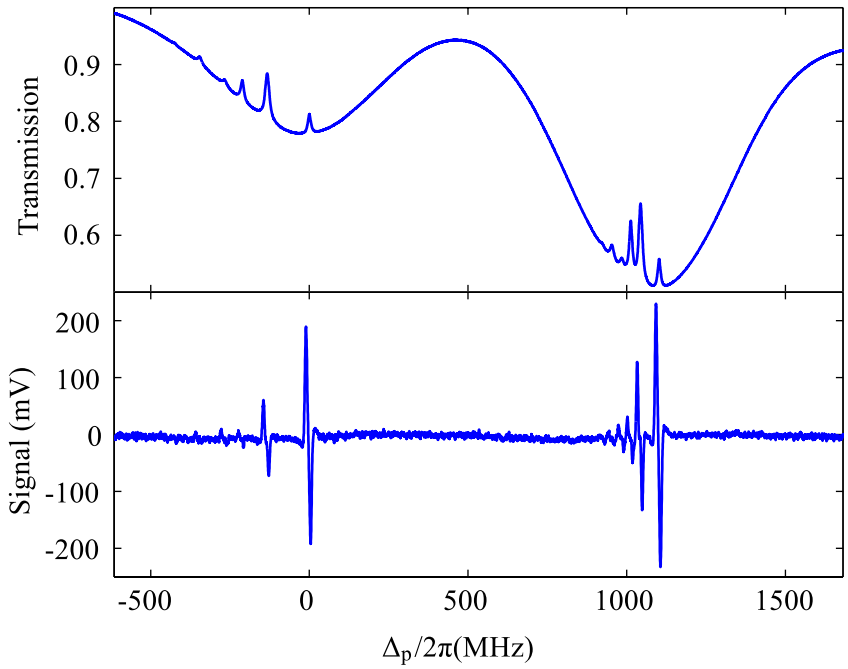

Figure 5.4: Saturated adsorption spectroscopy and corresponding modulation transfer spectroscopy signal for the 5s $^2S_{1/2}(F = 2) \rightarrow$ 5p $^2P_{3/2}(F')$ transition in ^{85}Rb and ^{87}Rb.

The error signals and corresponding saturated absorption spectroscopy of the 5s $^2S_{1/2}(F = 2) \rightarrow$ 5p $^2P_{3/2}(F')$ transition in ^{87}Rb and 5s $^2S_{1/2}(F = 3) \rightarrow$ 5p $^2P_{3/2}(F')$ in ^{85}Rb are presented in Fig. 5.4. The error signals have a zero background and a large amplitude for the closed transitions as expected. Using this signal the 780 nm master laser is stabilised to the 5s $^2S_{1/2}(F = 2) \rightarrow$ 5p $^2P_{3/2}(F = 3)$ cooling transition in ^{87}Rb. From this all necessary light for the MOT cooling, repump, Raman and Rydberg probe beams is referenced.

5.3 Cascade EIT laser stabilisation

The methods for laser locking described in the previous section are ideal for laser stabilisation to ground state transitions. A limitation of these schemes is that one is restricted to wavelengths corresponding to transitions with a significant population in the lower state or with sufficiently large Einstein A-coefficient to produce an absorption signal. For the two photon cascade electromagnetically induced transparency (EIT) system described by the energy level diagram of Fig. 5.5 the coupling beam, λ_c, must be stabilised to a transition from an intermediate state to a Rydberg state. This transition has little population in the lower state and a small Einstein A-coefficient therefore requiring an alternative laser stabilisation method to be implemented. In this situation a frequency comb [134] or a reference cavity stabilized to a ground state transition [135] are possible alternatives. However, these methods are limited by the stability of the cavity, which is influenced by environmental factors such as temperature and pressure.

For the experiments presented in this thesis a technique which enables laser stabilisation to transitions between excited states based on atomic coherences has been developed [121]. The technique is based on EIT allowing information about a weak excited-excited state transition to be transferred to a strong probe transition. EIT has been used previously as a dispersive reference to lock the relative frequency of two lasers to an atomic ground-state hyperfine splitting [136]. Also Doppler-free two-colour spectroscopy has been used to lock to excited-excited state transitions where the lower state is populated [137]. In contrast to other methods this scheme uses a probe laser,

λ_p to stabilise a second laser, λ_c, at a completely different wavelength, as shown in Fig 5.5 (a). This allows laser stabilization to transitions with small Einstein A-coefficients (of order 100 Hz) such as the transitions to Rydberg states required in this work. As the technique is based on an atomic coherence one can obtain resonance widths which are smaller than the natural broadening of the intermediate state. In principle, the technique is applicable to any excited state transition allowing a large number of additional potential optical frequency references.

In order to produce an error signal the frequency modulation spectroscopy technique of Ref. [132] and [133] is used with the spectral feature provided by the EIT signal. The probe beam is modulated to give sidebands above and below the EIT resonance which then beat with the probe beam carrier to produce a detector signal at the modulation frequency. Using a phase-sensitive detection scheme, dispersion and absorption components can be recovered to form an error signal. With the probe beam locked and the coupling beam scanning through resonance an EIT feature is observed on the transmission of the probe at both the carrier and sideband frequencies as

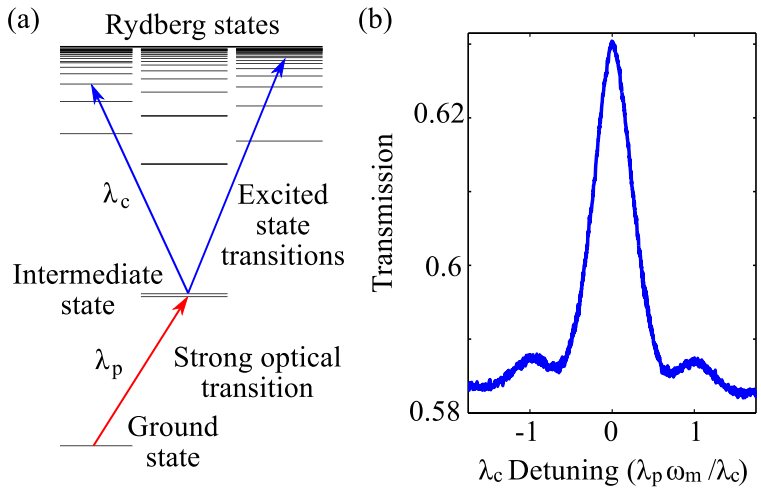

Figure 5.5: (a) Energy level diagram of a two photon transition to a highly excited state in a typical alkali atom system. By probing the strong ground state transition the excited state transition is detected using EIT. (b) A typical EIT spectrum as the coupling laser is scanned across resonance and the probe beam fixed on resonance. An EIT resonance is oberved at both the carrier and sideband frequencies, $\omega_0 \pm (\lambda_p/\lambda_c)\omega_m$.

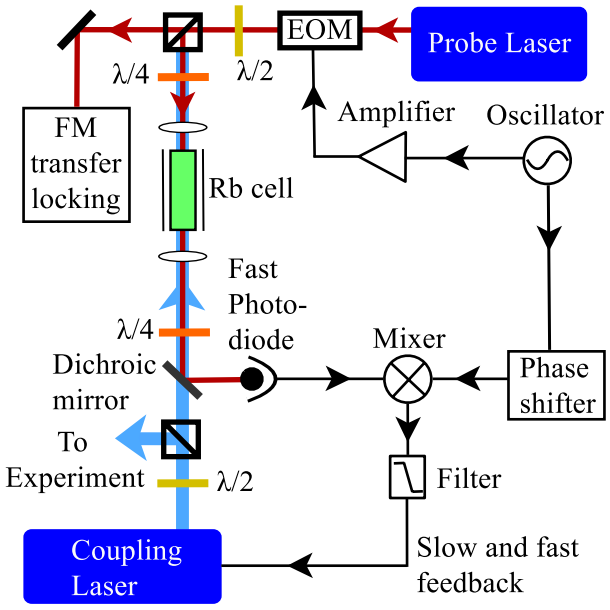

Figure 5.6: Schematic experimental setup for EIT laser stabilisation. The coupling and probe laser are counter-propagated through a magnetically shielded Rb vapour cell. The probe beam is modulated using an EOM and detected using a fast photodetector. This signal is mixed with the oscillator to produce an error signal that is fed back to the coupling laser.

shown in Fig. 5.5 (b). Note that due to the Doppler mismatch between the probe and coupling beams, the frequency offset of the sidebands is scaled by a factor of λ_p/λ_c. The cascade system in question consists of a weak probe beam resonant with the ^{87}Rb 5s $^2S_{1/2}(F = 2) \rightarrow$ 5p $^2P_{3/2}(F = 3)$ transition followed by an intense coupling beam resonant with the 5p $^2P_{3/2}(F = 3) \rightarrow$ nd ^{2}D or 5p $^2P_{3/2}(F = 3) \rightarrow$ ns ^{2}S transitions.

The experimental setup is shown in Fig. 5.6. A 780 nm probe beam and 480 nm coupling beam are counter-propagated through a magnetically shielded Rb vapour cell. Both beams initially have a radius of approximately 1 mm and are focused through the cell using a pair of $f = 200$ mm lenses. The beams are focused in order to increase the coupling beam Rabi frequency, this allows EIT to be observed for transitions to Rydberg states which have small A-coefficients. The probe light is frequency stabilised as described in the previous section. The probe beam is frequency modulated using an EOM

driven by an amplified[4] sinusoidal signal from an oscillator. Following the vapour cell the probe beam is incident on a fast photodiode[5]. The photodiode signal is frequency mixed[6] with the oscillator after passing through a phase shifter and filter. The error signal is fed back to both the laser current and the external cavity piezo after a 20 kHz low pass filter.

Examples of the resulting error signals while scanning the coupling laser are shown in Fig. 5.7. For Rydberg states with intermediate values of the principal quantum number, e.g. $n = 26$ in Fig. 5.7 (a), an error signal with good signal to noise is obtained with laser powers of under 1 mW. For increasing principle quantum number, e.g. $n = 70$ in Fig. 5.7 (b), error signals have been observed with still modest amounts of laser power. For yet higher Rydberg states and transitions with smaller dipole matrix elements (the Einstein A-coefficient for the 5p-ns transitions is an order of magnitude less than 5p-nd) significantly higher powers are required.

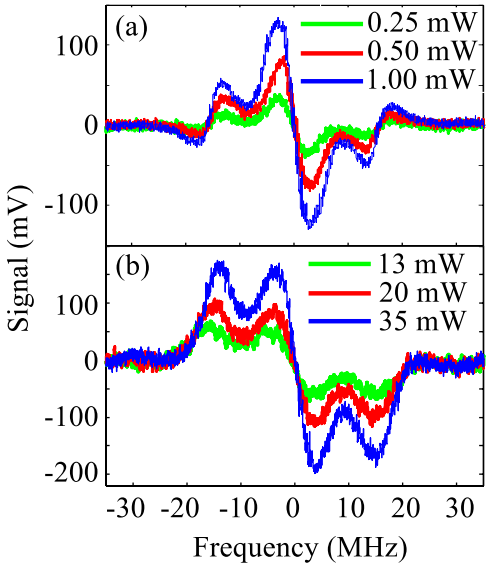

Figure 5.7: Locking signal at varying coupling beam powers. The probe beam was fixed at a power of 4 μW and was locked to the ^{87}Rb 5s $^2S_{1/2}(F = 2) \rightarrow$ 5p $^2P_{3/2}(F' = 3)$ transition and modulated at 10 MHz using an electro–optic modulator (EOM). The coupling beam is tuned to the (a) 26D and (b) 70S Rydberg state and scanned through resonance

[4]Mini-Circuits ZHL-3A
[5]Hamamatsu APD C5460 10 MHz
[6]Mini-Circuits ZAD-6+

5.4 Laser stabilisation performance

In order to evaluate the stability of the laser system several methods were employed. The performance of the Rydberg coupling laser is dependent on both the linewidth of the 480 nm laser and the 780 nm master laser it is referenced to because of the two-photon EIT stabilisation scheme. The linewidth of the 780 nm master laser can be readily evaluated by measuring its beat signal with an equivalent system. In order to find absolute linewidths the beat signal between all possible pairs of three equivalent laser systems must be measured. To achieve this, beams derived from three lasers were used: a home built diode laser, stabilised using polarisation spectroscopy; a commercial Toptica DL MOD laser, stabilised using modulation transfer spectroscopy; and a Toptical DL PRO also stabilised using modulation transfer spectroscopy (the system described in the previous section). A beams from each laser was set to approximately the same power and coupled into an optical fibre to ensure good spatial overlap and equal polarisation. The output light was then focused onto a high bandwidth photodiode[7] and beat signals recorded using a spectrum analyser[8]. This allows the power spectral density (PSD) at each frequency component to be measured. The light from each laser was shifted in frequency using an acousto-optic modulator (AOM) so that the beat signal appeared at a known frequency offset.

An example of the resulting beat measurement is shown in Fig. 5.8. The width of the beat signal is found by fitting a Lorentzian to the data. The beat note measured has a width equal to the sum of the linewidths of the individual lasers. From the set of beat notes measured the absolute linewidth of each laser can be found and is listed in the table in Fig. 5.8. The linewidth was determined in this way over time scales between 3.5 seconds and 170 seconds and found to vary between approximately 200 and 350 kHz. The reduction of the linewidth when measured over longer time scales is an artefact of the uncertainty in the measurement.

A direct measurement of the Rydberg coupling laser linewidth made by beating three lasers together cannot be made because adequate equivalent sys-

[7] EOT ET-2030A
[8] Agilent CSA N1996A

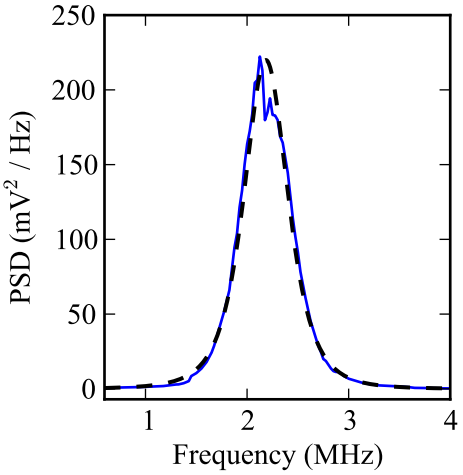

N_{av}	10	50	100	500
Time (s)	3.5	17	34	170
ν_{pro} (kHz)	343	315	306	195
ν_{mod} (kHz)	455	472	468	594
ν_{hb} (kHz)	424	396	451	572

Figure 5.8: Beat signal between light from the DL PRO and DL MOD lasers both stabilised using FM transfer spectroscopy. The data are fit with a Lorentzian, shown by the dashed black line, to give the linewidths shown in the table. The beat signals are measured over different time periods to evaluate the stability of the laser over different time scales. The table shows the linewidth for each of the lasers: the DL PRO, ν_{pro}; the DL MOD ν_{mod}; and homebuilt laser, ν_{hb}.

tems are not available. However, other approximate methods to evaluate the performance of the laser stabilisation are possible. Firstly, an estimate of the lower limit on the linewidth of the coupling laser system is made by measuring the rms noise of the error signal. As the amplitude of the error signal depends on the coupling laser power it is possible to increase the gradient of the error signal without increasing the amplitude noise due to probe laser intensity fluctuations or electronic noise. Frequency noise and amplitude noise can consequently be identified and which of these limits the stability of the lock determined. The rms noise of the locking signal (averaged over a period of 1 minute) when the laser is stabilised was measured and divided by the gradient of the unstabilised signal to give a linewidth estimate for the 26D Rydberg state error signals. With a coupling power of 0.5 mW the gradient of the error signal was 20 mV/MHz giving a linewidth of 200 kHz. A coupling power of 1.0 mW gave a gradient of 70 mV/MHz and a linewidth of 50 kHz. Finally, a power of 2.4 mW gave a gradient of 110 mV/MHz and a linewidth of 35 kHz, illustrating that for these parameters the linewidth is primarily limited by the gradient of the error signal and hence the coupling laser power used in the locking scheme.

Secondly, an estimate of the combined linewidth of the probe and coupling laser is made by performing a two-photon Rydberg excitation measurement on an ultracold atomic ensemble using the apparatus described in Ref. [74] and [138]. The probe and pump beam is counter-propagated through a cloud of laser cooled Rb atoms. The probe beam is scanned through the ^{85}Rb D_2 $F = 3 \rightarrow F' = 4$ transition using an acousto-optic modulator (AOM) in a time of 0.32 ms to produce the EIT spectra in Fig. 5.9. These data are fit using the model presented in Ref. [74] and [138] and indicate a combined relative laser linewidth of 280 ± 50 kHz.

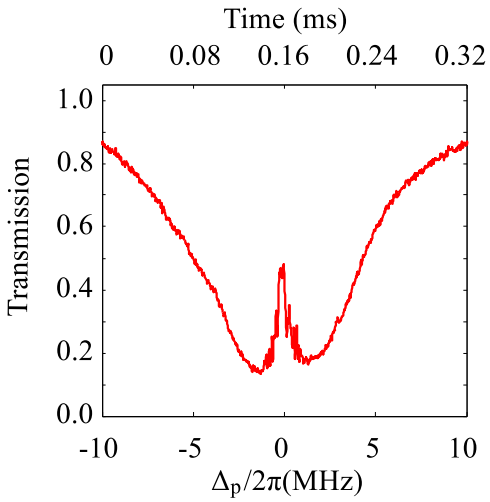

Figure 5.9: Transmission of a 200 nW probe beam as a function of probe beam detuning for the $5S_{1/2} \rightarrow 5P_{3/2} \rightarrow 26D$ transition. The probe laser is scanned over 20 MHz in 0.32 ms. The coupling beam power is 84 mW. The data were taken using the apparatus described in Ref. [74] and the laser system described in this thesis. The narrow EIT feature gives a combined laser linewidth of 280 ± 50 kHz.

5.5 Summary

The key laser stabilisation techniques required for the experiment have been described and experimental setup details given. Modulation transfer spectroscopy was chosen to stabilise the master 780 nm laser required for the experiment because it readily produces dispersive-like error signals, with a large amplitude for closed transitions, on a constant zero background. Light from this laser is used both for MOT cooling light and as a probe beam for

the two-photon Rydberg excitation scheme. The light required for the MOT repump and Raman beams is also referenced to this master laser as described in Chapter 4. In order to stabilise the 480 nm Rydberg coupling laser a novel scheme to lock to an EIT signal in a vapour cell has been developed. The details of this scheme have been given and example error signals presented. Finally, the stability of the laser system has been considered; beat measurements of the 780 nm laser light were made in order to find the linewidth. An evaluation of the 480 nm laser linewidth was made by measuring Rydberg EIT in an ultracold ensemble of atoms.

Chapter 6

Rydberg EIT and electrometry

The first section of this chapter builds on the laser stabilisation work by employing EIT as a non-destructive probe of the Rydberg state of ultracold atoms. In Sec. 6.1.1 the experimental setup required to measure an EIT spectrum is detailed. Following this an example of how data obtained in this way are fit with a theoretical lineshape is given.

The EIT spectra provide a means to readily measure the energy shift of the Rydberg state. As this shift is dependent on the electric field at the position of the atoms a method of carrying out electrometry is possible and is demonstrated in Sec. 6.2. The design of the vacuum chamber means that a dielectric surface is positioned close to the ultracold atoms. It is found that the presence of this dielectric and adsorbates on its surface have a strong affect on the Rydberg energy level shift. In Sec. 6.2.4 the Rydberg energy level shift corresponding to a calculated electric field is compared to the experimental results. Good agreement is found only where the dielectric material is included in the electric field model.

6.1 Rydberg EIT in an ultracold ensemble

Ultracold ensembles of Rydberg atoms have been the subject of much study in recent years. The collective behaviour of Rydberg atoms has been studied extensively in work on the dipole blockade [29–31] and superradiance [38]. Ultracold samples of Rydberg atoms have also found applications in elec-

trometry [64, 65] which is the motivation behind the work presented in this chapter.

In most experiments involving ultracold Rydberg atoms the presence of the Rydberg atoms is detected indirectly by means of a micro-channel plate (MCP). The Rydberg atoms are ionized by either field or laser ionisation and the electrons (or ions) produced detected by the MCP. In this work an alternative method of directly detecting the Rydberg state is used. Following work done on Rydberg state detection in thermal vapour cells [41, 60, 61, 72, 73] using electromagnetically induced transparency the technique has been extended to ultracold atoms [39, 74]. EIT provides a suitable probe of the Rydberg state; it provides a method of optical detection, at convenient wavelengths, and is non-destructive.

Electromagnetically induced transparency (EIT) is a coherent process where the absorption of probe light resonant with a transition between two states is modified by a strong coupling to a third state. If this strong coupling is to a Rydberg state the properties of that state are mapped onto the probe transition. As the probe intensity is weak only a very small population of atoms are excited to the Rydberg state. This technique is therefore non-destructive; the frequency of the probe can be scanned over resonance and an entire spectrum measured on a single ultracold sample [74]. This is technically advantageous over methods that employ an MCP because the repetition rate of the experiment may be much higher.

The work presented previously in this thesis provides all the tools required to measure EIT in a sample of ultracold atoms. A sample of atoms is loaded into the MOT using the techniques detailed in Chapter 3. The probe and coupling beams, stabilised by the method covered in Chapter 5, are then applied in a cascade EIT system.

6.1.1 Experimental setup and procedure

The experimental setup for electromagnetically induced transparency measurements is shown in Fig. 6.4. The probe and coupling beam are propagated through the vacuum chamber and focused to a point coinciding with the position of the MOT. Light for both beams is provided from single mode po-

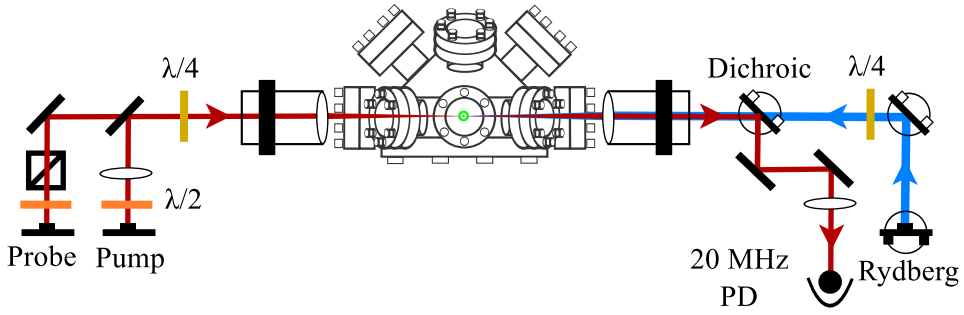

Figure 6.1: Experimental setup for EIT spectroscopy on atoms released from the MOT. The probe beam and Rydberg coupling beam are counter-propagated through the chamber such that they are focused onto the MOT position. Optical pumping light is provided along the same axis as the probe. The probe is separated from the Rydberg coupling beam using a dichroic mirror and the probe subsequently detected using a fast photodiode.

larisation maintaining fibres to provide high quality Gaussian beams. Both beams are focused using $f = 160$ mm lenses in order to produce a $1/e^2$ diameter of ~ 100 μm at the focus. Both beams are circularly polarised to maximise transition strength and thus produce a larger EIT feature. After passing through the sample of cold atoms the probe beam is separated from the Rydberg coupling beam, using a dichroic mirror, before being detected on a high bandwidth photodiode[1] with a bandwidth of 20 MHz. Optical pumping light is provided from a separate optical fiber and propagated along the same axis as the probe. This light is expanded using a $f = 160$ mm lens so it is collimated as it passes the MOT position, allowing the entire cloud to be illuminated. In addition to the pump light repump light is required for optical pumping. This is coupled into the same optical fibre as the probe.

A typical experimental sequence is shown in Fig. 6.2. The MOT is loaded as detailed in Chapter 3. Once the MOT is loaded in part ⓐ a 7 ms molasses phase, ⓑ, follows after which the cloud of atoms is allowed to expand freely. A time of 5 ms, labelled ⓒ, is allowed for the necessary closing of the MOT and repump light mechanical shutters and the opening of those for the probe and pumping beams. A 0.2 ms optical pumping phase, ⓓ, follows in order to prepare the atoms in the $|F = 2, m_F = 2\rangle$ state described in Sec. 4.2.4

[1]Hamamatsu APD C5460 20 MHz

of Chapter 4. An EIT measurement, labelled ⓔ, is made by scanning the probe beam twice, using an acousto-optic modulator (AOM), over a range ±20 MHz either side of resonance with the $|F' = 3, m_F = 3\rangle$ state in 0.5 ms while the Rydberg coupling beam is on. The sequence can then be repeated by switching the MOT back on to recapture the atoms. As EIT provides a non-destructive probe of the Rydberg state nearly all of the atoms released can be recaptured. A small MOT loading phase is required to allow time to record the data from the photodiode after which time another EIT measurement can be made. Finally, a background measurement is made so that the transmission of the probe can be calibrated. As the probe is scanned the AOM produces a spatial deviation in the beam, altering the alignment into the optical fibre. This produces a beam power that is dependent on laser frequency, an effect which can be removed by normalising the data by the background.

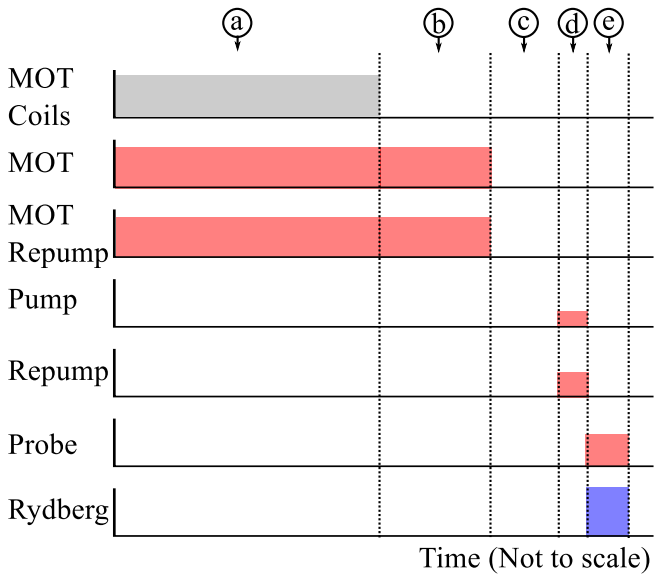

Figure 6.2: Experimental sequence for EIT spectroscopy. The MOT is loaded and then released following a molasses phase before optical pumping prepares the sample in the $F = 2, m_F = 2$ state. The probe is then scanned through resonance while the Rydberg coupling beam is on and an EIT spectrum recorded. The labels are described in the text.

6.1.2 Rydberg EIT measurement

The transmission of the probe as a function of detuning is shown in Fig. 6.3 (a). The blue data show the absorption of the probe, which has a power of 60 nW, as it is scanned through resonance. The data are smoothed with a 16 point moving average. The green data show the probe transmission in the presence of the Rydberg coupling beam, resonant with the 5p $^2P_{3/2}$ (F'=3) $\rightarrow$ 28s $^2S_{1/2}$ transition with a power of $\sim$20 mW. An EIT feature is clearly visible as a narrow transparency window in the absorption of the probe.

These spectra can be fit by calculating the susceptibility of the probe beam in the cascade system EIT shown in the energy level diagram of Fig. 6.3 (b) where the ground state, $|g\rangle$, is coupled to an excited state, $|e\rangle$, with a probe beam of Rabi frequency Ω_p, which is in turn coupled to the Rydberg state, $|r\rangle$, by a Rydberg coupling beam of Rabi frequency Ω_c. The states $|e\rangle$ and $|r\rangle$ have natural decay rates Γ_e and Γ_r respectively. The probe susceptibility, in the limit where the probe is weak and the Doppler shift is negligible, is given by [139]:

$$\chi = \frac{iNd_{ge}^2/\epsilon_0\hbar}{\gamma_{eg} - i\Delta_\mathrm{p} + \frac{\Omega_\mathrm{c}^2/4}{\gamma_{rg} - i(\Delta_\mathrm{p}+\Delta_\mathrm{c})}}, \tag{6.1}$$

where N is the atom number density, d_{ge} is the dipole moment matrix element for the $|g\rangle \rightarrow |e\rangle$ transition and $\Delta_\mathrm{p,c}$ are the detunings of the probe and coupling beams respectively. The decay rates, γ_{ij}, are related to the natural decay rates by $\gamma_{ij} = (\Gamma_i + \Gamma_j)/2$ (where $\Gamma_g = 0$). The absorption of the probe is then given by the imaginary part of this susceptibility:

$$\frac{I}{I_0} = \exp\left(-k\mathrm{Im}\chi L\right), \tag{6.2}$$

where I/I_0 is the transmission through a sample of length L and k is the probe wavevector. Therefore, the transmission of the probe can be fit with:

$$\frac{I}{I_0} = \exp\left(\frac{-kd_{21}^2 OD}{\hbar\epsilon_0}\mathrm{Im}\left\{\frac{i}{\gamma_{12} - i\Delta_\mathrm{p} + \frac{\Omega_\mathrm{c}^2/4}{\gamma_{31} - i(\Delta_\mathrm{p}+\Delta_\mathrm{c})}}\right\}\right), \tag{6.3}$$

where the N and L of Eq. (6.2) have been replace by the optical depth, OD.

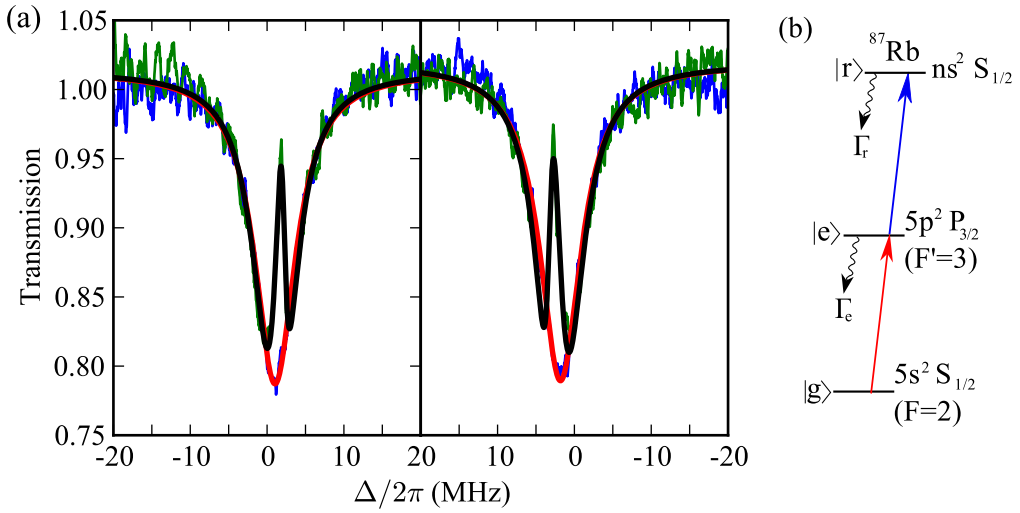

Figure 6.3: (a) Probe beam transmission as a function of detuning with (green line) and without (blue line) the Rydberg coupling laser for the 5s→ 5p→ 28s system. The black and red lines are fits to the data using Eq. (6.3); each half of the scan is fit independently. The probe beam is scanned through resonance twice in 0.5 ms. By scanning through resonance twice it is possible to check no large numbers of atoms are excited to the Rydberg state and lost from the system [74]. The EIT feature is clearly observed as a narrow transparency window in the transmission of the probe. (b) Energy level scheme for two photon cascade system EIT in ^{87}Rb. A probe, with Rabi frequency Ω_p, is scanned through the $5s^2\ S_{1/2}$ → $5p^2\ P_{3/2}$ transition which is coupled to the $28s^2\ S_{1/2}$ Rydberg state by Ω_c.

6.2 Electrometry using Rydberg EIT

6.2.1 Introduction

Rydberg atoms are a suitable tool for precision electrometry as their polarisability scales with the principal quantum number as n^7, which greatly enhances their response to electric fields in comparison to ground state atoms. Electrometry has been carried out using the highly excited Rydberg states of atoms in a supersonic beam, allowing background fields as small as ± 20 μV/cm [59] to be measured. Using samples of ultracold atoms, spatially dependent measurements of Rydberg energy level shifts have been employed to detect the presence of adsorbates on an atom chip [64] and the effect of nearby ions on Rydberg states [65]. Electric fields near surfaces have also been studied using magnetically trapped Bose-Einstein condensates. The polarization [57] and spatially resolved vector electric fields [58] of adsorbates on metals, semiconductors and insulators have been measured using this method.

The EIT technique described in the previous section is implemented to perform sensitive electrometry [140] by measuring the energy shifts of a Rydberg state. The electrometry is carried out in close proximity to the front window[2] of the vacuum chamber which is a dielectric material; the results are sensitive to the effect of adsorbates on the surface and the polarisability of the dielectric. The geometry of the experiment is shown in more detail in Fig. 6.4. Electric fields are applied using a series of four rod shaped electrodes, 3 mm in diameter and positioned in a rectangular pattern measuring 34 mm by 15 mm. The atoms released from the MOT are at the centre of the electrodes at a position that is 12.5 mm from the dielectric surface.

If the coupling laser is tuned to resonance then in an applied electric field $\mathcal{E}$ one can write:

$$\frac{\Delta_c}{2\pi} = -\frac{1}{2}\alpha_n \mathcal{E}^2, \tag{6.4}$$

where α_n is the polarizability of the Rydberg state in units of MHz/(V/cm)^2.

[2] AR coated fused silica

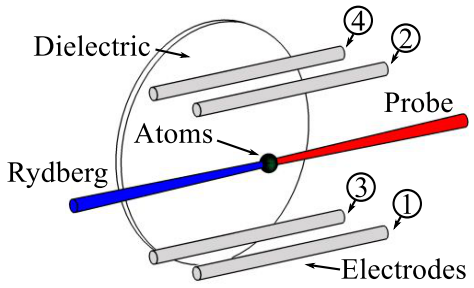

Figure 6.4: Experimental setup for electrometry using Rydberg EIT. A counter-propagating probe and Rydberg coupling beam are focused onto an ultracold sample of ^{87}Rb atoms released from a MOT. An electric field is produced using four rod shaped electrodes as shown in the diagram. The measurement is carried out near a dielectric surface positioned 12.5 mm from the MOT.

As the polarizability is known ($\alpha_{46} = 28.3$ MHz/(V/cm)^2 for the 46S in Rb used below [141]), the electric field can be calibrated by applying a known voltage to one of the electrodes and measuring the resulting shift $\Delta_c/2\pi$ of the Rydberg energy level.

Fig. 6.5 shows the effect of applying an electric field during the EIT measurement carried out as described in Sec. 6.1.2. The probe transmission, as it is scanned through resonance, is shown with and without the Rydberg coupling beam (blue and black lines respectively). The peak absorption is shifted to the red due to a quantisation magnetic field of approximately 2.5 G applied during the optical pumping and probe scan. The data showing the probe transmission in the presence of the Rydberg coupling beam show an EIT feature indicated by the arrow. In addition to the narrow EIT peak, the probe transmission shows a broader pedestal which we attribute to optical pumping processes. In panel (a) of Fig. 6.5 there is no voltage applied to the electrodes so that the EIT feature appears approximately at zero probe detuning. When a voltage is applied to the electrodes, as is the case in panel (b) of Fig. 6.5, the EIT feature is observed to shift as expected. A lineshape given by Eq. (6.3) can be used to fit these data and obtain values for the Rydberg energy level shift Δ_c and thus the local electric field.

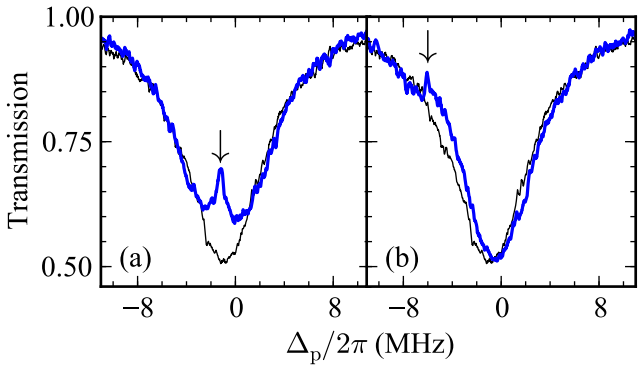

Figure 6.5: The black lines show the transmission of a 60 nW probe beam as the detuning is scanned through resonance, in a time of 250 μs. The blue line shows the probe beam transmission in the presence of a 45 mW Rydberg coupling beam for the 5s→ 5p→ 46s system. The presence of the Rydberg coupling beam is manifest as a transparency feature, indicated by the arrows, that is superposed onto the Lorentizian absorption lineshape. In panel (a) there is no external electric field applied by the electrodes and the EIT feature appears approximately at zero probe detuning. In panel (b) the EIT feature appears shifted due to the presence of an applied electric field.

6.2.2 Electrometry results

The measured Rydberg energy level shift as a function of the voltage applied to electrodes is presented in Fig. 6.6. In panel (a) the voltage is applied to the electrodes labelled ③ and ④ with the other grounded; panel (b) shows the results of applying the voltage to electrodes ① and ② with the others grounded. The voltage is applied to the electrodes throughout the duration of the experiment. Each data point represents the average of 10 experimental runs with the standard error indicated by the error bars. According to Eq. (6.4) the Stark shift is expected to be quadratic in the field. However, the data display a strong asymmetry about the zero field point. The data are fit with a function of the form:

$$\frac{\Delta_c}{2\pi} = -\frac{1}{2}\alpha(\mathcal{E} + \beta(\tau_p)|\mathcal{E}| + \mathcal{E}_0)^2, \tag{6.5}$$

where $\mathcal{E}_0$ is a constant background electric field and $\beta(\tau_p)|\mathcal{E}|$ is an additional field component which will be shown to depend on the length of time τ_p

that the voltage is applied to the electrodes. The $\beta(\tau_p)|\mathcal{E}|$ term in Eq. (6.5) reproduces the observed asymmetric effect in Fig. 6.6.

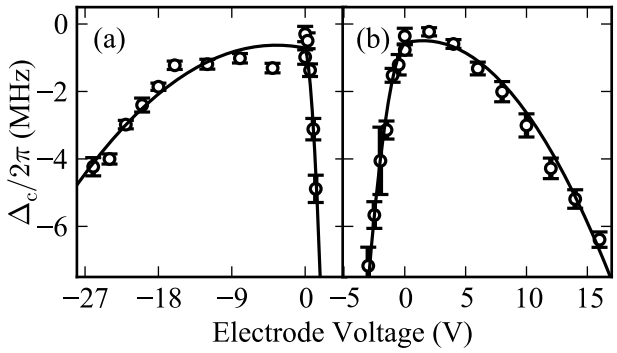

Figure 6.6: Energy level shift measurement of the 46S Rydberg state as a function of the voltage applied to the electrodes. The voltage is applied to the electrodes throughout the duration of the experiment. In panel (a) the voltage is applied to electrodes ③ and ④; in panel (b) the voltage is applied to ① and ②. The solid line is a fit to the data using Eq. (6.5).

The electric field represented by $\beta(\tau_p)|\mathcal{E}|$ is attributed to the presence of adsorbates bonded to the dielectric surface positioned close to the MOT. During construction of the apparatus a small amount of material, most likely Rb atoms emanating the dispensers, was deposited onto the dielectric surface. The electric fields produced by adsorbates on various materials have been studied by Cornell *et al.* [57][58] by measuring their effect on a Bose-Einstein condensate held in a magnetic trap. When an atom sticks to a substrate the resulting change in its electronic structure produces a dipole [57]. The valence electrons of the adsorbate will reside partially with the substrate leaving an ion at the surface. The dipoles created in this way will produce an electric field that will be proportional to the field produced by the electrodes, but will always point in a direction away from the substrate. The field produced by the electrodes, $\mathcal{E}$ in (6.5), will have a direction dependent on the geometry of the voltages applied to the electrodes. When the voltage is applied to the electrodes nearest the dielectric surface (③ and ④ in Fig. 6.4), fields $\mathcal{E}$ and $\beta(\tau_p)|\mathcal{E}|$ will add destructively and the overall field will be reduced. When the same electrodes carry a positive voltage, $\mathcal{E}$ will point in the opposite direction, and the converse will occur: fields $\mathcal{E}$ and $\beta(\tau_p)|\mathcal{E}|$ will add constructively. In

this case the overall field will be enhanced by the presence of the dipolar field. This behaviour can provide a possible explanation for the asymmetry observed in Fig. 6.6.

Although the asymmetric behaviour in Fig. 6.6 can be explained by surface dipoles, other effects may have a contribution. The presence of ions on the dielectric surface would also shift the energy of the Rydberg levels; in this case however, for a fixed number of ions, one would expect a constant background electric field. This would appear as a voltage shift in Fig. 6.6 which are included by the $\mathcal{E}_0$ term in (6.5). A time dependent number of charges, both positive and negative, would be required to produce the asymmetric Stark maps observed. Using the current setup it is not possible to confirm that surface dipoles are the only affect present.

The measured Stark map is dramatically modified if a transient electric field is applied. Similar time dependent effects have also been observed in vapour cells [61] and in cold atoms [65]. The effect of the electrode voltage pulse length, τ_p, on the Rydberg energy level shift is presented in Fig. 6.7. Two regimes are considered: the dashed line is the fit to the data shown in Fig. 6.6 (a), where the Rydberg energy level shift is measured when the voltage is applied continuously ($\tau_\mathrm{p} \to \infty$); the blue data show the Rydberg energy level shift where the voltage is pulsed ($\tau_\mathrm{p} \to 0$). In this case the voltage applied to the electrodes is on only for a time of 110 μs, coinciding with the range of the probe scan where the EIT feature is observed. Here the Rydberg energy level shift clearly has a quadratic dependence on the applied voltage and the data are fit accordingly with Eq. (6.5) with $\beta = 0$. The turning point of the quadratic does not occur at zero electrode voltage, this indicates that there is a constant background electric field of 10 mV/cm.

The relaxation time between the $\tau_\mathrm{p} \to 0$ and $\tau_\mathrm{p} \to \infty$ Stark map is determined by measuring the Stark shift Δ_c at a fixed electrode voltage of -9 V as a function of the duration τ_p of the applied field. The results are shown in Fig. 6.7(b). The solid line is an exponential fit of the form $1 - \exp(-\tau_\mathrm{p} t/T_\mathrm{a})$ with a time constant $T_\mathrm{a} \sim 1$ s. The time T_a gives an indication of the time response of the adsorbate dipoles. The electric field contribution of adsorbate dipoles can be minimized by reducing the time that electric fields are applied, i.e., by using an electric field pulse with duration $\tau_\mathrm{p} \ll T_\mathrm{a}$.

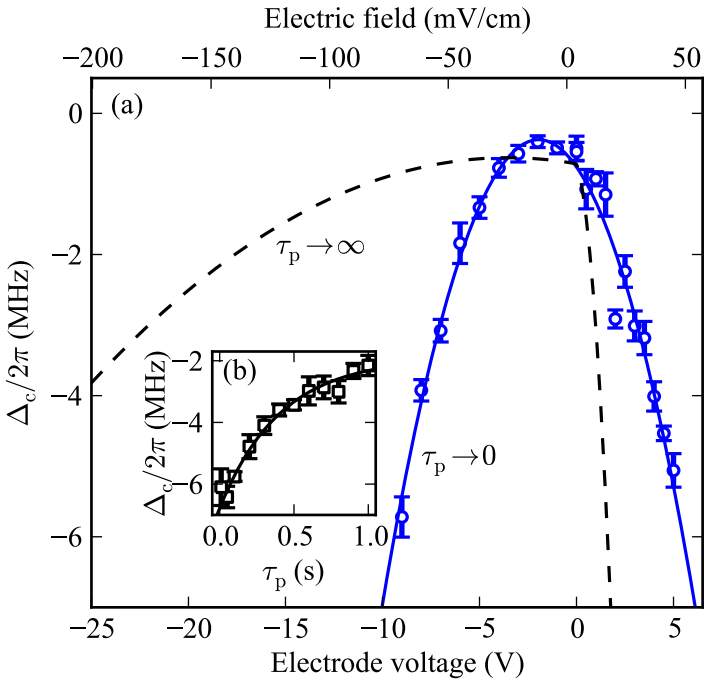

Figure 6.7: (a) Energy level shift of the 46S Rydberg state for contrasting pulse length regimes. The blue data are the measurement of the Rydberg energy level shift where the electrode voltage pulse length tends to zero ($\tau_p \to 0$). These data are fit with a quadratic and the corresponding electric field found from the polarizability. The dashed line shows the Rydberg energy shift where the electrode voltage is applied continuously ($\tau_p \to \infty$) as shown in Fig. 6.6 (a). (b) Shows the Rydberg energy level shift as a function of the voltage pulse length with the voltage fixed at -9 V.

6.2.3 Electric field calculation

The Rydberg energy level shift measured can be modelled by calculating the electric field produced by the electrodes. The electric field produced by a given spatial distribution of electrical potential is found by numerically solving Laplace's equation using the method detailed in Appendix A. The potential of the electrodes and surrounding vacuum chamber are used as the initial starting conditions and the potential found iteratively throughout the vacuum chamber.

The key areas of potential included in the calculation are shown in Fig. 6.8 (a) The area marked ⓐ is free space where the potential is given by solutions

of Laplace's equation. Area ⓑ is the surrounding metal bulk of the vacuum chamber, which is connected to electrical ground, and so must be fixed to a potential of zero. The electrodes are marked ⓒ and are fixed at the value of the voltage applied to them to create the electric field. Finally, ⓓ represents the dielectric surface of the window at the front of the vacuum chamber.

In order to give a complete description of the system the presence of the dielectric must be included in the calculation. A dielectric material in an electric field will be polarised; dipoles created within the bulk of the dielectric will produce an additional electric field that opposes the applied field, thus reducing the overall electric field within the material. This reduction in electric field within the bounds of the dielectric is included in the electric field model by reducing the potential in this region. The calculation is carried out in two parts: firstly the potential throughout the chamber is calculated without the dielectric; secondly the calculation is repeated with the potential found at the dielectric modified. Each time the iteration process is carried out the potential at all points in the model, $\phi(x, z)$, is found from an initial known geometry of potential, $\phi_I(x, z)$. In the first part of the calculation $\phi_I(x, z)$ consists of the electrodes and bulk of the vacuum chamber, labelled

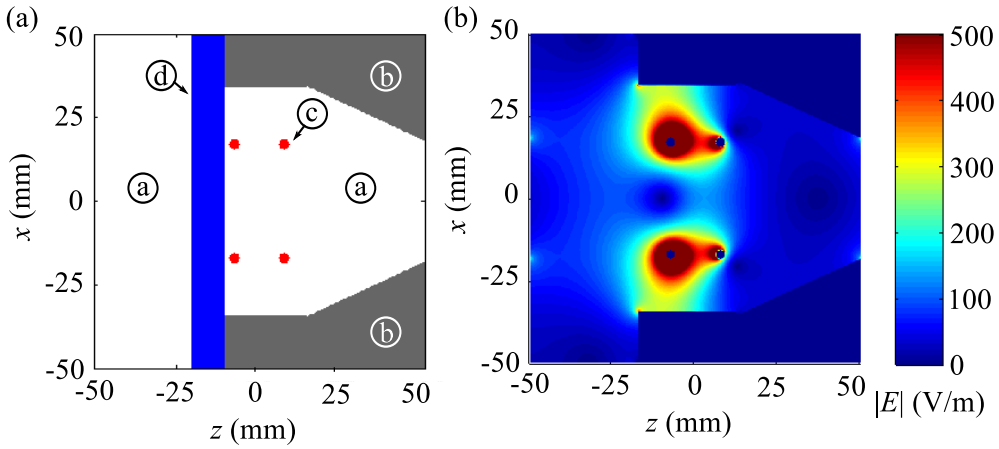

Figure 6.8: (a) Geometry of the key features of the potential used in the electric field calculation. The labelled areas are: ⓐ free space; ⓑ the metal bulk of the vacuum chamber; ⓒ the electrodes; and ⓓ the dielectric. (b) Resulting electric field magnitude calculated by including only the potential at the electrodes and vacuum chamber.

ⓑ and ⓒ in Fig. 6.8 (a). The iteration process is then completed to give the potential without the dielectric present, $\phi_0(x, z)$. From this potential the electric field can be calculated and is shown in Fig. 6.8 (b). For this specific example the electrodes nearest the dielectric are given a potential of -8 V and the other electrodes are fixed at 0 V. The second part of the calculation begins by setting $\phi_I(x, z)$ equal to $\phi_0(x, z)$ but with the potential within the bounds of the dielectric reduced by a constant factor, η, which represents the permittivity of the material. If the dielectric is bound by the region $(x, z_{d_1} < z < z_{d_2})$ in the x and z co-ordinates of Fig. 6.8 (a) the second part of the calculation proceeds with $\phi_I(x, y)$ given by:

$$\phi_I(x,z) = \begin{cases} \phi_0(x,z), & \text{if } z < z_{d_1} \text{and } z > z_{d_2} \\ \phi_0(x,z)(1-\eta). & \text{if } z_{d_1} < z < z_{d_2} \end{cases} \tag{6.6}$$

In this way the potential and corresponding electric field is reduced within the bounds of the dielectric. The iteration process is again carried out to give the complete model of the potential that includes the dielectric and is consistent with Laplace's equation. The value of η is chosen such that agreement is found between this model and the measured Rydberg energy level shifts. The results of the two stages of the calculation, the magnitude of the electric field without and with the dielectric, are shown in Fig. 6.9 (a) and (b) respectively. It is clear that within the bounds of the dielectric, indicated by the dotted vertical lines in Fig. 6.9 (b), the electric field is diminished. As a consequence of this the electric field at the centre of the electrodes (the position of the atoms) is also reduced. This effect is seen more clearly in the slices through the electric field and potential shown in Fig. 6.10 and Fig. 6.11.

The panels of Fig. 6.10 and Fig. 6.11 show slices through the calculated potential and electric field along the lines where $x = 0$ and $z = 0$. The black lines show the calculation without the dielectric and the blue lines show the results of when the dielectric is included; the relative position of the dielectric is shown by the vertical green lines and the electrodes by the red lines. The value of η in Eq. (6.6) is set to 0.4. The three panels of Fig. 6.10 show specifically: (a) the potential as a function of the distance along

the z direction; (b) the electric field in the x direction as a function of the distance along the z direction; and (c) the electric field in the z direction as a function of the distance along the z direction. Similarly, Fig. 6.11 shows: (a) the potential as a function of the distance along the x direction; (b) the electric field in the x direction as a function of the distance along the x direction; and (c) the electric field in the z direction as a function of the distance along the x direction.

The potential in Fig. 6.10 (a) shows that the presence of the dielectric has a strong effect at the position of the atoms. Within the dielectric the potential is reduced by the dielectric as required. The minimum of this potential is not at the centre of the electrodes because of the shape of the grounded vacuum chamber potential. This shape is asymmetrical in the z direction and therefore moves the potential minimum off-centre. The geometry of the system produces an electric field that is zero in the x direction as shown in Fig. 6.11 (b). The z component of the field in Fig. 6.11 (c) is the derivative of the potential in Fig. 6.11 (a) and again shows a strong effect caused by the dielectric. At the boundary of the dielectric a discontinuity arises and the field within the material is reduced. The ratio of the electric field with and without the dielectric is related to the relative permittivity of the material $\epsilon_{\mathrm{r}} = \mathcal{E}/\mathcal{E}_{\mathrm{D}}$ [142] and is set by the value of η. Although the electric

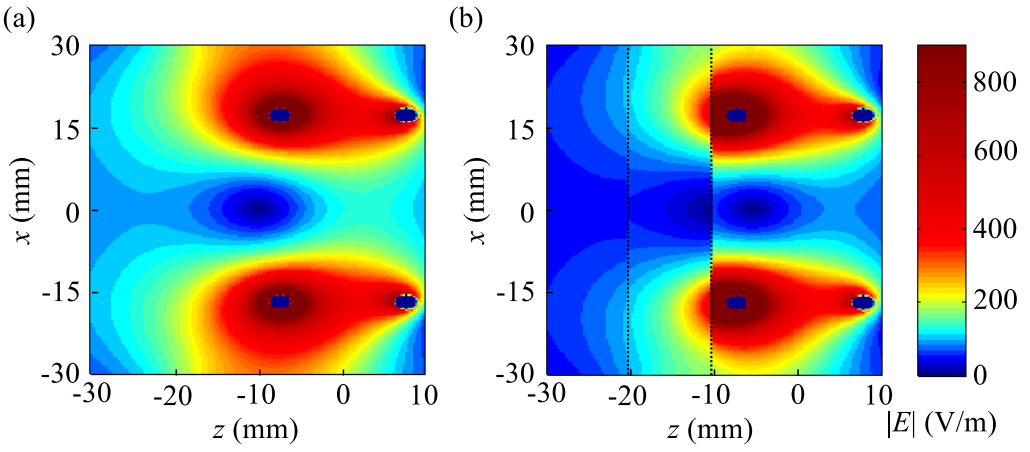

Figure 6.9: (a) Result of the calculation of the electric field magnitude without the dielectric. (b) The calculated electric field magnitude with the inclusion of the dielectric bounded by the dashed vertical lines.

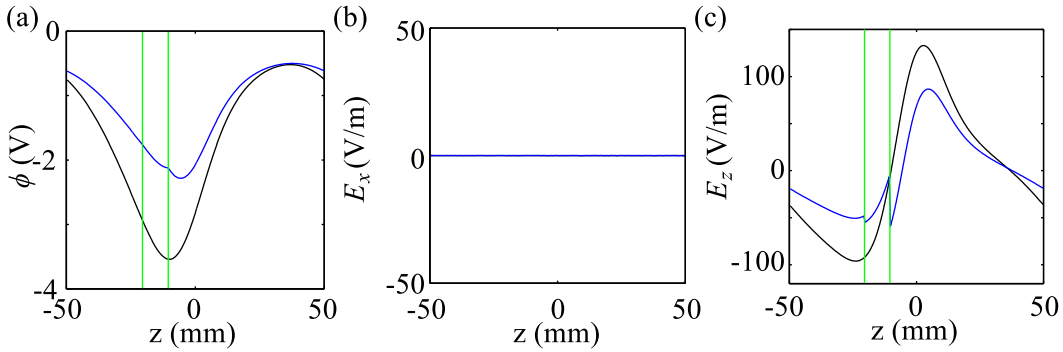

Figure 6.10: Slices through the calculated potential and electric field along the line where $x = 0$. Panel (a) shows the potential, (b) the electric field in the x direction and (c) the electric field in the z direction. Black and blue lines show the result of the calculation without and with the dielectric, respectively. The vertical green lines indicated the position of the dielectric.

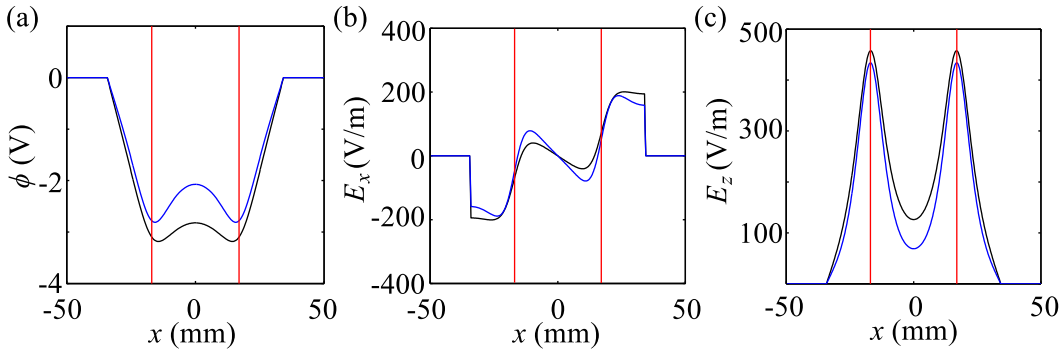

Figure 6.11: Slices through the calculated potential and electric field along the line where $z = 0$. Panel (a) shows the potential, (b) the electric field in the x direction and (c) the electric field in the z direction. The black and blue line shows the result of the calculation with and without the dielectric respectively.

field exhibits a discontinuity across the dielectric boundary, the electric displacement field, $D = \epsilon_r \epsilon_0 \mathcal{E}$ [142], is continuous. This therefore models the expected behaviour of a dielectric material.

Fig. 6.11 (a) again shows a strong effect from the inclusion of the dielectric. In this case the potential is symmetrical in shape because of the symmetric geometry of the system in the x direction. The zero potential furthest from the centre of Fig. 6.11 (a) marks the extent of the metal bulk of the vacuum chamber which is set to ground. The potential is seen to be largest at positions closest to the electrodes, indicated by the vertical red lines, as

one would expect. Fig. 6.11 (b) shows the electric field component in the x direction and is hence the derivative of the potential in Fig. 6.11 (a). At the position of the atoms this is zero, which corresponds to the zero of Fig. 6.10 (b). Finally, the z component of the field is observed to be minimum at the position of the atoms and is again strongly affected by the dielectric.

With a model in place to calculate the local electric field at the position of the atoms, including the effect of the dielectric, the measurements from the previous section can be simulated. Once the local electric field is calculated for the voltage applied to the electrodes the Rydberg energy level shift may be obtained as discussed in the following section.

6.2.4 Calculation of Rydberg energy level shifts

The Rydberg energy level shift is related to the local electric field by the relation:

$$\frac{\Delta_{\mathrm{c}}}{2\pi} = -\frac{1}{2}\alpha_{46}\mathcal{E}^2. \tag{6.7}$$

Here α is the polarisability of the Rydberg state in question and $\mathcal{E}$ is the electric field. The value of the polarisability may either be found by applied the n^7 scaling to the known value of a particular state [71] or calculated as described in Ref. [138]. For the measurements carried out in the previous section the Rydberg state is 46S giving $\alpha_{46} = 28.384 \times 10^{-4}$ MHz/(V/m^2). The atoms are all assumed to be positioned at the centre of the electrodes and the electric field at this position is obtained from the calculation described in Sec. 6.2.3.

A comparison between the measured and calculated level shifts for different combinations of live electrodes is shown in Fig. 6.12 and compared to experimental measurements carried out using the method previously described. The measurements are made in the transient applied field regime, with $\tau_{\mathrm{p}} = 110\ \mu s$ such that $\beta = 0$ in Eq. (6.5), to eliminate the effect of surface adsorbates. Each panel of Fig. 6.12 shows data for a different layout of electrode voltages detailed in the inset diagrams, where the solid circles represent a live electrode. The dashed lines are the result of the electric field

calculation with the dielectric surface omitted from the model and the solid lines show the result of its inclusion. The addition of the dielectric clearly improves the model and gives good agreement to the data. The effect of the dielectric is most prominent in the cases where the voltage is applied to electrodes near to the dielectric, shown in panels (b) and (c). In panel (c) the electrode geometry produces a field that is perpendicular in direction to the dielectric surface making its effect minimal. For the case of a diagonally opposite pair of electrodes, as is the case in panel (c) the expected field is

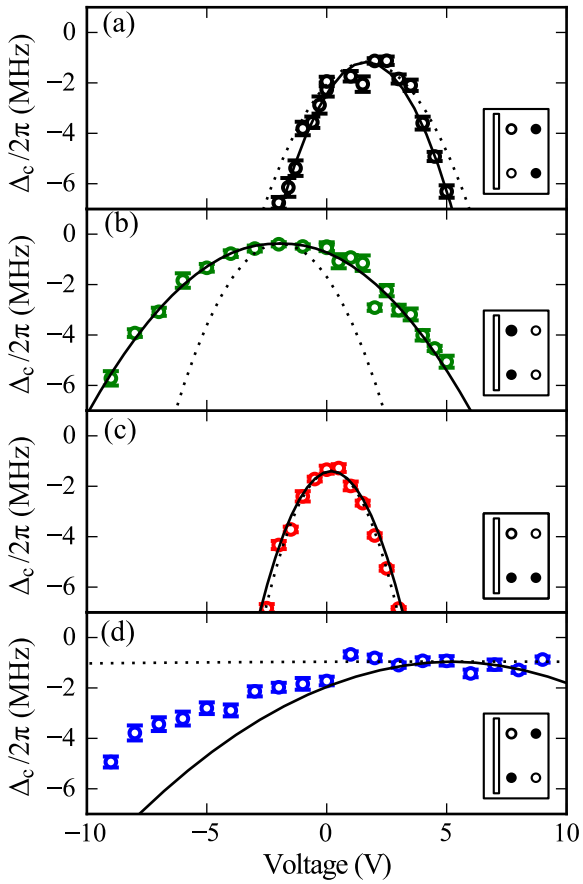

Figure 6.12: Comparison of measured Rydberg energy level shift with that corresponding to the calculated electric field. Each panel shows data for a different electrode geometry relative to the dielectric surface, where grounded electrodes are unfilled while those with an applied voltage are filled black. The dotted lines show the results of the calculated electric field when the dielectric surface is not included in the calculation. The solid lines show the case where the dielectric is included resulting in improved agreement to the data.

zero. With this electric field geometry the field experienced by the atoms is highly sensitive to their position relative to the electrodes. This accounts for the larger discrepancy between measured Rydberg energy level shift and that calculated in panel (d). These results highlight the large effect of the dielectric on the electric field produced at the position of the atoms. This is most apparent where the live electrodes are in close proximity to the dielectric and in this case the electric field is seen to be reduced to 50% of that expected without the dielectric. For the best fit the electric field in the dielectric is reduced by a factor $\epsilon_{\mathrm{r}} = 1.6$. This value is less than the low frequency permittivity of silica glass, 3.81 [143], suggesting that surface charges play an additional role in determining the field.

6.3 Outlook and summary

The work in this chapter demonstrates a method of performing electrometry near a dielectric surface by measurement of Rydberg energy levels shift using electromagnetically induced transparency. At a modest principle quantum number of $n = 46$ a sensitivity to background electric fields of ~ 10 mV/cm is observed. For Rydberg states of increasing principal quantum number the scaling of the polarisability gives this method unparalleled sensitivity. Using Rydberg states up to $n = 150$ background fields of 20 μm/cm have been measured [59]. The success of this technique in readily detecting electric fields may find application in precision measurements of surface adsorbates and dielectric properties. It is of general importance for experiments that make use of Rydberg atoms located near dielectric surfaces, such as short focal length lenses within vacuum chambers [36, 37], where surface interactions must be minimised.

In conclusion, this chapter has detailed the techniques required to measure Rydberg EIT in an ultracold sample of atoms. Atoms released from the MOT are interrogated with a probe beam whilst also illuminated by an intense Rydberg coupling beam. By detecting the probe beam on a photodiode an EIT spectrum has been measured; the presence of the coupling beam is then manifest as a narrow transparency window in the transmission spectrum of the probe.

The EIT spectrum data are fit in order to measure any shift in the Rydberg state caused by the application of an electric field. The large polarisability of the Rydberg state gives this method excellent sensitivity and the non-destructive nature of the EIT method provides a high experimental repetition rate. The design of the vacuum chamber in which the experiment is carried out incorporates a dielectric material near the position of the ultracold sample of atoms. The effect of this bulk material and surface adsorbates on the electric field are measured by the electrometry. An electric field attributed to the presence of adsorbates is measured when the electric fields are applied to the sample over a long time scale. This effect can be eliminated by apply electric fields transiently, allowing the expected quadratic relationship between Rydberg level shift and electric field to be recovered. Finally, the measured Rydberg energy level shift is compared to that calculated by numerically evaluating the field within the vacuum chamber. The resulting comparison between theory and experiment is only good where the dielectric is included. This experiment therefore highlights the strong effect of the dielectric and adsorbates on the Rydberg states of nearby atoms.

Chapter 7

Outlook and conclusion

7.1 Outlook

The experimental setup presented in this thesis offers great flexibility and several future directions of the project are possible. In terms of the coherent ground state excitation, the initial work towards Raman transfer presented within this thesis suggests that extensive work is required to achieve significant results. The low fidelity of the Raman transfer achieved can be attributed to the impurity of the initial state produced by the optical pumping. This leads to many possible Raman transfer paths and the Rabi oscillation signal becoming 'washed' out. Work to rectify these drawbacks has begun; the experimental setup has been adapted to give the possibility of a magnetic trap. The coils used to generate the MOT magnetic field gradient have been replaced with water cooled coils that can be run with a greatly increased current. This allows the magnetic field gradient to be increased, which not only improves the performance of the MOT, but also allows the setup of a magnetic trap. In this way a single magnetic spin state may be levitated in the trap, and along with improved optical pumping, a sample of atoms with a highly pure initial state may be obtained.

If this is modification is found to be unsuccessful in producing high fidelity Raman transfer, further adaptations will be required. The possibility of increasing the detuning of the Raman beams from resonance would have to be explored. This will have other consequences for the experiment, as discussed

in Sec. 4.2.1 of Chapter 4, in particular requiring a greater Rydberg coupling Rabi frequency so that the Raman transfer may still be suppressed. Although this could require a major rebuild of the experiment, the results of similar Rydberg quantum information processing experiments have shown that there is much interest in this field. In particular the success of the recent results on two atom systems [36, 37] has highlighted the impact of QIP using Rydberg atoms and motivates the on-going work on the experiment presented within this thesis.

The work relating to coherent excitation to Rydberg states successfully demonstrated a method of performing electrometry; an obvious extension to this work would be to perform spectroscopy on states of greater principle quantum number to improve the sensitivity. Although excitation to higher states is possible using the present setup, in order to maintain good signal to noise in the EIT spectra, higher Rydberg coupling Rabi frequencies may be required. The experiment could also be extended to measure the spatial variation of electric fields by moving the position of the test sample of atoms. In this way the profile of the electric fields near to various materials and adsorbates could be measured in a similar way to Ref. [58] and [64].

Excitation to Rydberg states of increasingly high principlal quantum number opens many possible long term directions for the experiment. It has been proposed that laboratory scale atomic physics experiments may provide a means to search for the existence of exotic particles beyond the standard model [144]. For example, the presence of hidden photons is expected to create detectable deviations from Coulomb's law. Although the Coulomb inverse square law has been extensively tested using closed conducting spheres several centimetres in size [145], the force at shorter distances is less well explored. The spectra of Rydberg atoms may provide a test of the Coulomb law at length scales of a few micrometres, a currently little investigated regime [146].

For the existing setup, with a two-photon Rydberg excitation scheme, the highest Rydberg state that can be coupled to is limited by the wavelength and laser power available at 480 nm. In previous work employing the same laser system as used throughout this thesis, Rydberg states of $n = 125$ have been observed in a vapour cell [61]. In order to couple to higher n Rydberg

states microwave transitions may be used. Using a similar setup to that presented here [74], work on a microwave dressing of Ryderg dark states has already been carried out with 46s and 45p states [147]. Using the apparatus developed in this thesis this work may be readily extended to other more highly excited states. Furthermore, proposals have also been made to exploit Rydberg atoms to investigate Anderson localisation [148] using microwave transitions between Rydberg states. In general, the study of highly excited Rydberg states offers many interesting possible directions for the experiment.

7.2 Summary and conclusion

In summary, this thesis represents the work carried out to develop an experiment to study excitation between ground and Rydberg states. The work is motivated by the application of Rydberg atoms to QIP [48] and precision electrometry [59]. The experimental setup is very flexible; it provides a source of ultracold atoms, phase stable Raman beams and two-photon Rydberg excitation. It may therefore be adapted to several possible future directions.

In order to create a pair of phase stable Raman beams the experiment was designed around a single 780 nm master laser that provides all light required for ground state excitation. Beams separated by the hyperfine ground state splitting in ^{87}Rb were generated using an EOM that creates sidebands on the light produced by the master laser. As these sidebands are only 1% of the intensity of the carrier a technique to spatially filter the beams was required so that they could be injected into slave lasers, thus providing adequate light for the entire experiment. This was achieved using a novel filtering technique employing the Faraday effect in a isotopically pure Rb vapour cell [92].

Once generated, the Raman beams were applied to a sample of ultracold atoms released from the dipole trap, the aim being to drive coherent population transfer between the two hyperfine ground states. Some evidence of Raman transfer was observed, with a visibility of approximately 20%. This was attributed to poor preparation of the initial state, a problem which can possibly be overcome by loading the atoms into a magnetic trap and opti-

mising the optical pumping.

To study excitation to Rydberg states a novel laser stabilisation technique that allows locking to non-ground state transitions has been developed. These transitions are much weaker than those originating from the ground state so that an alternative lock scheme is required. The method presented in this thesis generates a locking signal using cascade EIT in a vapour cell [121]. Excellent locking signals were demonstrating for moderate laser powers and substantially high n Rydberg states; for the 70S states a suitable locking signal was produced using only 13 mW of 480 nm light. This technique was successfully implemented not only for the work on Rydberg excitation in this thesis but in other similar experiments [39, 74].

With the two-photon excitation laser system in place, spectroscopy of the Rydberg state could be carried out in ultracold atoms by observing EIT. Atoms were released from the MOT and the probe beam scanned across resonance whilst the Rydberg coupling beam was on; EIT was then manifest as a transparency window in the transmission of the probe. By fitting this spectrum using a theoretical lineshape the detuning of the coupling beam from resonance with the Rydberg state could be found. As a shift in the Rydberg energy level is highly sensitive to the local electric field this system offers a suitable method of performing electrometry.

The shift in the Rydberg state was measured with various electric fields generated using voltages applied to electrodes within the vacuum chamber. When the voltages were applied continuously the resulting Stark map was found to have an unexpected asymmetric profile around zero local electric field. This affect was attributed to adsorbates bonded to a nearby dielectric surface, the front window of the vacuum chamber, generating an additional electric field. When a voltage was applied to the electrodes transiently, for time scales of 100 μs, the expected quadratic Stark effect could be recovered. The local electric field at the position of the MOT could then be calibrated and the background field was found to be 10 mV/cm.

Finally, the measured electric field was compared to a theoretical model of the field within the vacuum chamber calculated by numerically solving Laplace's equation. Where the live electrodes were near to the dielectric the measured

field was found to depart from the calculated value. In order to improve the model the dielectric was included in the calculation by reducing the potential within its boundary. Using this method good agreement to the data could be found with a dielectric constant $\epsilon_{\mathrm{r}} = 1.6$. This value is less than the low frequency permittivity of silica glass, 3.81, suggesting that surface charges play an additional role in determining the field. This method of electrometry has high sensitivity, especially for states of increasing n, and is important for experiments where Rydberg atoms are in close proximity to dielectric surfaces.

Appendix A

Electric field calculation

A.1 Numerical solution of Laplace's equation

In order to evaluate the electric field, for a given spatial distribution of electrical potential, solutions of Laplace's equation must be found:

$$\frac{\partial^2\phi(x,y)}{\partial x^2} + \frac{\partial^2\phi(x,y)}{\partial y^2} = 0, \tag{A.1}$$

where $\phi(x,y)$ is the electrical potential at a position (x,y). Numerically solutions of Laplace's equation are discussed in Ref. [149] and the references found therein. To carry out the calculation one discretises the two-dimensional space into a grid where a point (x,y) is separated from its neighbours by a distance a as shown in Fig. A.1. The Taylor expansion

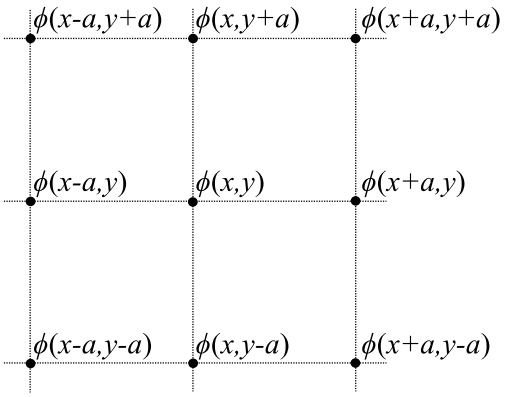

Figure A.1: Electrical potential ϕ over a grid with points spaced by a.

can then be used to obtain an expression linking the value of ϕ with its value at the surrounding grid points. The Taylor expansion of a function of two variables, $f(u,v)$ about the point (u_0,v_0) is given by:

$$f(u,v)=\sum_{n=0}^{\infty}\left[\frac{1}{n!}\sum_{k=0}^{n}\binom{n}{k}\frac{\partial^n f(u_0,v_0)}{\partial u^{n-k}\partial v^k}(u-u_0)^{n-k}(v-v_0)^k\right], \tag{A.2}$$

with:

$$\binom{n}{k}=\frac{n!}{k!(n-k)!}. \tag{A.3}$$

For a function of a single variable this reduces to:

$$f(u)=\sum_{n=0}^{\infty}\frac{1}{n!}\frac{\partial^n f(u_0)}{\partial u^n}(u-u_0)^n. \tag{A.4}$$

The value of ϕ at each of the surrounding grid points can now be Taylor expanded about the central point $\phi(x,y)$. For functions of only one variable, expanding $\phi(x+a,y)$ around $\phi(x,y)$ for example, Eq. (A.4) is used. The required Taylor expansion is found by replacing $f(u)$ with $\phi(x+a)$ and u_0 with x in Eq. (A.4). For functions of two variables, *i.e.* expanding $\phi(x+a,y+a)$ around $\phi(x,y)$, the Taylor expansion in (A.2) must be used. The Taylor expansion for each point in the grid shown in Fig. A.1 is then:

$$\begin{aligned}
\phi(x\pm a,y) &= \phi(x,y)\pm\phi_x(x,y)a+\frac{1}{2}\phi_{xx}(x,y)a^2\pm\frac{1}{6}\phi_{xxx}(x,y)+O(a^4),\\
\phi(x,y\pm a) &= \phi(x,y)\pm\phi_y(x,y)a+\frac{1}{2}\phi_{yy}(x,y)a^2\pm\frac{1}{6}\phi_{yyy}(x,y)+O(a^4),\\
\phi(x\pm a,y\pm a) &= \phi(x,y)\pm\phi_x(x,y)a\pm\phi_y(x,y)a\\
&\quad+\frac{1}{2}\{\phi_{xx}(x,y)a^2\pm 2\phi_{xy}(x,y)a^2+\phi_{yy}(x,y)a^2\}\\
&\quad+\frac{1}{6}\{\pm\phi_{xxx}(x,y)\pm 3\phi_{xxy}(x,y)a^3\\
&\quad\pm\phi_{xyy}(x,y)a^3\pm\phi_{yyy}(x,y)a^3\}+O(a^4),
\end{aligned} \tag{A.5}$$

where the subscripts denote the partial derivative with respect to those variables. In the last of these expressions all combinations of + and − signs must

be included. Finding the sum, S, of these expressions and collecting terms of equal orders of a gives:

$$\begin{aligned} S &= [\phi(x \pm a, y) + \phi(x, y \pm a) + \phi(x \pm a, y \pm a) + \phi(x \pm a, y \mp a)], \\ &= 8\phi(x, y) \\ &+ 3\phi_x(x, y)a - 3\phi_x(x, y)a + 3\phi_y(x, y)a - 3\phi_y(x, y)a \\ &+ 3\phi_{xx}(x, y)a^2 + 3\phi_{yy}(x, y)a^2 + 2\phi_{xy}(x, y)a^2 - 2\phi_{xy}(x, y)a^2 \\ &+ 2\phi_{xxx}(x, y)a^3 - 2\phi_{xxx}(x, y)a^3 + 2\phi_{yyy}(x, y)a^3 - 2\phi_{yyy}(x, y)a^3 \\ &+ \phi_{xxy}(x, y)a^3 - \phi_{xxy}(x, y)a^3 + \phi_{xyy}(x, y)a^3 - \phi_{xyy}(x, y)a^3 \\ &+ O(a^4). \end{aligned} \tag{A.6}$$

With the fourth order terms, $O(a^4)$, omitted and noting that the third order terms in a cancel, this reduces to:

$$S = 8\phi(x, y) + 3a^2\{\phi_{xx}(x, y) + \phi_{yy}(x, y)\}, \tag{A.7}$$

In order to satisfy Laplace's equation the term $\{\phi_{xx}(x, y) + \phi_{yy}(x, y)\}$ must be zero giving:

$$\begin{aligned} \phi(x, y) &= \frac{1}{8}[\phi(x \pm a, y)\phi(x, y \pm a) \\ &+ \phi(x \pm a, y \pm a) + \phi(x \pm a, y \mp a)]. \end{aligned} \tag{A.8}$$

Laplace's equation can therefore be solved if the potential at each point in space is made equal to the average of the points surrounding it. This can be done numerically by setting an initially known distribution of potential and iteratively setting each point to be equal to the average of the potential at the surrounding eight points. If at the start of each iteration the initial potential is reset then the system will converge to a distribution of potential that satisfies Laplace's equation. Once the potential is calculated the electric field is found using the relation:

$$E = -\nabla\phi(x, y) \tag{A.9}$$

A.2 Example calculation

To illustrate the method described in the previous section the electric field produced between a pair of parallel plates with an applied potential is calculated. The geometry of the system is shown in Fig. A.2(a): a pair of plates 2 mm thick are positioned 13 mm apart from one another. The plate coloured red in Fig. A.2(a) is fixed at a potential of 10 V and the blue coloured plate is at 0 V. The calculation is carried out using a grid of 200 × 200 points to ensure good resolution. The iteration process described in the previous expression is then carried out to find the potential at all points in the grid. The electric field components at each point are then calculated by finding the gradient along the direction of the z and x axes. The magnitude of the electric field may then be found by adding the field components in quadra-

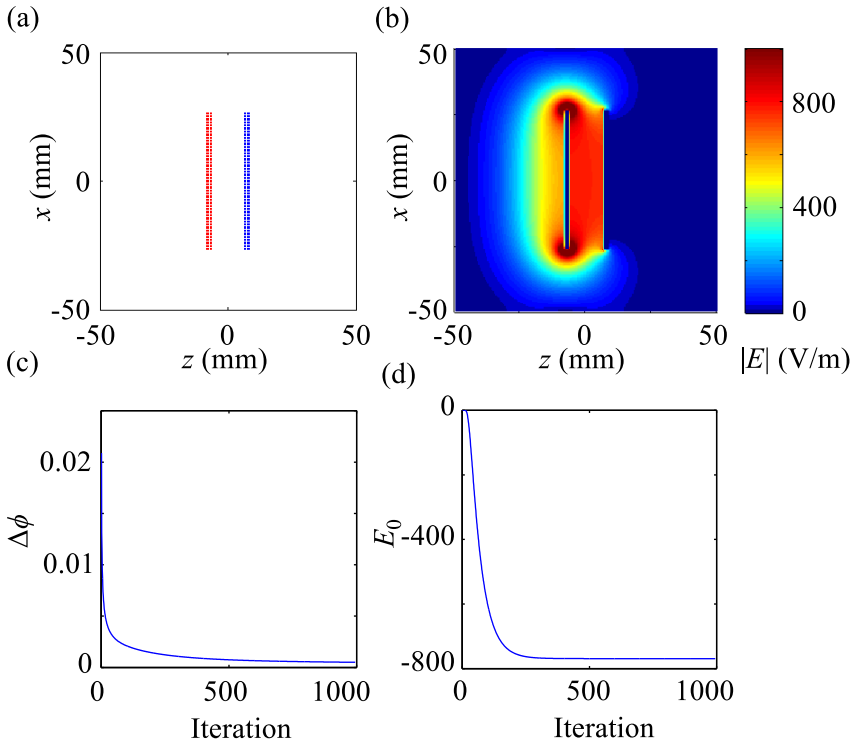

Figure A.2: Example calculation of the electric field between two parallel plates of potential. The geometry of the plates in shown in (a) where the red dots are a potential of 10 V and the blue dots are 0 V. The calculated electric field magnitude is then shown in (b). Parts (c) and (d) show the convergence of the average potential and central electric field value, respectively.

ture, the result of which is shown in Fig. A.2(b). The calculated electric field is constant between the plates and decays to zero outside this region.

In Fig. A.2(c) and (d) the convergence of the potential and electric field is demonstrated. In Fig. A.2(c) the difference in potential between iteration steps, averaged over the entire grid, is shown as a function of iteration number. The change in potential rapidly falls with increasing iteration step and tends towards a zero value where it is consistent with the solution of Laplace's equation. The iteration process is stopped when the change in potential between steps reaches a predefined minimum. The evolution of the electric field magnitude at the centre of the grid is shown in Fig. A.2(d). At the beginning of the iteration process the potential has not been propagated throughout the grid so the electric field is zero. As the process continues the electric field converges towards a steady value along with the potential.

The shape of the potential and electric field components is shown in more detail in Fig. A.3 and Fig. A.4. In Fig. A.3 slices through the potential and components of the electric field along the line where $x = 0$ are shown. The potential is observed to be 10 V and 0 V at the position of the plates, which are indicated by the vertical red lines, with a linear variation between these values. The electric field component in the x direction along $x = 0$ is zero. This is expected as there should be no electric field component parallel to the surface if the plates. The electric field component in the z direction is the gradient of the potential in Fig. A.3(a); it has a constant value between the plates and falls to zero outside of this region. The magnitude of the electric

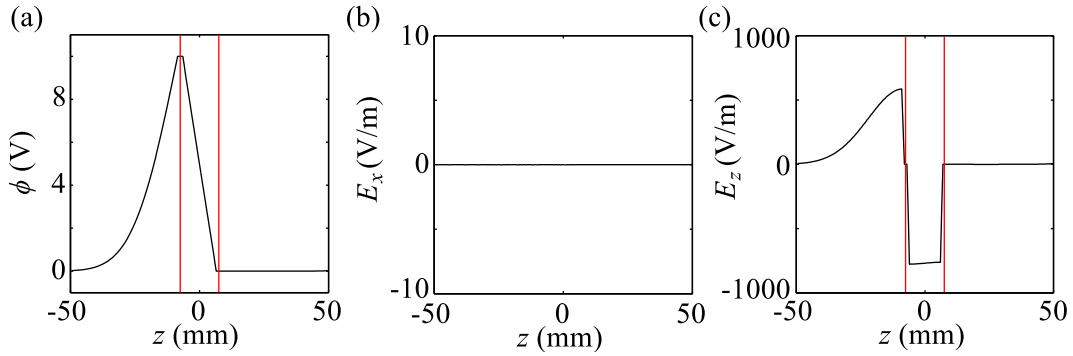

Figure A.3: Slices through the potential and electric field along the line $x = 0$ as a function of the position in the z direction.

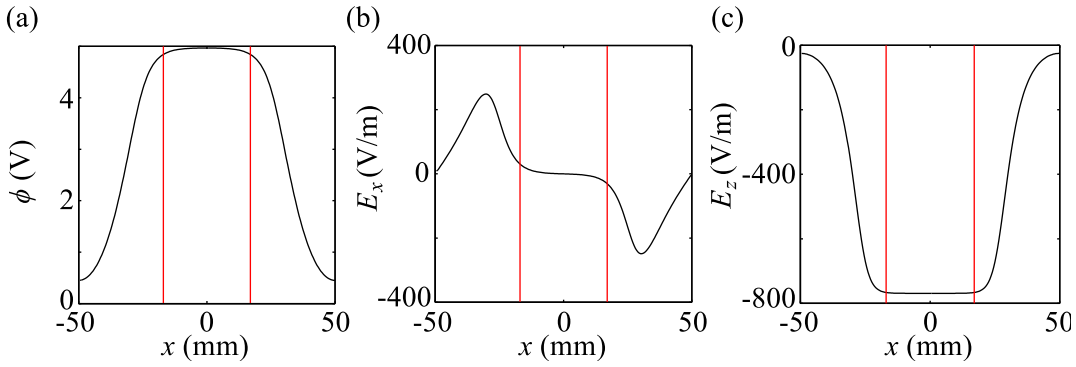

Figure A.4: Slices through the potential and electric field along the line $z = 0$ as a function of the position in the x direction.

field between plates in found to be 770 V/m.

Fig. A.4 shows a slice through the calculated potential and electric field, but along the line where $z = 0$. In Fig. A.4(a) the potential has a constant value between the plates and falls to zero away from this region. The electric field component in the x direction, shown in Fig. A.4(b), is also zero between the plates but a field exists at the end of the plates where the potential is changing. Finally in Fig. A.4(c) the electric field between the plates in the z direction is constant and falls to zero outside of this region.

These results are consistent with the well known result of the electric field between a pair a parallel capacitor plates. The field is constant between the plates and given by the simple relation: $E = d/V$ where d is the separation of the plates and V is the change in potential across them. With the plates 13 mm apart with a voltage difference of 10 V across them the field generated is 769.23 V/m. This is in excellent agreement with the value calculated by solving Laplace's equation. The slight variation of the calculated field between the plates is due to finite size effects.

Appendix B

Detailed optics setup

A detailed diagram of the optics used throughout the work presented in this thesis is shown on the following page in Fig. B.2. A key for the diagram is given below in Fig. B.1.

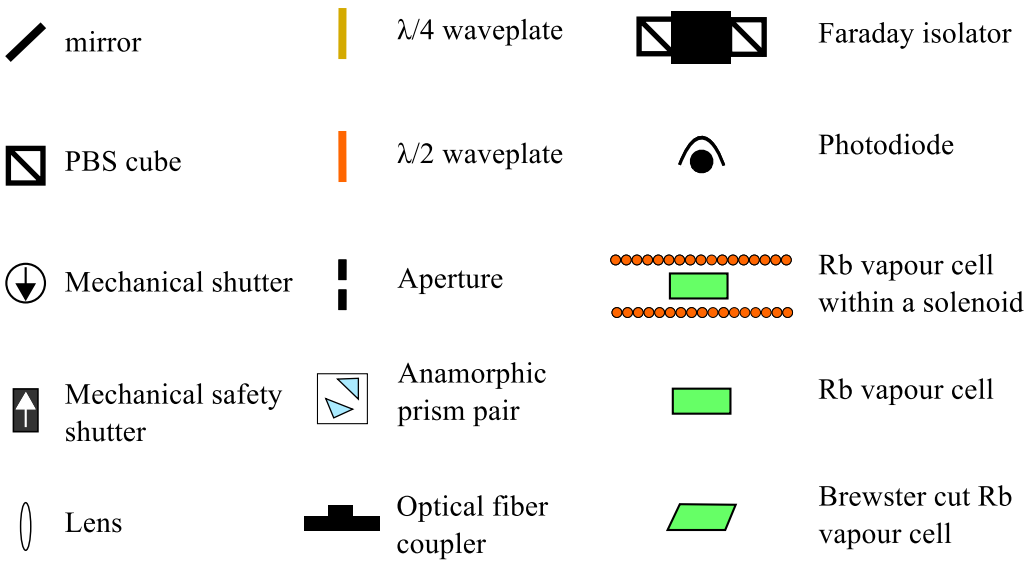

Figure B.1: Optical setup diagram key.

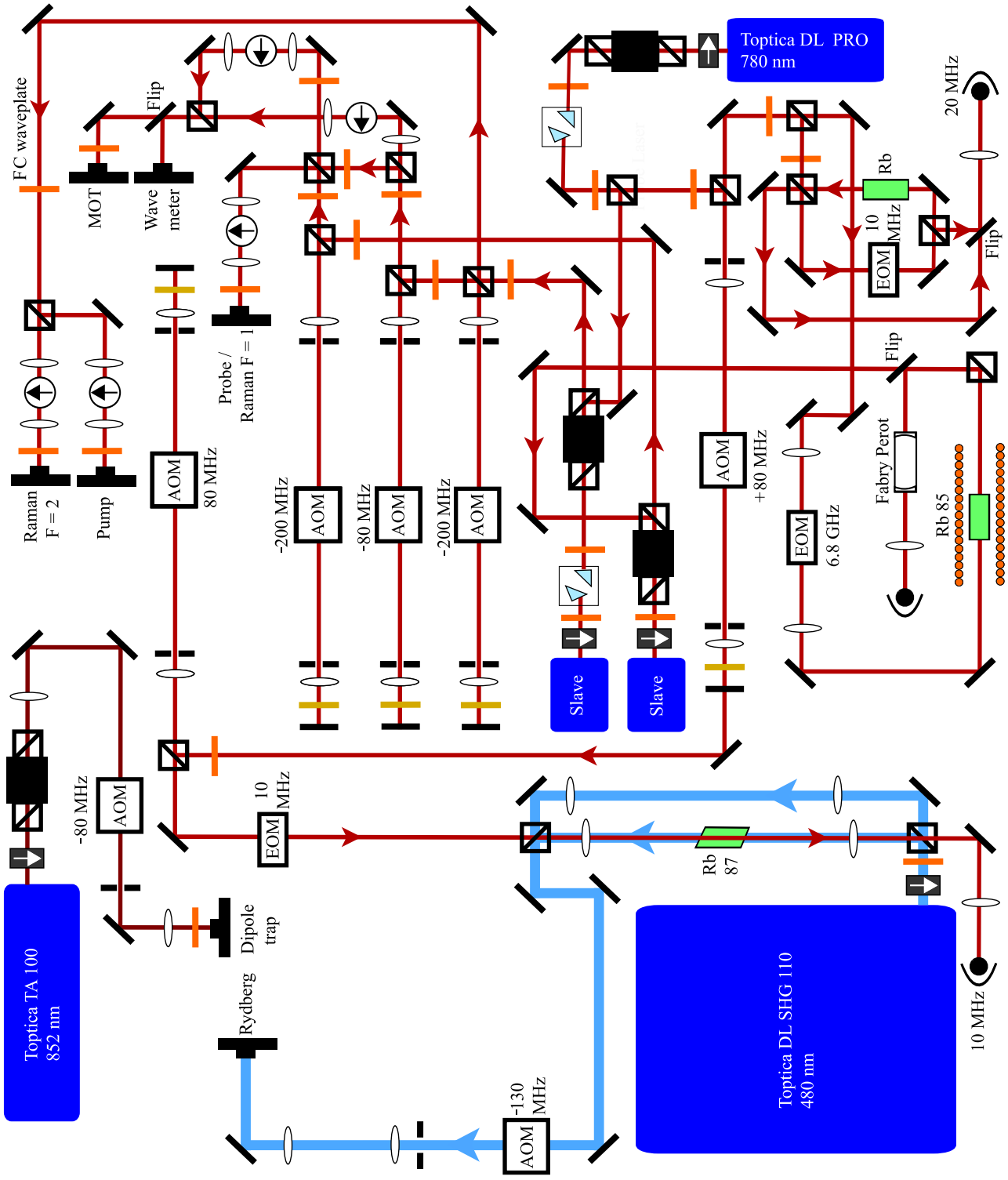

Figure B.2: Schematic optical setup.

Bibliography

[1] T. H. Maiman, *Stimulated optical radiation in ruby*, Nature **187**, 493–494 (08 1960).

[2] L. Allen and J. H. Eberly, *Optical resonance and two-level atoms* (Dover, 1987).

[3] H. M. Gibbs, *Incoherent resonance fluorescence from a Rb atomic beam excited by a short coherent optical pulse*, Phys. Rev. A **8**, 446 (1973).

[4] S. E. Harris, *Electromagnetically induced transparency*, Physics Today **50**, 36 (1997).

[5] M. Fleischhauer, A. Imamoglu, and J. P. Marangos, *Electromagnetically induced transparency: Optics in coherent media*, Rev. Mod. Phys. **77**, 633 (2005).

[6] K.-J. Boller, A. Imamoglu, and S. E. Harris, *Observation of electromagnetically induced transparency*, Phys. Rev. Lett. **66**, 2593 (1991).

[7] J. Dalibard and C. Cohen-Tannoudji, *Dressed-atom approach to atomic motion in laser light: the dipole force revisited*, J. Opt. Soc. Am. B **2**, 1707 (1985).

[8] U. Fano, *Effects of configuration interaction on intensities and phase shifts*, Phys. Rev. **124**, 1866 (1961).

[9] L. V. Hau, S. E. Harris, Z. Dutton, and C. H. Behroozi, *Light speed reduction to 17 metres per second in an ultracold atomic gas*, Nature **397**, 594 (02 1999).

[10] E. Arimondo, *Coherent population trapping in laser spectroscopy*, Prog. Opt. **35**, 257 (1996).

[11] A. Aspect *et al.*, *Laser cooling below the one-photon recoil energy by velocity-selective coherent population trapping*, Phys. Rev. Lett. **61**, 826 (1988).

[12] K. Bergmann, H. Theuer, and B. W. Shore, *Coherent population transfer among quantum states of atoms and molecules*, Rev. Mod. Phys. **70**, 1003 (1998).

[13] J. R. Rydberg, *On the structure of the line-spectra of the chemical elements*, Phil. Mag., 5th ser., **29**, 331 (1890).

[14] T. F. Gallagher, *Rydberg Atoms* (Cambridge University Press, 1994).

[15] M. A. Nielsen and I. L. Chuang, *Quantum computation and quantum information* (Cambridge University Press, 2000).

[16] D. Jaksch *et al.*, *Fast quantum gates for neutral atoms*, Phys. Rev. Lett. **85**, 2208 (2000).

[17] M. D. Lukin *et al.*, *Dipole blockade and quantum information processing in mesoscopic atomic ensembles*, Phys. Rev. Lett. **87**, 037901 (2001).

[18] R. G. Unanyan and M. Fleischhauer, *Efficient and robust entanglement generation in a many-particle system with resonant dipole-dipole interactions*, Phys. Rev. A **66**, 032109 (2002).

[19] D. Møller, L. B. Madsen, and K. Mølmer, *Quantum gates and multiparticle entanglement by Rydberg excitation blockade and adiabatic passage*, Phys. Rev. Lett. **100**, 170504 (2008).

[20] M. Müller *et al.*, *Mesoscopic Rydberg gate based on electromagnetically induced transparency*, Phys. Rev. lett. **102**, 170502 (2009).

[21] M. Saffman and K. Mølmer, *Efficient multiparticle entanglement via asymmetric Rydberg blockade*, Phys. Rev. Lett. **102**, 240502 (2009).

[22] H. Weimer *et al.*, *A Rydberg quantum simulator*, Nat Phys **6**, 382 (05 2010).

[23] M. Saffman and T. G. Walker, *Creating single-atom and single-photon sources from entangled atomic ensembles*, Phys. Rev. A **66**, 065403 (2002).

[24] A. S. Sørensen, C. H. van der Wal, L. I. Childress, and M. D. Lukin, *Capacitive coupling of atomic systems to mesoscopic conductors*, Phys. Rev. Lett. **92**, 063601 (2004).

[25] D. Petrosyan and M. Fleischhauer, *Quantum information processing with single photons and atomic ensembles in microwave coplanar waveguide resonators*, Phys. Rev. Lett. **100**, 170501 (2008).

[26] T. F. Gallagher *et al.*, *Resonant Rydberg-atom — Rydberg-atom collisions*, Phys. Rev. A **25**, 1905 (1982).

[27] J. M. Raimond, G Vitrant, and S Haroche, *Spectral line broadening due to the interaction between very excited atoms: 'the dense Rydberg gas'*, J. Phys. B **14**, L655 (1981).

[28] Chu S., *Laser manipulation of atoms and particles*, Science **253**, 861 (1991).

[29] K. Singer *et al.*, *Suppression of excitation and spectral broadening induced by interactions in a cold gas of Rydberg atoms*, Phys. Rev. Lett. **93**, 163001 (2004).

[30] D. Tong *et al.*, *Local blockade of Rydberg excitation in an ultracold gas*, Phys. Rev. Lett. **93**, 063001 (2004).

[31] T. C. Liebisch, A. Reinhard, P. R. Berman, and G. Raithel, *Atom counting statistics in ensembles of interacting Rydberg atoms*, Phys. Rev. Lett. **95**, 253002 (2005).

[32] R. Heidemann *et al.*, *Evidence for coherent collective Rydberg excitation in the strong blockade regime*, Phys. Rev. Lett. **99**, 163601 (2007).

[33] U. Raitzsch *et al.*, *Echo experiments in a strongly interacting Rydberg gas*, Phys. Rev. Lett. **100**, 013002 (2008).

[34] A. Gaëtan *et al.*, *Observation of collective excitation of two individual atoms in the Rydberg blockade regime*, Nat Phys **5**, 115 (2009).

[35] E. Urban *et al.*, *Observation of Rydberg blockade between two atoms*, Nat Phys **5**, 110 (2009).

[36] L. Isenhower *et al.*, *Demonstration of a neutral atom controlled-NOT quantum gate*, Phys. Rev. Lett. **104**, 010503 (2010).

[37] T. Wilk *et al.*, *Entanglement of two individual neutral atoms using Rydberg blockade*, Phys. Rev. Lett. **104**, 010502 (2010).

[38] J. O. Day, E. Brekke, and T. G. Walker, *Dynamics of low-density ultracold Rydberg gases*, Phys. Rev. A **77**, 052712 (2008).

[39] J. D. Pritchard *et al.*, *Cooperative atom-light interaction in a blockaded Rydberg ensemble*, Phys. Rev. Lett. **105**, 193603 (2010).

[40] E. Brekke, J. O. Day, and T. G. Walker, *Four-wave mixing in ultracold atoms using intermediate Rydberg states*, Phys. Rev. A **78**, 063830 (2008).

[41] A. K. Mohapatra *et al.*, *A giant electro-optic effect using polarizable dark states*, Nat Phys **4**, 890 (11 2008).

[42] V. Bendkowsky *et al.*, *Observation of ultralong-range Rydberg molecules*, Nature **458**, 1005–1008 (04 2009).

[43] K. R. Overstreet *et al.*, *Observation of electric-field-induced Cs Rydberg atom macrodimers*, Nat Phys **5**, 581 (08 2009).

[44] A. Speck, C. H. Storry, E.A. Hessels, and G. Gabrielse, *Laser-controlled production of Rydberg positronium via charge exchange collision*, Phys. Lett B **597**, 257 (2004).

[45] J.-H. Choi *et al.*, *Magnetic trapping of long-lived cold Rydberg atoms*, Phys. Rev. Lett. **95**, 243001 (2005).

[46] J. Millen, G. Lochead, and M. P. A. Jones, *Two-electron excitation of an interacting cold Rydberg gas*, Phys. Rev. Lett. **105**, 213004 (2010).

[47] T. C. Killian *et al.*, *Ultracold neutral plasmas: recent experiments and new prospects*, J. Phys. A. **36**, 6077 (2003).

[48] M. Saffman, T. G. Walker, and K. Mølmer, *Quantum information with Rydberg atoms*, Rev. Mod. Phys. **82**, 2313 (2010).

[49] D. D. Yavuz *et al.*, *Fast ground state manipulation of neutral atoms in microscopic optical traps*, Phys. Rev. Lett. **96**, 063001 (2006).

[50] T. A. Johnson *et al.*, *Rabi oscillations between ground and Rydberg states with dipole-dipole atomic interactions*, Phys. Rev. Lett. **100**, 113003 (2008).

[51] N. Schlosser, G. Reymond, I. Protsenko, and P. Grangier, *Sub-poissonian loading of single atoms in a microscopic dipole trap*, Nature **411**, 1024 (2001).

[52] J. Neukammer *et al.*, *Spectroscopy of Rydberg atoms at* $n \approx 500$*: Observation of quasi-Landau resonances in low magnetic fields*, Phys. Rev. Lett. **59**, 2947 (1987).

[53] M. T. Frey *et al.*, *Use of the Stark effect to minimize residual electric fields in an experimental volume*, Review of Scientific Instruments **64**, 3649 (1993).

[54] A. Schramm *et al.*, *Laser photoelectron attachment to molecules in a skimmed supersonic beam: Diagnostics of weak electric fields and attachment cross sections down to* 20 μeV, Phys. Rev. Lett. **81**, 778 (1998).

[55] M. H. Anderson *et al.*, *Observation of Bose-Einstein condensation in a dilute atomic vapor*, Science **269**, 198 (1995).

[56] K. B. Davis *et al.*, *Bose-Einstein condensation in a gas of sodium atoms*, Phys. Rev. Lett. **75**, 3969 (1995).

[57] J. M. McGuirk, D. M. Harber, J. M. Obrecht, and E. A. Cornell, *Alkali-metal adsorbate polarization on conducting and insulating surfaces probed with Bose-Einstein condensates*, Phys. Rev. A **69**, 062905 (2004).

[58] J. M. Obrecht, R. J. Wild, and E. A. Cornell, *Measuring electric fields from surface contaminants with neutral atoms*, Phys. Rev. A **75**, 062903 (2007).

[59] A. Osterwalder and F. Merkt, *Using high Rydberg states as electric field sensors*, Phys. Rev. Lett. **82**, 1831 (1999).

[60] M. G. Bason, A. K. Mohapatra, K. J. Weatherill, and C. S. Adams, *Electro-optic control of atom-light interactions using Rydberg dark state polaritons*, Phys. Rev. A **77**, 032305 (2008).

[61] A. K. Mohapatra, T. R. Jackson, and C. S. Adams, *Coherent optical detection of highly excited Rydberg states using electromagnetically induced transparency*, Phys. Rev. Lett. **98**, 113003 (2007).

[62] J. D. Carter and J. D. D. Martin, *Energy shifts of Rydberg atoms due to patch fields near metal surfaces*, Phys. Rev. A **83**, 032902 (2011).

[63] D. D. Neufeld, Y. Pu, and F.B. Dunning, *Probing stray surface electric patch fields using Rydberg atoms*, Nucl. Instr. and Meth. B **In Press, Corrected Proof**, – (2010).

[64] A. Tauschinsky *et al.*, *Spatially resolved excitation of Rydberg atoms and surface effects on an atom chipydberg atoms and surface effects on an atom chip*, Phys. Rev. A **81**, 063411 (2010).

[65] M. Viteau *et al.*, *Rydberg spectroscopy of a Rb MOT in the presence of applied or ion created electric fields*, Opt. Express **19**, 6007 (2011).

[66] C. Monroe *et al.*, *Demonstration of a fundamental quantum logic gate*, Phys. Rev. Lett. **75**, 4714 (1995).

[67] Z. Kis and F. Renzoni, *Qubit rotation by stimulated Raman adiabatic passage*, Phys. Rev. A **65**, 032318 (2002).

[68] P. S. Jessen and I.H. Deutsch, *Optical lattices* (Academic Press, 1996) p. 95.

[69] Y. Miroshnychenko *et al.*, *Quantum engineering: An atom-sorting machine*, Nature **442**, 151 (07 2006).

[70] W. S. Bakr *et al.*, *A quantum gas microscope for detecting single atoms in a Hubbard-regime optical lattice*, Nature **462**, 74 (2009).

[71] R. Löw *et al.*, *Apparatus for excitation and detection of Rydberg atoms in quantum gases*, arXiv:0706.2639v1.

[72] M. G. Bason, A. K. Mohapatra, K. J. Weatherill, and C. S. Adams, *Narrow absorptive resonances in a four-level atomic system*, J. Phys. B **42**, 075503 (2009).

[73] M. G. Bason *et al.*, *Enhanced electric field sensitivity of rf-dressed Rydberg dark states*, New Journal of Physics **12**, 065015 (2010).

[74] K. J. Weatherill *et al.*, *Electromagnetically induced transparency of an interacting cold Rydberg ensemble*, J. Phys. B **41**, 201002 (2008).

[75] K. J. Weatherill *et al.*, *A versatile and reliably reusable ultrahigh vacuum viewport*, Rev. Sci. Instrum. **80**, 026105 (2009).

[76] Steven Chu, *Nobel lecture: The manipulation of neutral particles*, Rev. Mod. Phys. **70**, 685 (1998).

[77] C. N. Cohen-Tannoudji, *Nobel lecture: Manipulating atoms with photons*, Rev. Mod. Phys. **70**, 707 (1998).

[78] W. D. Phillips, *Nobel lecture: Laser cooling and trapping of neutral atoms*, Rev. Mod. Phys. **70**, 721 (1998).

[79] C. J. Foot, *Atomic Physics* (Oxford Univeristy Press, 2005).

[80] S. Chu *et al.*, *Three-dimensional viscous confinement and cooling of atoms by resonance radiation pressure*, Phys. Rev. Lett. **55**, 48 (Jul 1985).

[81] E. L. Raab *et al.*, *Trapping of neutral sodium atoms with radiation pressure*, Phys. Rev. Lett. **59**, 2631 (1987).

[82] D. A. Steck, *Rubidium 87 D line data*, `http://steck.us/alkalidata/rubidium87numbers.pdf`.

[83] P. D. Lett *et al.*, *Optical molasses*, J. Opt. Soc. Am. B **6**, 2084 (1989).

[84] P. D. Lett *et al.*, *Observation of atoms laser cooled below the Doppler limit*, Phys. Rev. Lett. **61**, 169 (1988).

[85] J. Dalibard and C. Cohen-Tannoudji, *Laser cooling below the Doppler limit by polarization gradients: simple theoretical models*, J. Opt. Soc. Am. B **6**, 2023 (Nov 1989).

[86] P. J. Ungar, D. S. Weiss, E. Riis, and S. Chu, *Optical molasses and multilevel atoms: theory*, J. Opt. Soc. Am. B **6**, 2058 (1989).

[87] R. Grimm, M. Weidemüller, and Y. B. Ovchinnikov, *Optical dipole traps for neutral atoms*, Adv. At., Mol., Opt. Phys **42**, 95 (2000).

[88] S. Chu, J. E. Bjorkholm, A. Ashkin, and A. Cable, *Experimental observation of optically trapped atoms*, Phys. Rev. Lett. **57**, 314 (1986).

[89] S. J. M. Kuppens *et al.*, *Loading an optical dipole trap*, Phys. Rev. A **62**, 013406 (2000).

[90] C. J. Myatt *et al.*, *Production of two overlapping Bose-Einstein condensates by sympathetic cooling*, Phys. Rev. Lett. **78**, 586 (1997).

[91] D.L. Jenkin *et al.*, *Bose-Einstein condensation of 87Rb in a levitated crossed dipole trap*, Eur. Phys. J. D(2011).

[92] R. P. Abel *et al.*, *Faraday dichroic beam splitter for Raman light using an isotopically pure alkali-metal-vapor cell*, Opt. Lett. **34**, 3071–3073 (2009).

[93] M. Kasevich and S. Chu, *Atomic interferometry using stimulated Raman transitions*, Phys. Rev. Lett. **67**, 181–184 (1991).

[94] S. Manz, T. Fernholz, J. Schmiedmayer, and J.-W. Pan, *Collisional decoherence during writing and reading quantum states*, Phys. Rev. A **75**, 040101 (2007).

[95] J. Bateman, A. Xuereb, and T. Freegarde, *Stimulated Raman transitions via multiple atomic levels*, Phys. Rev. A **81**, 043808 (2010).

[96] P. Bouyer, T. L. Gustavson, K. G. Haritos, and M. A. Kasevich, *Microwave signal generation with optical injection locking*, Opt. Lett. **21**, 1502–1504 (1996).

[97] M. P. A. Jones *et al.*, *Controlled photon emission and Raman transition experiments with a single trapped atom* (Proc. 17th Conf. on Laser Spectroscopy, 2005).

[98] J. E. Bateman *et al.*, *Hänsch–Couillaud locking of Mach–Zehnder interferometer for carrier removal from a phase-modulated optical spectrum*, J. Opt. Soc. Am. B **27**, 1530 (Aug 2010).

[99] D Haubrich, M Dornseifer, and R Wynands, *Lossless beam combiners for nearly equal laser frequencies*, Rev. Sci. Instrum. **71**, 338 (2000).

[100] M. Faraday, *Experimental researches in electricity*, Phil. Trans. Royal Soc **136**, 1 (1846).

[101] Y. Öhman, *Solar flares observed at the Swedish astrophysical station in Anacapri in the year 1955*, Stockholm Observ. Ann. **19**, 3 (1956).

[102] J. Menders *et al.*, *Ultranarrow line filtering using a Cs Faraday filter at 852 nm*, Opt. Lett. **16**, 846–848 (1991).

[103] D. J. Dick and T. M. Shay, *Ultrahigh-noise rejection optical filter*, Opt. Lett. **16**, 867–869 (1991).

[104] T. Junxiong *et al.*, *Experimental study of a model digital space optical communication system with new quantum devices*, Appl. Opt. **34**, 2619–2622 (1995).

[105] A. Popescu, K. Schorstein, and T. Walther, *A novel approach to a Brillouin–LIDAR for remote sensing of the ocean temperature*, Appl. Phy. B **79**, 955 (2004).

[106] H. Chen, C. Y. She, Paul Searcy, and Eric Korevaar, *Sodium-vapor dispersive Faraday filter*, Opt. Lett. **18**, 1019–1021 (1993).

[107] S. K. Gayen *et al.*, *Induced-dichroism-excited atomic line filter at 532 nm*, Opt. Lett. **20**, 1427–1429 (1995).

[108] A. Cerè *et al.*, *Narrowband tunable filter based on velocity-selective optical pumping in an atomic vapor*, Opt. Lett. **34**, 1012–1014 (2009).

[109] C. S. Gardner, *Performance capabilities of middle-atmosphere temperature lidars: comparison of Na, Fe, K, Ca, and Rayleigh systems*, Appl. Opt. **43**, 4941 (2004).

[110] A. B. Villaverde, D. A. Donatti, and D. G. Bozinis, *Terbium gallium garnet Verdet constant measurements with pulsed magnetic field*, J. Phys. C. **11**, 495 (1978).

[111] P. Siddons *et al.*, *A gigahertz-bandwidth atomic probe based on the slow-light Faraday effect*, Nat Photon **3**, 225–229 (04 2009).

[112] D. J. McCarron, S. A. King, and S. L. Cornish, *Modulation transfer spectroscopy in atomic Rubidium*, Meas. Sci. Technol **19**, 105601 (2008).

[113] P. Siddons, C. S. Adams, C. Ge, and I. G. Hughes, *Absolute absorption on Rubidium D lines: comparison between theory and experiment*, J. Phys. B **41**, 155004 (2008).

[114] B. E. Sherlock and I. G. Hughes, *How weak is a weak probe in laser spectroscopy?*, Am. J. Phys. **77**, 111–115 (2009).

[115] A. R. Edmonds, *Angular momentum in quantum mechanics*, 4th ed. (Princeton University Press, 1996).

[116] R. Loudon, *The Quantum Theory of Light*, 3rd ed. (Oxford Univeristy Press, 2000).

[117] C. Carr, *Private communication*.

[118] C. Cohen-Tannoudji, J. Dupont-Roc, and G. Grynberg, *Atom-photon interaction* (Wiley, 1992).

[119] J. H. Shirley, *Modulation transfer processes in optical heterodyne saturation spectroscopy*, Opt. Lett. **7**, 537 (1982).

[120] J. Zhang, D. Wei, C. Xie, and K. Peng, *Characteristics of absorption and dispersion for Rubidium D2 lines with the modulation transfer spectrum*, Opt. Express **11**, 1338–1344 (2003).

[121] R. P. Abel *et al.*, *Laser frequency stabilization to excited state transitions using electromagnetically induced transparency in a cascade system*, Appl. Phys. Lett. **94**, 071107 (2009).

[122] J. L. Hall, *Nobel lecture: Defining and measuring optical frequencies*, Rev. Mod. Phys. **78**, 1279–1295 (2006).

[123] B. Chéron *et al.*, *Laser frequency stabilization using Zeeman effect*, J. Phys. III France **4**, 401–406 (1994).

[124] K. L. Corwin *et al.*, *Frequency-stabilized diode laser with the Zeeman shift in an atomic vapor*, Appl. Opt. **37**, 3295–3298 (1998).

[125] A. Millett-Sikking, I. G Hughes, P. Tierney, and S. L. Cornish, *DAVLL lineshapes in atomic Rubidium*, J. Phys. B **40**, 187 (2007).

[126] M. L. Harris, S. L. Cornish, A. Tripathi, and I. G. Hughes, *Optimization of sub-Doppler DAVLL on the Rubidium D2 line*, J. Phys. B **41**, 085401 (2008).

[127] T. Petelski *et al.*, *Doppler-free spectroscopy using magnetically induced dichroism of atomic vapor: a new scheme for laser frequency locking*, Eur. Phys. J. D **22**, 279–283 (2003).

[128] G. Wasik, W. Gawlik, J. Zachorowski, and W. Zawadzki, *Laser frequency stabilization by Doppler-free magnetic dichroism*, Appl. Phys. B **75**, 613–619 (2002).

[129] C. P. Pearman *et al.*, *Polarization spectroscopy of a closed atomic transition: applications to laser frequency locking*, J. Phys. B **35**, 5141–5151 (2002).

[130] N. P. Robins *et al.*, *Interferometric, modulation-free laser stabilization*, Opt. Lett. **27**, 1905–1907 (Nov 2002).

[131] G. Jundt, G. T. Purves, C. S. Adams, and I. G. Hughes, *Non-linear Sagnac interferometry for pump-probe dispersion spectroscopy*, Eur. Phys. J. D **27**, 273–276 (2003).

[132] G. C. Bjorklund, *Frequency-modulation spectroscopy: a new method for measuring weak absorptions and dispersions*, Opt. Lett. **5**, 15–17 (1980).

[133] G. C. Bjorklund, M. D. Levenson, W. Lenth, and C. Ortiz, *Frequency modulation (FM) spectroscopy*, Appl. Phy. B **32**, 145–152 (1983).

[134] Th. Udem, R. Holzwarth, and T. W. Hänsch, *Optical frequency metrology*, Nature **416**, 233–237 (2002).

[135] P. Bohlouli-Zanjani, K. Afrousheh, and J. D. D. Martin, *Optical transfer cavity stabilization using current-modulated injection-locked diode lasers*, Rev. Sci. Instrum. **77**, 093105 (2006).

[136] D. M. Heywood S. C. Bell, J. D. White, J. D. Close, and R. E. Scholten, *Laser frequency offset locking using electromagnetically induced transparency*, Appl. Phys. Lett. **90**, 171120 (2007).

[137] D. V. Sheludko *et al.*, *State-selective imaging of cold atoms*, Phys. Rev. A **77**, 033401 (2008).

[138] J. D. Pritchard, *Cooperative Optical Non-linearity in a blockaded Rydberg ensemble*, Ph.D. thesis, Univeristy of Durham (2011).

[139] J. Gea-Banacloche, Y.-Q. Li, S.-Z. Jin, and M. Xiao, *Electromagnetically induced transparency in ladder-type inhomogeneously broadened media: Theory and experiment*, Phys. Rev. A **51**, 576–584 (1995).

[140] R. P. Abel, C. Carr, U. Krohn, and C. S. Adams, *Electrometry near a dielectric surface using Rydberg electromagnetically induced transparency*, Phys. Rev. A **84**, 023408 (2011).

[141] M. S. O'Sullivan and B. P. Stoicheff, *Scalar polarizabilities and avoided crossings of high Rydberg states in Rb*, Phys. Rev. A **31**, 2718 (1985).

[142] I. S. Grant and W. R. Phillips, *Electromagnetism* (Wiley, 1976).

[143] *Handbook of Chemistry and Physics*, 87th ed. (CRC Press, 2006).

[144] J. Jaeckel and A. Ringwald, *The low-energy frontier of particle physics*, arXiv:1002.0329v1(2010).

[145] E. R. Williams, J. E. Faller, and H. A. Hill, *New experimental test of Coulomb's law: A laboratory upper limit on the photon rest mass*, Phys. Rev. Lett. **26**, 721 (1971).

[146] J. Jaeckel and S. Roy, *Spectroscopy as a test of Coulomb's law*, arXiv:1008.3536v2(2010).

[147] M. Tanasittikosol *et al.*, *Microwave dressing of Rydberg dark states*, arXiv:1102.0226v3(2011).

[148] Alexej Schelle, Dominique Delande, and Andreas Buchleitner, *Microwave-driven atoms: From Anderson localization to Einstein's photoeffect*, Phys. Rev. Lett. **102**, 183001 (2009).

[149] G. H. Shortley and R. Weller, *The numerical solution of Laplace's equation*, J. Appl. Phys **9**, 334 (1938).